Search for extra dimensions in the diphoton channel with ATLAS experiment at LHC

Bao Tran Le

▶ **To cite this version:**

Bao Tran Le. Search for extra dimensions in the diphoton channel with ATLAS experiment at LHC. High Energy Physics - Experiment [hep-ex]. Université de Grenoble, 2013. English. NNT : . tel-00805474v1

HAL Id: tel-00805474

https://theses.hal.science/tel-00805474v1

Submitted on 28 Mar 2013 (v1), last revised 3 May 2013 (v2)

HAL is a multi-disciplinary open access archive for the deposit and dissemination of scientific research documents, whether they are published or not. The documents may come from teaching and research institutions in France or abroad, or from public or private research centers.

L'archive ouverte pluridisciplinaire **HAL**, est destinée au dépôt et à la diffusion de documents scientifiques de niveau recherche, publiés ou non, émanant des établissements d'enseignement et de recherche français ou étrangers, des laboratoires publics ou privés.

UNIVERSITÉ DE GRENOBLE

THÈSE

Pour obtenir le grade de

DOCTEUR DE L'UNIVERSITÉ DE GRENOBLE

Spécialité : **Physique Subatomique et Astroparticules**

Arrêté ministériel : 7 août 2006

Présentée par

LE Bao Tran

Thèse dirigée par **Jan STARK**

préparée au sein **Laboratoire de Physique Subatomique et de Cosmologie**
et de **l'Écoles Doctorale Physique de Grenoble**

Recherche de manifestations de dimensions supplémentaires dans le canal diphoton avec l'expérience ATLAS au LHC

Thèse soutenue publiquement le **19 Mars 2013**,
devant le jury composé de :

M. Patrick AURENCHE
LAPTh Annecy, Président
M. Erez ETZION
Tel Aviv University, Israel, Examinateur
M. Serguei GANJOUR
IRFU CEA-Saclay, Rapporteur
M. Bertrand LAFORGE
LPNHE-Paris VI University, Examinateur
M. Jan STARK
LPSC Grenoble, Directeur de thèse
M. Patrice VERDIER
IPNL Lyon, Rapporteur

ABSTRACT

This thesis summarizes a search for manifestations of Large Extra Dimensions (LED) using 4.91 fb^{-1} of data collected in 2011 by the Atlas detector at the LHC collider at CERN. In 2011, the LHC has provided proton-proton collisions at a center-of-mass energy of $\sqrt{s} = 7$ TeV. LED can potentially solve the so-called hierarchy problem, i.e. large apparent difference between two fundamental scales of the Standard Model (SM), the electroweak and the Planck scales. In the context of the ADD model (named after the authors N. Arkani-Hamed, S. Dimopoulos and G. Dvali) of LED, the effects of quantum gravity become much stronger than in the SM; possibly large enough to be observed at the LHC. There are two possibilities of graviton production in proton-proton collisions: direct graviton production and virtual graviton exchange. In this thesis, we present a search for the manifestation of extra dimensions via the effect of virtual graviton exchange on the di-photon final state. The di-photon invariant mass spectrum is studied and found to be in good agreement with SM background expectation. We set limits on the fundamental Planck scale of the ADD model using two different methods: a counting experiment and an analysis of the shape of the di-photon mass spectrum. The counting experiment yields limits between 2.62 and 3.92 TeV at 95% C.L., depending on the number of extra dimensions and the theoretical formalism used. The shape analysis yields slightly more stringent limits: the lower limits on the fundamental Planck scale improve by a factor of 1.04.

RÉSUMÉ

Cette thèse résume une recherche de manifestations de Grandes Dimensions Supplémentaires (GDS, Large Extra Dimensions en anglais) en utilisant 4.91 fb^{-1} de données enregistrées en 2011 par le détecteur Atlas installé auprès du collisionneur LHC au CERN. En 2011, le LHC a produit des collisions proton-proton à une énergie dans le centre de masse de $\sqrt{s} = 7$ TeV. Les GDS peuvent potentiellement expliquer une énigme connue sous le nom du problème de la hiérarchie : la grande différence entre l'échelle électrofaible et l'échelle de Planck dans le Modèle Standard (MS). Dans le cadre du modèle ADD (nommé selon les auteurs N. Arkani-Hamed, S. Dimopoulos and G. Dvali) des GDS, les effets de la gravitation quantique deviennent plus forts que dans le MS; potentiellement suffisamment forts pour être observés au LHC. Il y a deux mécanismes de production de gravitons dans les collisions proton-proton : production directe de gravitons et échange virtuel de gravitons. Dans cette thèse, nous présentons une recherche de dimensions supplémentaires via l'effet de l'échange virtuel de gravitons dans l'état final di-photon. Le spectre de masse invariante des événements di-photon est étudié, et un bon accord entre les données et le bruit de fond prédit par le MS est observé. Nous utilisons deux méthodes pour estimer des limites sur l'échelle de Planck fondamentale du modèle ADD : une expérience de comptage et une analyse de la forme du spectre de masse. L'expérience de comptage donne des limites entre 2.62 et 3.92 TeV à 95% C.L., en fonction du nombre de dimensions supplémentaires et du formalisme théorique utilisé. L'analyse de la forme du spectre de masse donne des limites légèrement plus strictes : la limite inférieure sur l'échelle de Planck fondamentale augmente d'un facteur de 1.04.

ACKNOWLEDGEMENTS

The first words, I would like to give many thanks to the jury members who spent time to travel and come for my thesis defense. I appreciate really much for their valuable comments in the manuscript completion, especially the “rapporteurs” who took time to write the thesis reports.

I am extremely grateful to my supervisor, Jan Stark, for his professional advices during the last three years. He has carefully and patiently guided me from the starting point of a newbie. Moreover, as a foreign student studying abroad, I encountered some difficulties in life and received many helps from him.

I would like to thank the Atlas group members at LPSC and the Atlas diphoton group for the scientific discussions. I would also like to thank the Director of LPSC who accepted me to work at the lab.

Besides, I acknowledge Rencontre du Vietnam organism and CNRS who have provided the financial supports for my study. I am grateful to people who are in France-Vietnam collaboration project and have companied me with their regards, such as Patrick Aurenche, Jean Tran Thanh Van, Sandrine Laplace, Do Hoang Son, etc.

And last but not least, I would express the deepest love to my parents who gave birth to me and support all my endeavors. It is also a pleasure for me to thank my sisters and good friends for their encouragement during the time when I needed.

Contents

Chapter 1

Theoretical background

Thousands of years ago our universe has been thought of as made of a small structure, called atom. At the beginning of the 20th century, it has been shown experimentally that the atom is not the smallest constituent of nature. It is made of subatomic particles, such as protons, neutrons and electrons. So, are these the elementary particles of the universe? The answer is "no" and it has been proven experimentally that proton and neutron are constituted of quarks. This discovery opened a golden era of particle physics development. Through the 20th century, new particles were discovered and interactions between them have been well understood. A theory now known as "Standard Model" (SM) was proposed to describe fundamental particles and their interactions by a relativistic quantum field theory. It has been tested over the past four decades in a variety of experiments and is verified to be the most successful theory framework in particle physics. However, it is most likely not a complete model, since there are still unanswered questions in the theoretical construction. The so-called hierarchy problem is an example of the hints which suggest that the SM may be incomplete. It refers to the tremendous difference of two fundamental scales: the Planck scale and the electroweak scale. In this thesis, we consider a Large Extra Dimension theoretical model which has been proposed to solve this problem.

We all perceive the world around us as three dimensional space. But, is this a complete picture? It is possible that there are, in addition to the ordinary dimensions which we have already known, extra spatial dimensions. We do not feel these additional dimensions because they are different from the three dimensions we are

familiar with. Our observation is constrained to a three dimensional space which is located in a higher dimensional volume. If the extra dimensions really exist, they are thought to be "curled-up", or compactified with very small radius. The idea of additional spatial dimensions appears naturally in string theory when ones tries to construct a consistent description of quantum gravity. Thus we could detect the existence of any extra dimensions through their effect on gravity. The gravitational force would be modified at distance comparable to the size of extra dimensions. Based on this concept, the Large Extra Dimension model was built and its observable effects are potentially detectable in high energy experiments, such as Large Hadron Collider (LHC) which is so far the most powerful accelerator built to study for high energy physics. More information of the LHC will be discussed in chapter 2.

This chapter will begin with a short introduction to the SM and its history. Then we will describe the hierarchy problem and one of the solutions for it, the Large Extra Dimension paradigm. Two mechanisms of graviton production in the context of this model, namely the processes of direct graviton emission and virtual graviton exchange, are discussed. In addition, we review results from different experimental searches for Large Extra Dimensions. Finally, as we will search graviton decays to photon pairs, we discuss the production of photon pairs in the framework of the SM theory. This gives us a general idea of background contamination in our analysis.

1.1 Standard Model

In the Standard Model, matter is made up of quarks and leptons. They are fermions of half-integer spin. There are six types of quarks grouped into three generations: up and down, charm and strange, top and bottom. The up-type quarks have charge of 2/3 while the down-type quarks have charge of -1/3. The mass of quarks increases in order: the first generation has the smallest masses, the third generation has the highest masses. There are also six leptons which form another family of elementary fermions. They are classified into three generations similarly to quarks. Each generation is comprised of a unit electrical charged lepton coupled with a zero-charged lepton. The three charged leptons are electron (e^-), muon (μ^-) and tau (τ^-). Each of them has their associated neutral lepton, called neutrino (ν_e, ν_μ, ν_τ). Figure 1.1 summarizes

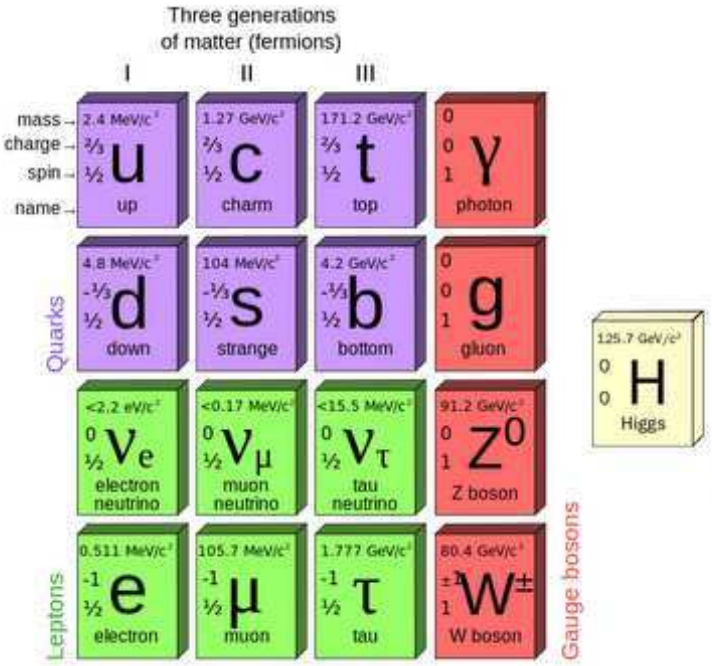

Figure 1.1: Elementary particles in Standard Model.

all particles and their properties described in SM [1]. Note that for each quark and lepton, there is partner anti-particle which has the same mass, but opposite charges.

There are four known types of interactions: strong, weak, electromagnetic and gravitational interactions. The interaction between particles is mediated by transmitting a force carrier, called gauge boson. The strong force is responsible for holding the quarks together to form larger particles. The carriers of the strong force are the gluons. The weak force can be observed in the decay processes of heavy quarks and leptons. The first evidence of this interaction came from the study of beta decay in nuclear physics [1]. The W and Z bosons are the carriers of the weak interaction. The electromagnetic force mediates the interactions between charged particles. The photon is the carrier of the electromagnetic force. It is a massless and neutral bo-

[1]This process is explained at the partonic level as the transition of a neutron (or d quark) to a proton (or u quark) or inversely. In 1934, Fermi developed a theory to interpret the beta decay [2] with an unknown explanation in terms of weak interaction. The nature of weak interaction for this process has been studied in detail later on.

son. Only three interactions are included in SM, the gravity is not described since the gravitational attraction for microscopic particles is very small compared to the other interactions ($\sim 10^{29}$ weaker than the weak force [3]). Although no complete quantum treatment of gravity exists to date, massless spin-2 graviton is thought to be the gauge boson that transmits the gravitational force. Its tiny strength raises a question about the naturalness of the theoretical construction. This is referred to as hierarchy problem of the SM which will be discussed later.

Each of the four interactions has been described in its own physical theory. The classical theory of gravity is Newton's law of universal gravitation. Einstein generalized its relativistic treatment in a general theory of relativity. We have not successfully constructed a renormalizable quantum gravity yet and its effects have never been observed experimentally since the gravity is simply too small to play a significant role in elementary particle physics. The physical theory which describes the electromagnetic force is called electrodynamics and described by the well-known Maxwell equations established over one hundred years ago. The quantum theory of electrodynamics was perfected by Tomonaga, Feynman and Schwinger in the 1940s. The weak force was unknown to classical physics, its description was at the beginning given in a relativistic quantum formulation. There were several theories modeled for the weak force, until the 1960s when Glashow, Weinberg and Salam (GWS) presented a beautiful theory that unified the weak and electromagnetic forces into a single electroweak one [4, 5, 6, 7]. Therefore the model of GWS is often called electroweak theory. For the strong interaction, a first attempt of explanation was given by Yukawa in the 1930s [8]. A more complete theory called chromodynamics was proposed in the 1970s [9].

In the SM, quarks are the only particles which undergo the strong forces, leptons do not. Besides the electrical charge, quarks have an additional degree of freedom called the color charge which is red (r), blue (b) or green (g). It is conventionally referred to as charge of the strong interaction. The color-charged quarks are not observed individually, they are always found as bound states of hadrons which are combinations of quarks and which are colorless charge. This addresses confinement of quarks in hadrons and is explained by a phenomenon known as asymptotic freedom at small distance or high energy [10, 11, 12] in QCD. The strong coupling strength is

weak when the distance between quarks is small (compared to the radius of proton) and it becomes stronger when quarks move far away each other. The observation of quarks in nature is always indirect through the composite forms of hadrons. Two types of hadron are: baryon and meson. A combination of three quarks (anti-quarks) creates a baryon (anti-baryon), while a quark and an anti-quark combination forms a meson. Additionally, unlike the photon in electromagnetic interaction, the gluons can interact with each other as they themselves possess color charge.

There is no dedicated name for the "charge" that produces weak forces, in the sense that electric charge produces electromagnetic forces and color charge produces strong forces. Whatever it is, all quarks and all leptons carry it. This means the weak interaction acts on all particles. There are two kinds of weak interactions. The first one is neutral weak interaction mediated by the Z boson. A quark or lepton does not change flavor after absorbing or emitting a Z boson. For most Feynman diagrams that describe an interaction via photon exchange, there is corresponding diagram in which the photon is replaced by a Z boson. The second type of weak interaction is flavor changing, mediated by the massive W boson. A particle converts into its partner after interacting with the W, for example an electron turns into its corresponding neutrino ν_e with the emission of a W, or an up quark changes to a down quark and reversely. The charge-current weak interaction gives transitions whether within a generation or possibly generational mixing. For example, instead of d, u is coupled with d' which is a linear combination of the three d, s, b. This is contained in the Cabibbo-Kobayashi-Maskawa matrix [13, 14] which describes the cross-generational transitions of quarks in weak interaction.

The Standard Model is a non-abelian gauge theory which beautifully describes the three forces of nature, except the gravitational force. The theory is based on the gauge symmetry group $SU(3) \times SU(2) \times U(1)$. The strong force arises from $SU(3)$ while $SU(2) \times U(1)$ represents the electroweak force. $SU(2)$ after denoted $SU(2)_L$ is the weak isospin group and acts only on the left-handed fermions, while $U(1)$ after denoted $U(1)_Y$ is the hypercharge Y group. In order to be renormalizable, the Lagrangian of the theory is required to be invariant under local gauge transformations. By demanding this requirement, it is mandatory to introduce new vector fields in the Lagrangian and their associated gauge bosons. For $SU(3)$ transformation, vector

fields are represented by eight gluons in particle language. The gauge fields for $SU(2)$ are $W^i_\mu, i = 1, 2, 3$. The gauge field corresponding to the $U(1)$ transformation is B_μ. In electroweak model, these fields do not present themselves but mix together to form the charged states $W^\pm_\mu$ which are identified as the physical $W^\pm$ bosons respectively.

$$W^\pm = \frac{W^1_\mu \mp iW^2_\mu}{\sqrt{2}} \tag{1.1}$$

The electroweak gauge symmetry $SU(2) \times U(1)$ is spontaneously broken to the $U(1)$ gauge symmetry of electromagnetism. In this symmetry breaking mechanism, the neutral charge states W^3_μ of $SU(2)$ and B_μ of the original $U(1)$ get mixed to produce the photon and the Z boson:

$$A_\mu = \frac{g_2 B_\mu - g_1 Y_L W^3_\mu}{\sqrt{g_2^2 + g_1^2 Y_L^2}} \tag{1.2}$$

$$Z_\mu = \frac{g_1 Y_L B_\mu + g_2 W^3_\mu}{\sqrt{g_2^2 + g_1^2 Y_L^2}} \tag{1.3}$$

where Y_L is the left-handed projection of the hypercharge Y, for which $Y_L = -1$. The hypercharge Y relates to electric charge Q and the third component of the weak isospin T_3 by the equation $Y = 2(Q - T_3)$. The symbols g_1 and g_2 denote the coupling constants of the $U(1)_Y$ and $SU(2)$ fields. The A_μ and Z_μ correspond to the photon and Z boson, respectively.

In conclusion, in the context of local gauge invariance, in addition to the requirement of introducing new vector fields, the associated bosons corresponding to these fields need to be massless. This can describe the appearance of gluons and photon with zero mass. However, the W and Z bosons are experimentally massive. In order to generate the mass term into the Lagrangian and make it still locally gauge invariant, one needs to exploit a procedure of spontaneous symmetry breaking and Higgs mechanism [15, 16]. By introducing a new scalar field of which the quantum treatment is Higgs boson, the weak interaction gauge bosons acquire mass through interaction with it. Recently, new results [17, 18] from two of the largest experiments at LHC, ATLAS and CMS, gave strong evidence for the existence of the Higgs boson that make SM a more complete theory beautifully describing the universe we live in.

1.2 Hierarchy problem

Although SM describes well the behavior of the microscopic particle world, there are still some aspects that have not been explained satisfactorily. The gravitational force is not included in SM because it has tiny strength at elementary particle level comparing to the weak interaction. Thus its coupling strength is much smaller than couplings of the other forces. This leads to the so-called hierarchy problem in SM. Alternatively, it is possible to express the difference in the sense of two fundamental energy scales in nature. This corresponds to a tremendous hierarchy from the scale of electroweak symmetry breaking $m_{EW} \sim 100$ GeV to the Planck scale $M_{Pl} = 1/\sqrt{G_N} \sim 10^{16}$ TeV at which the gravity is expected to become as strong as the other known forces. Here G_N denotes the Newton's coupling constant.

Why such a large difference? Which mechanism makes the gravity so much weaker than the other interactions in the particle world? Theoretical physicists have developed several theories trying to solve this problem. Some have argued that new particles and new forces are needed, and many theories arise such as supersymmetry, technicolor , little Higgs, etc. Some have argued that our understanding of gravity is mistaken and that there are new dimensions ("extra dimensions") of space that have not been detected and will become apparent to our experiments at larger energy, possibly at the LHC in the near future. Or Nature may have chosen a completely different scenario to give rise to this hierarchy.

1.3 Large Extra Dimensions

Many theories have been proposed to solve the hierarchy problem in the SM. In this thesis, we discuss a particular framework which addresses the problem via the postulate of extra spatial dimensions. One of the solutions using this idea is known as Large Extra Dimension model proposed by Nima Arkani-Hamed, Savas Dimopoulos and Georgi Dvali (ADD) [19, 20, 21].

The idea of extra dimensions was initiated by Kaluza-Klein theory in 1920s [22]. Kaluza [23] firstly attempted to unify the gravity and electromagnetism by extending the general relativity to a five-dimensional spacetime and Klein [24] then proposed this extra dimension to be curled up in a cirle of very small radius to explain its unobserved

nature. Around 1980s, string theory employed it as a requirement for describing a consistent theory of quantum gravity [25]. However, the extra dimensions in string theory is supposed to be compactified at a scale close to the Planck scale, and are very difficult to test in the up-to-date experiments. A different approach was given in ADD model which proposes the size of the extra dimensions could be roughly at millimeter and at the TeV scale that leads to possible observation at the LHC or near future experiments.

In the ADD framework, in addition to the ordinary flat 3D dimension (a so-called "brane") which we are familiar with, it is proposed that there are additional spatial dimensions which are thought to be curled-up, or compactified. The entire space is usually called the "bulk". If we assume that the electroweak scale m_{EW} is the only fundamental scale in nature, the scale for the strength of gravitational interaction is approximately set to m_{EW}. In this philosophy, the tremendous discrepancy between the weak and Planck scale disappears, the hierarchy problem is trivially resolved. The ordinary Planck scale M_{Pl} which we have seen before is just an apparent manifestation on the brane of the actual constant M_D in the (4+n) dimensional theory (the "4" is referred to 3D space+time dimensions).

Let's suppose that there are n extra compactified spatial dimensions with radius $\sim R$ in our universe. The gravitational potential energy of two masses m_1, m_2 placed within a distance $r \ll R$ dictated by Gauss's law in (4+n) dimensions is:

$$V(r) \sim \frac{m_1 m_2}{M_D^{n+2}} \frac{1}{r^{n+1}} \quad , \quad (r \ll R) \tag{1.4}$$

On the other hand, if the masses are placed at distance $r \gg R$, their gravitational flux lines can not continue to penetrate in the extra dimensions, and the usual $1/r$ potential is obtained,

$$V(r) \sim \frac{m_1 m_2}{M_D^{n+2} R^n} \frac{1}{r} \quad , \quad (r \gg R) \tag{1.5}$$

so our effective 4 dimensional M_{Pl} is

$$M_{Pl}^2 \sim M_D^{n+2} R^n \tag{1.6}$$

Putting $M_D \sim m_{EW}$ and demanding that R be chosen to reproduce the observed M_{Pl}, the size of extra dimensions R is estimated by [19]

$$R \sim 10^{\frac{30}{n}-17}\text{cm} \times \left(\frac{1\text{TeV}}{m_{EW}}\right)^{1+\frac{2}{n}} \tag{1.7}$$

For $n = 1$, $R \sim 10^{13}$ cm, its size is of the order of the radius of solar system. However, its size reduces to only ~ 1 mm for the case of two ED. It is similar to the size of an atom ~ 1 nm for three ED. It further decreases to subatomic sizes and reaches ~ 1 fm (the size of a proton) for seven ED. We have seen that Newton's law at distances comparable to the size of ED is modified as a consequence of the compacted extra dimensions. The gravitational potential would fall as $1/r^{n+1}$ for $r \lesssim R$. This explicitly excludes the case of a single ED, as it have been proved that our solar system requires the potential to fall as $1/r$ at the distance comparable to the size of planetary orbits. For cases of $n \geqslant 2$, they are all possible because Newton's law has not been tested at distances smaller than 1 mm [26]. This reveals that in this model a large ED with the size as macroscopic as 1 mm is perfectly possible.

While submillimeter dimensions remain untested for gravity, the particle physics forces have certainly been accurately measured up to weak scale distances (about 10^{-18} cm). In the ADD paradigm, in order to not violate any constraints from subatomic physics and from experimental data, the SM particles and gauge interactions are constrained to be localized in the ordinary 4 space-time dimensional submanifold. However, gravitons can penetrate freely through these extra dimensions. The extra spatial dimensions create an extra volume which is sufficiently large to dilute the gravity, so that it appears weak to an observer in the brane. This is a possible interpretation of the very small strength of gravitational interaction compared to the others.

When a graviton enters the compactified extra dimensions, the periodic boundary condition, as caused by compactification, leads to a quantization of the graviton's energy into discrete eigenvalues. From the point of view of a 3-dimensional observer, the eigenmodes are seen as a tower of graviton excitations which are referred to as Kaluza-Klein (KK) modes. The energy spacing between the KK excitations of the graviton depends on the size of ED ($\sim 1/R$), and it increases from ~ 0.1 meV to 100 MeV if the size of ED changes from $\sim 10^{-3}$ to 10^{-15} mm. Although each KK mode couples to the energy-momentum tensor with the gravitational strength $1/M_{Pl}^2$, the integration over a large number of KK modes tremendously enhances the strength of the gravitational interaction. For example, with the collision energy of ~ 1 TeV, given the size of ED ~ 1 fm, about 10^4 KK modes along each extra dimension can

be reached. Knowing that one expects $n = 7$ extra dimensions corresponding to this size, $10^{4n} = 10^{28}$ modes in total are excited, thus the gravitational interaction is amplified by this huge factor [27]. In addition, as the energy spacing between modes is very small, it is difficult to resolve the adjacent modes. In most of the experiments, the KK spectrum would appear to be continuous. This spectrum breaks down at a certain ultraviolet cutoff M_S which represents the validity cut-off scale of the Einstein gravitational action. As an analogy, it is the scale in which the complete SM theory is known and reliable. A new mass scale has been introduced in the model besides the fundamental parameters M_D and number of ED n. This energy cutoff is expected to be of order of M_D [28], since the ratio M_S/M_D parametrizes how strongly (or weakly) coupled quantum gravity is.

In summary, it is perfectly possible that quantum-gravity effects start to reveal themselves at energies much lower than M_{Pl} , possibly as low as the weak scale in the context of ADD model. This has the exciting implication that high energy collider experiments such as LHC may be able to probe the physics of quantum gravity.

1.4 Probing Extra Dimensions through graviton effects

It is not surprising that gravitons are an important subject of study when investigating the manifestation of extra spatial dimensions in ADD model. Two possible effects of gravitons will be discussed specifically. The first is known as direct graviton effect, while the second is virtual graviton effect.

1.4.1 Direct graviton emission

Because Kaluza-Klein gravitons couple to the energy momentum tensor, they can be added to any vertex or line in a SM Feynman diagram [29]. For example, a KK graviton can be directly created in the following processes $q + \overline{q} \rightarrow g + G_{KK}$, $q + g \rightarrow q + G_{KK}$, or $g + g \rightarrow g + G_{KK}$ which result in a monojet in final state. The graviton would escape from our 3 dimensional world to the extra dimensions, carrying away a part of the energy of the collision. The experimental signature of

these processes is apparently a monojet with a large transverse momentum non-conservation.

Real graviton emission yields stable cross section prediction which directly depends on the fundamental Planck scale M_D [29]. This is an interesting signature to probe for extra spatial dimension, but not in the scope of this thesis. The study has been performed in [30]. We concentrate on the other type of effects called virtual graviton exchange which will be discussed in the following section.

1.4.2 Virtual graviton effect

1.4.2.1 Experimental signature

Apart from collisions where gravitons are directly emitted, it is also possible for a so-called virtual graviton to be created. Virtual, in a sense, means that the graviton does not show itself in the final state of a process, it is just an intermediate off-shell particle which exists between the initial and final states of purely SM particles. In a Feynman diagram that describes the process, the virtual graviton is presented by a line connecting two interaction vertices. Intuitively, a graviton after being created consequently decays into a pair of photons or leptons as a Drell-Yan like process. The latter is less sensitive because decays of spin-2 gravitons to spin-1/2 leptons are suppressed. The virtual graviton effect typically contributes to the Drell-Yan (DY) or diphoton spectrum at high invariant mass. Thus, it can be observed as deviations in the cross section and mass spectra from the SM prediction. The virtual graviton exchange diagram can interfere constructively or destructively with its SM counterpart. The Drell-Yan processes in the presence of large extra dimensions is shown in figure 1.2. Note that this is just one of the many processes where virtual graviton effects can take place. Our channel of interest is diphoton production which has similar diagrams but replace two leptons by two photons in the final state.

1.4.2.2 Predicted cross section

The cross section of virtual graviton exchange is not well-defined since it depends on a particular representation of the interaction Lagrangian and the definition of the ultraviolet cutoff for the KK modes. There are three such popular representations [29,

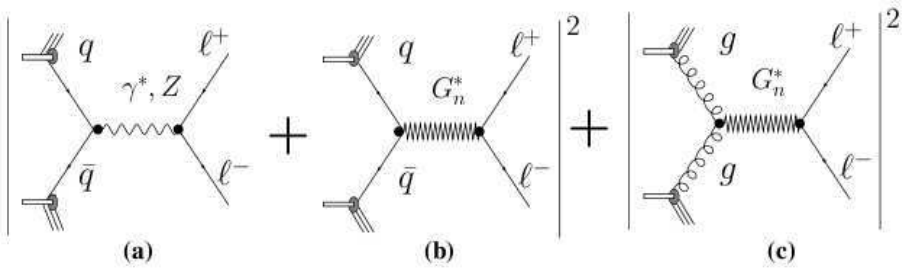

Figure 1.2: Feynman diagrams for the modified Drell-Yan production in the presence of large extra dimension,(a) the Standard Model and (b),(c) the exchange of a Kaluza-Klein graviton contributions [31].

32, 33]. The effects of ED are parametrized via a single variable $\eta_G = \mathcal{F}/M_S^4$, where $\mathcal{F}$ is a dimensionless parameter reflecting the dependence of virtual G_{KK} exchange on the number of extra dimensions. Definition of $\mathcal{F}$ in each representation mentioned above are as follows:

$$\mathcal{F} = 1, \text{ (GRW) [29]}; \tag{1.8}$$

$$\mathcal{F} = \begin{cases} \log\left(\frac{M_S^2}{\hat{s}}\right) & n = 2 \\ \frac{2}{n-2} & n > 2 \end{cases}, \text{ (HLZ) [33]}; \tag{1.9}$$

$$\mathcal{F} = \frac{2\lambda}{\pi} = \pm\frac{2}{\pi}, \text{ (Hewett) [32]}. \tag{1.10}$$

In the above formula, $\mathcal{F}$ depends explicitly on the number of ED only in the HLZ formalism. The gravitational effect contributes constructively in both the HLZ and GRW formalism. However, in the Hewett convention, the sign of F is unknown and included in a parameter λ. The value of λ is of order 1 and usually assigned either +1 (constructive interference) or -1 (destructive interference). The parameter η_G has units of TeV^{-4} if M_S is expressed in TeV, and describes the strength of gravity in the presence of large ED.

The differential or total cross section of diphoton (or dilepton) production in the presence of virtual graviton exchange can be parametrized as [27]:

$$\sigma_{tot} = \sigma_{SM} + \eta_G \sigma_{int} + \eta_G^2 \sigma_G, \tag{1.11}$$

where σ_{SM} is the SM cross section for the processes under study and σ_{int} and σ_G are the interference and pure graviton effects, respectively. Note that the G_{KK} exchange

effect is expressed by the parameter η_G as in equation 1.11, the direct term and interference term in the excess cross section are proportional to $1/M_S^8$ and $1/M_S^4$, respectively.

Virtual graviton effect is complementary to direct graviton emission in the quest of validating ADD model, or generally searching for extra spacial dimensions. The former process depends on the ultraviolet cutoff of KK spectrum M_S, while the latter depends directly on the fundamental Planck scale M_D. Even if both scales are expected to be of the same order, it is quite possible that M_S is somewhat lower than M_D, thus the effect of extra dimension might be detected in virtual graviton exchange before they are observed in direct emission.

1.5 Experimental Constraints and Limits

Searches for large extra dimensions have been performed in many experiments. So far no evidence of graviton production has been observed. However, the analyses at the Large Electron Positron (LEP), Tevatron and LHC colliders have placed limits on the size of extra dimensions and the Planck scale of extra dimensional space. The limits directly set on the fundamental Planck scale in large extra dimensions with respect to the number of extra dimensions are summarized in ref. [34] for several collider experiments.

In particular, the analysis from virtual graviton exchange signature permits to constrain the ultraviolet cutoff scale of the model. The DØ experiment set 95% C.L. limits on M_S between 2.1 TeV and 1.3 TeV for 2 to 7 extra dimensions [35]. More recently, in a study of the diphoton channel with 2011 data samples of $\sim$ 2.2 fb^{-1}, CMS set a lower limit of 2.3 - 3.8 TeV on the scale M_S with 95% C.L. [36]. While ATLAS, in the same analysis using full sets of 2011 data ~ 4.9 fb^{-1}, set 95% C.L. limits on M_S between 2.6 TeV and 3.9 TeV depending on the number of extra dimensions and the theoretical formalism used [37]. The Atlas results in Ref. [37] are also the results which will be presented in this thesis.

1.6 Diphoton production in SM

In addition to our signal channel of diphoton from virtual graviton exchange, there are various SM processes which abundantly produce two photons in the final state. These processes contribute a considerable background component and require to be quantitatively evaluated.

In high energy collisions, photons are mostly produced via quark-gluon Compton scattering or quark-antiquark annihilation where photons take part directly in the hard scattering process. They are called direct photons which are distinguished from those resulting from decays of π^0 at large transverse momentum. In addition to these processes, photon production can also be due to the fragmentation of outgoing partons (often known as bremsstrahlung). Along these lines, we can classify the diphoton production into three categories: two direct photons, one direct photon plus one resulting from fragmentation of a quark or gluon (single fragmentation), and both photons from fragmentation (double fragmentation).

The straightforward LO diagram of diphoton production in perturbative calculation is known as quark-antiquark annihilation (Born process). The coupling of this process is of order $\mathcal{O}(\alpha^2)$, as illustrated in "diagram a" of figure 1.3. A NLO correction in terms of QCD pertubative calculation of order $\mathcal{O}(\alpha^2\alpha_S)$ is also included, such as processes with virtual correction to $q + \overline{q} \to \gamma\gamma$ and gq (or $\overline{q}$) $\to \gamma\gamma q$ (or $\overline{q}$) shown in "diagrams b and c" of figure 1.3 respectively. At a higher order, for example in the process $gq \to \gamma\gamma q$, final state quark-photon collinear singularities appear in the calculation. From a physical point of view, this phenomenon is observed as a photon accompanied by hadrons going in the same direction. The singularities are factorized and absorbed into the fragmentation functions at some arbitrary fragmentation scale M_f. This yields a second type of leading order contribution: the single fragmentation, see "diagram d" of figure 1.4 for example. When the fragmentation scale M_f is chosen of the order of hard scattering scale $\gg 1$ GeV, the gluon and quark fragmentation functions behave roughly as $\alpha/\alpha_S(M_f^2)$ [38], and it gives a cancellation of the α_S term in the QCD perturbative calculation in "diagram d". As a consequence, the contribution of single fragmentation process is asymptotically of the same order as the Born process. A consistent treatment at NLO corrections $\mathcal{O}(\alpha^2\alpha_S)$ to this contribution is expressed in "diagrams e and f" of figure 1.4. Similarly, the absorption of collinear

singularity appearance in "diagram f" yields the last leading order contribution of diphoton production: the double fragmentation type, see "diagram g" of figure 1.5. Examples of NLO corrections to this contribution are seen in "diagrams h and i" of figure 1.5.

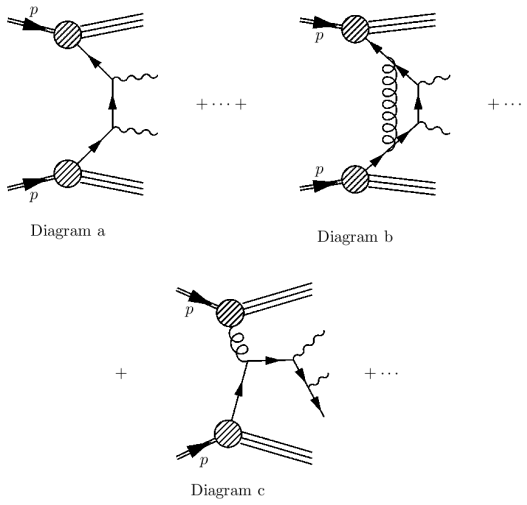

Figure 1.3: Direct production diagrams: (a) Born process, (b) virtual gluon correction to diagram a, (c) radiative photon from quark/gluon interaction [38].

Beyond these, the gluon fusion (so-called box process) $gg \rightarrow \gamma\gamma$ through a quark loop is also taken into account, as shown in figure 1.6. Strictly speaking, it is a NNLO contribution from the point of view of power counting. It is nevertheless taken into account for the reason of very high gluon luminosity compared to the quark and antiquark ones. This nearly compensates the extra powers of α_s, so as to yield a comparable contribution to the Born term. Therefore, it is also counted in the two direct photons contribution.

Note that the fragmentation processes dominate significantly in the intermediate mass region. In the interesting high mass region where LED effect might show up, the main contribution is only the "two direct" component (including gluon fusion) while the others can be neglected.

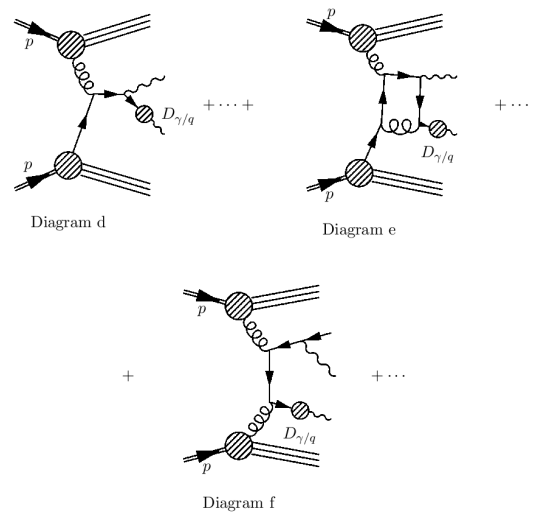

Figure 1.4: Single fragmentation diagrams [38].

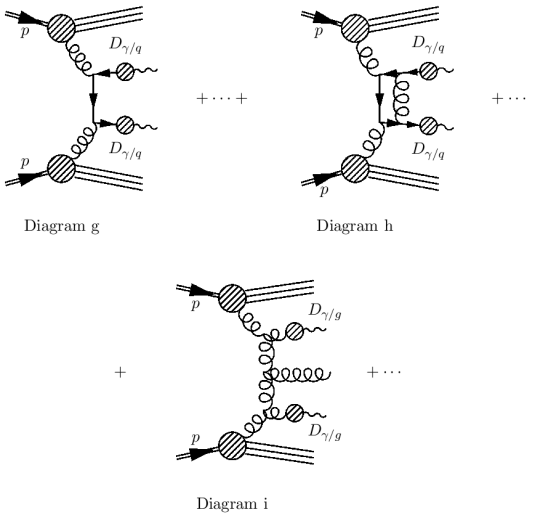

Figure 1.5: Double fragmentation diagrams [38].

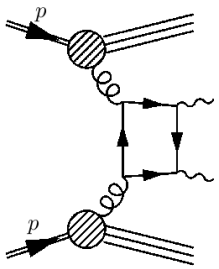

Figure 1.6: Gluon fusion diagram [38].

Chapter 2

ATLAS detector at LHC

We will present in this chapter an overview of the experimental setup. The first section is a short introduction to the Large Hadron Collider (LHC). The Atlas detector and its components are discussed in the following sections. We also briefly present the trigger and data acquisition system of Atlas, and the introduction of data and Monte Carlo simulations for analysis in the last sections of this chapter.

2.1 LHC overview

The LHC [39] at CERN (Geneva, Switzerland) is currently the world's highest-energy particle collider. It is installed in a tunnel approximately 100 m underground with a circumference of 27 km that used to be occupied by the Large Electron Positron (LEP) collider [40]. It is designed to accelerate two oppositely oriented proton beams to the energy of 7 TeV, in order to provide collisions up to the center-of-mass energy of $\sqrt{s} = 14$ TeV with a luminosity of $10^{34}\ cm^{-2}s^{-1}$.

Protons are dissociated from hydrogen atoms and injected to a chain of accelerators. In a first step, protons are accelerated to 50 MeV by the Linear Accelerator (LINAC). They are then directed to the Proton Synchrotron Booster (PSB) which accelerates them to 1.4 GeV and consecutively to Proton Synchrotron (PS) where the energy is increased to 25 GeV. After injection to the Super Proton Synchrotron (SPS) providing 450 GeV of energy, protons are transferred into the main LHC ring where they circulate in both directions: clockwise and anti-clockwise. The scheme of the

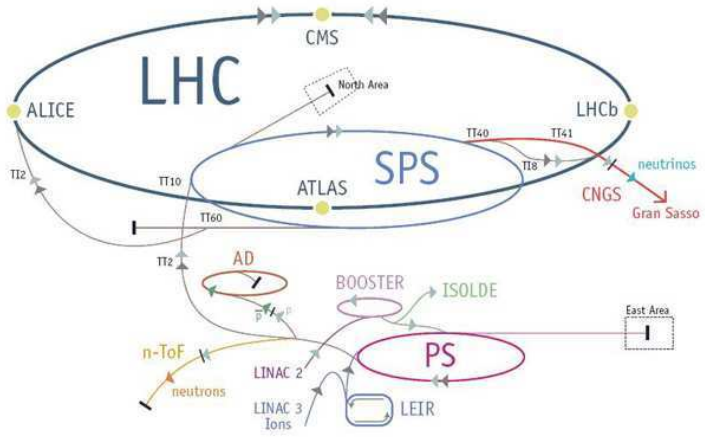

Figure 2.1: Overview of LHC.

acceleration chain is illustrated in figure 2.1. The two beams are circulated in separate vacuum ring tunnels with magnetic fields of opposite orientation and ramped up to the design energy in a few minutes. The beams are kept at stable energy during collision runs. Dipole magnets keep the particles on a bent curve and quadrupole magnets keep the beam focused. The magnetic field is created by superconducting material immersed in 1.9 K liquid helium.

There are 4 main interaction points where two beams are adjusted to collide head-on. Consequently, there are 4 principal detectors installed at each of the interaction regions: ATLAS (A Toroidal LHC ApparatuS) and CMS (Compact Muon Solenoid) are general purpose detectors designed to discover new physics at LHC, while the other two are more specialized, ALICE (A Large Ion Collider Experiment) is dedicated to the study of heavy ion collisions and LHCb is devoted to CP-violation and B-physics studies in order to better understand the matter-antimatter asymmetry of the universe. LHC operation is hopefully the key to open the secrets of the universe which have not been discovered during last decades, thanks to its large increase in energy and luminosity compared to previous colliders.

Protons are circulating in the rings not continuously but in portions called "bunches". There are 3564 bunches for a proton beam at full intensity and the density of protons per bunch is about 10^{11} protons/16 μm and the bunch spacing is of 25 ns. These numbers do not reflect the current state of LHC but the nominal design.

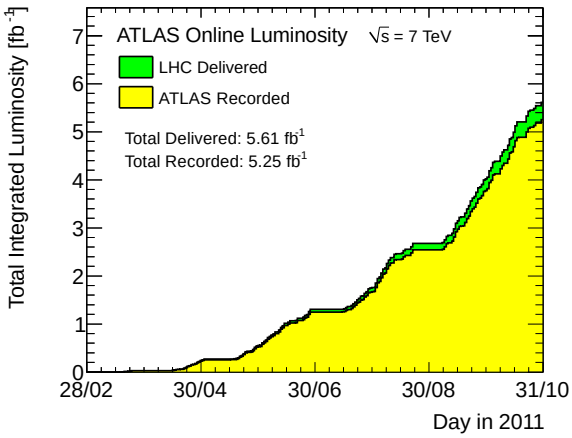

Figure 2.2: The total cumulative integrated luminosity in the 2011 dataset.

The probability of a process to occur is measured by the corresponding interaction cross section. The event rate depends not only on the interaction cross section, but also on the luminosity of the collider which is proportional to the beam intensities, the number of bunches per beam, the beam collision frequency and inversely the beam size at the interacting point. Therefore, it is necessary to have a luminosity large enough to produce new interesting processes which usually have very small cross sections. At the design luminosity of LHC 10^{34} $cm^{-1}s^{-1}$ and the maximum collider energy of 14 TeV, about 600 million inelastic events per second, or about 20 events per crossing, are produced at a given interaction region.

The LHC was successfully in operation with its half designed energy $\sqrt{s} = 7$ TeV in March of 2010. The accelerator ran at this energy during two periods in 2010 and 2011. A higher energy run at $\sqrt{s} = 8$ TeV was achieved during 2012 and the design goal of $\sqrt{s} = 14$ TeV is planned in 2015. In this thesis, we provide more information of data collected in 2011 since the analysis concentrates on this collection period. In 2011, the LHC was operated with different bunch spacings, gradually increasing (75, 50 and 25 ns) and the maximum number of bunches achieved is of 1380 per beam [41]. Figure 2.2 illustrates the integrated luminosity which reached 4.91 fb^{-1} by the end of 2011. The peak luminosity increased regularly and a peak up to $3.5 \times 10^{33} cm^{-2}s^{-1}$ was achieved [42].

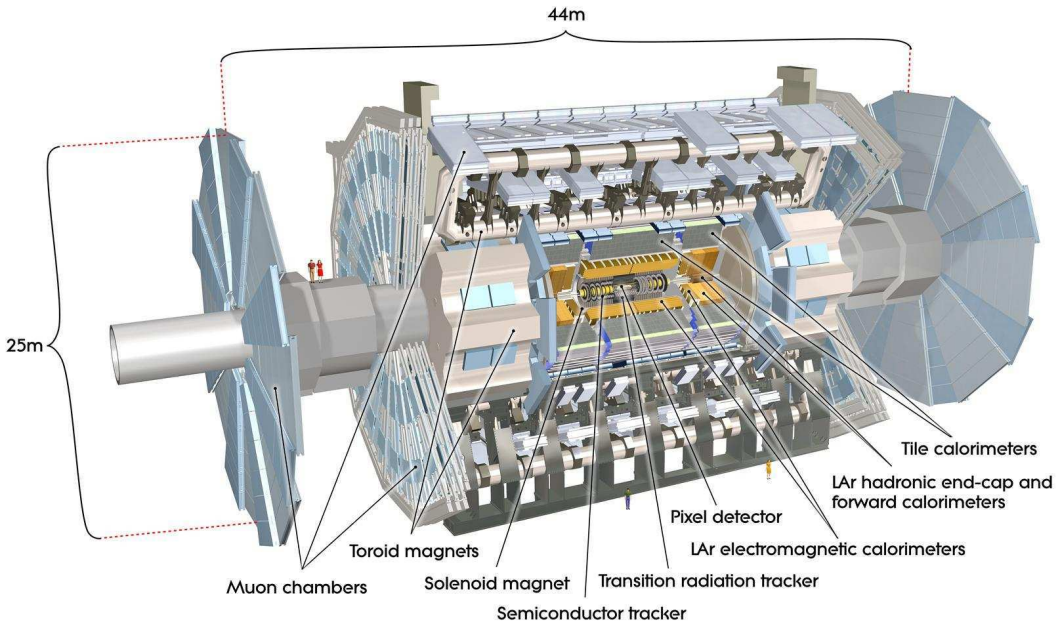

Figure 2.3: Cut-away view of the ATLAS detector.

2.2 The Atlas detector

ATLAS is a general purpose detector, constructed to study particle physics in the TeV energy range. With dimensions of 25 m in diameter, 44 m in length and a weight of roughly 7000 tonnes [43], it is the largest detector at the LHC. The different detector systems of ATLAS are structured concentrically around the beam line, as shown in Figure 2.3. The innermost detector component is the Inner Detector (ID), followed by the electromagnetic and hadronic calorimeters and the muon spectrometer. Table 2.1 summarizes the general requirement of resolution for each delector component. The following sections will review the coordinate system used to describe the ATLAS detector, as well as the individual detector components and the ATLAS trigger system.

The LHC beams collide in the center of the ATLAS detector, which defines the origin of right-handed Cartesian system. The z-axis is parallel to the beam line and the x-y plane is perpendicular to the beam line. The positive x-axis is defined as pointing from the interaction point to the center of the LHC ring, and the positive

Detetor components	Required resolution
Tracking	$\sigma_{p_T}/p_T = 0.05\% p_T \bigoplus 1\%$
EM Calorimeter	$\sigma_E/E = 10\%/\sqrt{E} \bigoplus 0.7\%$
Hadronic calorimeter	
barrel and endcap	$\sigma_E/E = 50\%/\sqrt{E} \bigoplus 3\%$
forward	$\sigma_E/E = 100\%/\sqrt{E} \bigoplus 10\%$
Muon spectrometer	$\sigma_{p_T}/p_T = 10\%$ at $p_T = 1$ TeV

Table 2.1: Performance goal on resolution of each Atlas detector components. The units for E and p_T are in GeV.

y-axis is pointing upwards. The side-A of the detector is defined as that with positive z and side-C is that with negative z. The azimuthal angle ϕ is measured around the beam axis starting from the positive x-axis and the polar angle θ is the angle from the beam axis starting from the positive z-axis. Conventionally, the pseudorapidity η, which is additive under the Lorentz transformation from one reference frame to another, is defined by $\eta = -ln(tan(\theta/2))$. In case of massive objects such as jets, the rapidity $y = 1/2ln[(E + p_z)/(E - p_z)]$ is used instead. The distance ΔR in the pseudorapidity-azimuthal angle space is defined as $\Delta R = \sqrt{(\Delta\eta)^2 + (\Delta\phi)^2}$. Variables with the subscript "T" refer to the transverse plane. Subsequently transverse momentum p_T, transverse energy E_T, or missing transverse energy E_T^{miss} for example are defined in x-y plane. Missing energy refers to the energy of the particles which are not detected but can be deduced from the conservation laws of energy and momentum. The missing energy is a tool to infer the presence of non-detectable particles in the detector.

2.2.1 Inner Detector

The Inner Detector (ID) is located directly outside the beampipe, close to the interaction region where particles are produced. It is designed to provide highly efficient track reconstruction, excellent momentum resolution and a good measurement of the primary and secondary vertices. With a volume of 7 m length and 1.15 m radius immersed in a 2 T magnetic field of a thin superconducting solenoid, the detector

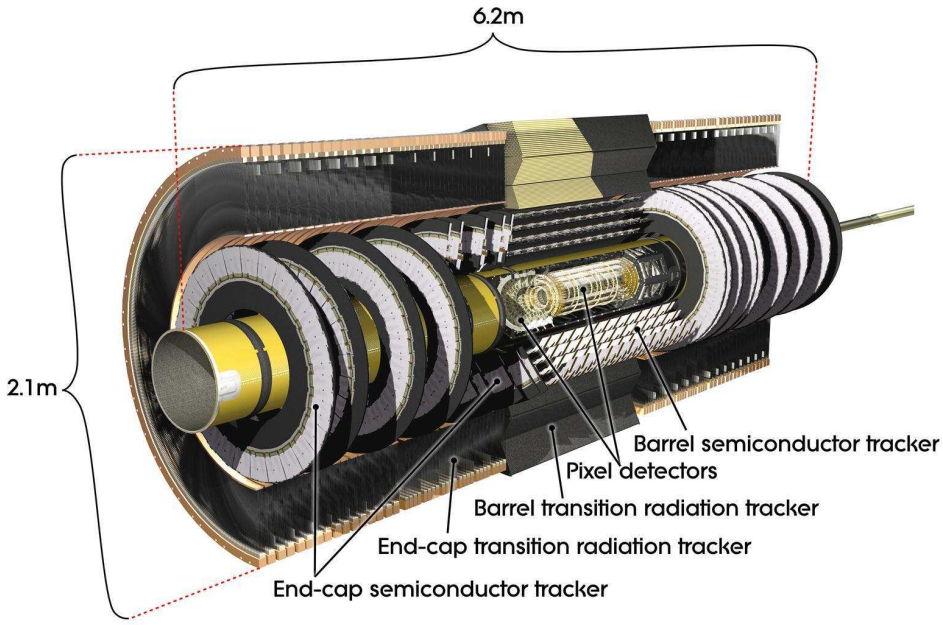

Figure 2.4: Overview of the ATLAS Inner Detector.

covers the pseudorapidity range of $|\eta| < 2.5$. It consists of three independent but complementary sub-detectors, the Pixels, Semi-Conductor Tracker (SCT) and the transition radiation tracker (TRT); see figure 2.4 for an overview of the ID.

At the innermost radii, just around the collision vertex, the pixel detector is placed and delicated to vertex reconstruction. It has a very high granularity in order to track thousands of particles coming from the collisions. The high-precision position measurements per track are achieved by approximately 80 million pixels combined into 1744 pixel modules. The size of each pixel is $50\,\mu m \times 400\,\mu m$. There are 1456 modules in three layers positioned on concentric cylinders around the beam axis in the barrel region and 288 modules in the endcap arranged as six disks perpendicular to the beam axis. The main goal is to measure vertices accurately, determine the impact parameter of tracks and identify long-lived particles such as b-hadrons and τ-leptons.

The SemiConductor Tracker (SCT) is the middle layer of the Inner Detector. A good hit resolution is achieved by thousands of silicon microstrips: 8448 strips build 4 coaxial cylindrical layers in the barrel and 6944 strips spread out over nine wheels on

each side of the endcap. It also provides quick electronic response and good pattern recognition capability. Thanks to SCT system, additional hits in the intermediate radial range are added to make the momentum measurement more precise.

The TRT is at the outermost radius of inner detector. It consists of straw tubes with a diameter of 4 mm and a length of 144 cm in the barrel and 37 cm in the endcap. There are 50000 straws in the barrel and 320000 in the endcap, which typically provide 36 hits per track. The straw tubes are interleaved with transition radiation material which causes high p_T electrons to emit transition radiation (TR), and therefore to yield much larger signal amplitudes. As a result, TRT helps in electron identification by using low or high threshold.

2.2.2 Calorimeter

The Atlas calorimeter system is mainly set up to measure the energies and also the directions of particles that traverse it and interact with the material of the calorimeter. It includes an electromagnetic (EM) and a hadronic calorimeters, see figure 2.5. The EM calorimeter is typically for electron and photon measurements while the hadronic calorimeter is used for identification and energy measurement of hadrons (mainly charged pions). They consist of barrel and endcap parts covering up to $|\eta| < 3.2$. In addition, forward calorimeter is placed at $3.1 < |\eta| < 4.9$ to get a maximal coverage around the beam axis. In the region $|\eta| < 2.4$ which is matched to the ID, the fine granularity of EM calorimeter allows for precise measurements of electron/photon energy and direction. The rest of the calorimeter has coarser granularity that is sufficient to satisfy physics requirements for jet reconstruction and E_T^{miss} measurements.

The Atlas calorimeter employs a sampling technique (sandwiching active material and absorber) which separates the absorption from energy measurement. This provides a compact design and good containment for EM and hadronic showers. With its large coverage up to $|\eta| < 4.9$ and the total thickness of greater than 22 radiation lengths (X_0) in the barrel of EM calorimeter (24 X_0 in the endcap), and about 9.7 interaction lengths (λ) of instrumented material in hadronic calorimeter barrel (10λ in the endcap), the calorimeter contains most final state particles except muons, neutrinos and other particles which do not interact electromagnetically and hadronically.

A particle from collisions going through the tracking detector comes into the

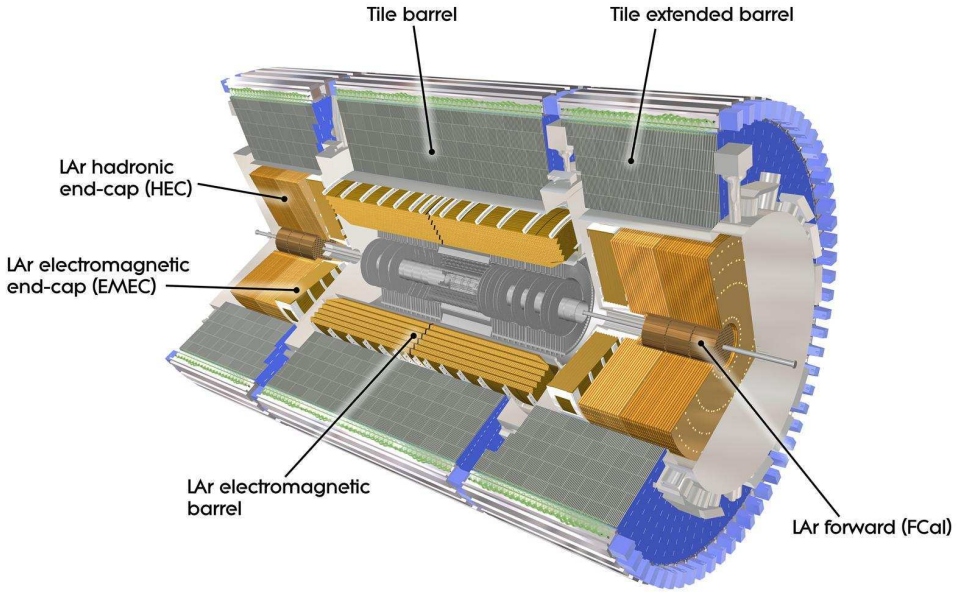

Figure 2.5: Cut-away view of the ATLAS Calorimeter.

calorimeter. It deposits most of the energy in the absorbers of the calorimeter by a chain of interactions with materials which produces a shower of secondary particles. Particle production continues until all the incident particle energy is absorbed. These secondary particles ionize the active medium of calorimeter, then charged particles consisting of free electrons and positive ions drift to electrodes and create electric signals. The energy measurement is performed by calibration of collected signals. The process of particle interaction with materials creates a shower structure, each particle makes different shower shape due to its different behavior of interacting. Particles can therefore be identified by their shower shapes.

2.2.2.1 Electromagnetic calorimeter

This is the main detector to measure electron and photon energies. The calorimeter also measures particle positions. This is particularly important for the case of photons which are not detected in inner detector. The EM showers are created by two processes, bremsstrahlung and pair production. Electrons undergo the bremsstrahlung effect, i.e. when transversing the detector material they can radiate off photons.

	EM calorimeter			
	Barrel		Endcap	
	$\Delta\eta \times \Delta\phi$	$\lvert\eta\rvert$	$\Delta\eta \times \Delta\phi$	$\lvert\eta\rvert$
Presampler	0.025×0.1	$\lvert\eta\rvert < 1.52$	0.025×0.1	$1.5 < \lvert\eta\rvert < 1.8$
First layer	$0.025/8 \times 0.1$	$\lvert\eta\rvert < 1.4$	0.050×0.1	$1.375 < \lvert\eta\rvert < 1.425$
	0.025×0.025	$1.4 < \lvert\eta\rvert < 1.475$	0.025×0.1	$1.425 < \lvert\eta\rvert < 1.5$
			$0.025/8 \times 0.1$	$1.5 < \lvert\eta\rvert < 1.8$
			$0.025/6 \times 0.1$	$1.8 < \lvert\eta\rvert < 2.0$
			$0.025/4 \times 0.1$	$2.0 < \lvert\eta\rvert < 2.4$
			0.025×0.1	$2.4 < \lvert\eta\rvert < 2.5$
			0.1×0.1	$2.5 < \lvert\eta\rvert < 3.2$
Second layer	0.025×0.025	$\lvert\eta\rvert < 1.4$	0.050×0.025	$1.375 < \lvert\eta\rvert < 1.425$
	0.075×0.025	$1.4 < \lvert\eta\rvert < 1.475$	0.025×0.025	$1.425 < \lvert\eta\rvert < 2.5$
			0.1×0.1	$2.5 < \lvert\eta\rvert < 3.2$
Third layer	0.050×0.025	$\lvert\eta\rvert < 1.35$	0.050×0.025	$1.5 < \lvert\eta\rvert < 2.5$

Table 2.2: Granularity versus $|\eta|$ of different layers of EM calorimeter.

Photons can produce electron pairs via pair production, which is a dominant process for high energetic photons. This leads to a shower of electron-photon cascade. The measured energy is proportional to the collected signal at electrodes.

The EM calorimeter is contained in three separate cryostats. ATLAS cryostats, which contain liquid argon, cover the calorimeter and keep the system at the desired temperature. The central cryostat contains the electromagnetic barrel calorimeter, and the two endcap cryostats contain the electromagnetic endcap (EMEC) calorimeters. The barrel spans up to $|\eta| = 1.475$, while the endcap covers $1.375 < |\eta| < 3.2$. The crack region between $1.37 < |\eta| < 1.52$ is affected by additional material needed to instrument and cool the inner detector, and it is usually excluded from analyses that require precise electron or photon measurements. The EM calorimeter is segmented in four sections in depth: the presampler and 3 layers, whose coverage and granularity are detailed in table 2.2. The first layer is finely segmented along η, except for the edge zones of the EMB and EMEC which have a somewhat coarser

granularity. The second layer collects the largest fraction of the energy of the EM shower, and the third layer collects only the tail of highly energetic EM showers and is therefore less segmented in η. As mentioned previously, the direction of photons is determined in this detector part via fine granularity of the first and second layers. Furthermore, a LAr presampler covers the region $|\eta| < 1.8$ to provide an estimation of energy lost due to material interaction in the Inner Detector.

The Atlas EM calorimeter is a lead-liquid argon detector with accordion-shape absorbers and electrodes to provide full ϕ-symmetry without azimuthal cracks. The absorbers are made of lead plates, interleaved with gaps between plates filled with liquid argon. The thickness of the lead plates changes as a function of η in order to limit the decrease of the sampling fraction as $|\eta|$ increases, which assures a uniform performance in terms of energy resolution. The thickness is of 1.53 mm for $|\eta| < 0.8$ and changes to 1.13 mm for $|\eta| > 0.8$ in the barrel. Also, the plates have thickness of 1.7 mm for $|\eta| < 2.5$ and of 2.2 mm for $|\eta| > 2.5$ in the endcap. This geometry provides a very uniform performance in terms of linearity and resolution as a function of ϕ, and allows for a fast extraction of signal at the rear or at the front of electrodes.

The accordion structure plates are designed to have constant LAr gaps in the EM barrel and increases with radius in the end-cap. The liquid argon is kept in the same cryostat as the inner detector solenoid to avoid additional material in front of the EM calorimeter.

The readout electrodes are located in the gaps between the absorbers and consist of three conductive copper layers separated by insulating polyimide sheets. The two outer layers are at the high-voltage potential and the inner one is used for reading out the signal via capacitive coupling.

The EM barrel calorimeter is divided into two half cylindrical barrels. The gap between these two identical half barrels is approximately 4 mm wide in the center at z=0. The length of each half-barrel is 3.2 m, their inner and outer diameters are 2.8 m and 4 m respectively. The half-barrel has been divided into 16 modules, each covering a $\Delta\phi = 22.5°$. The total thickness of a module is at least 22 radiation lengths (X_0), increasing from 22 X_0 to 30 X_0 between $|\eta| = 0$ and $|\eta| = 0.8$ and from 24 X_0 to 33 X_0 between $|\eta| = 0.8$ and $|\eta| = 1.3$.

The EMEC calorimeters are located at the ends of the barrel calorimeter. Each

endcap weighs 27 tonnes, and has an inner and outer radius of 330 mm and 2098 mm, respectively. It has two coaxial wheels: the outer wheel which covers the region $1.375 < |\eta| < 2.5$ and the inner wheel which covers $2.5 < |\eta| < 3.2$. The boundary between the two wheels is 3 mm wide and matches the acceptance of inner detector. Each endcap is further divided into eight wedge-shaped modules without discontinuity in ϕ. The total active thickness of an endcap is greater than 24 X_0 for $|\eta| < 1.475$, and increases from 24 to 38 X_0 for $|\eta|$ increasing from 1.475 to 2.5 (outer wheel) and from 26 to 36 X_0 for $|\eta|$ increasing from 2.5 to 3.2 (inner wheel).

As mentioned above, the presampler is a separate thin liquid-argon layer implemented in front of the EM calorimeter just behind the inner detector to provide shower sampling in front of the active EM calorimeter and inside the barrel cryostat. The presampler fully covers the EM barrel as well as a part of endcap, up to $|\eta| = 1.8$ in order to improve the energy measurement in the transition region between the barrel and the endcap calorimeter where the material in front of calorimeter amounts to several X_0.

2.2.2.2 Hadronic calorimeter

The hadronic calorimeter is designed for reconstruction and energy measurement of particle jets, and the measurement of the missing transverse energy. A hadronic shower is more complicated than an electromagnetic shower because of the complex nature of inelastic hadronic interactions. At high energy, these are characterized by multiparticle production and particle emission originating from nuclear decay of excited nuclei. Due to the relatively frequent generation of π^0, there is also an electromagnetic component in hadronic showers. The hadronic showers penetrate deeper into the detector material and make longer showers in comparison to the electromagnetic showers. For that reason, more material is needed in the hadronic calorimeter.

The ATLAS hadronic calorimeter contains the tile calorimeter, the liquid-argon Hadronic End-cap Calorimeter (HEC) and the liquid-argon Forward Calorimeter (FCal).

Tile Calorimeter which is a sampling calorimeter using steel as the absorber and scintillator as the active medium, is positioned outside the EM barrel calorimeter. As depicted in figure 2.5, the tile calorimeter is split into one central barrel part (5.8 m

wide in axial direction), as well as two extended barrels (2.6 m in length). The gap region between the barrel and extended barrel is instrumented by special modules which are also made of steel-scintillator sandwiches with the same sampling fraction as the rest of the tile calorimeter but the scintillator is thin enough to occupy in the available space in the gap. These devices allow to partially recover the energy loss in the cracks. The readout of the tiles is achieved with optical fibers. Readout cells are built by grouping fibers into photomultipliers and are projective to the interaction point. They provide a granularity of $\Delta\eta \times \Delta\phi = 0.1 \times 0.1$.

The HEC consists of two independent wheels per end-cap, located directly behind the EM end-cap calorimeter. It is a copper-liquid argon sampling calorimeter with a flat-plate design, covering the range $1.5 < |\eta| < 3.2$ and sharing the same cryostat with EM endcap calorimeter. The HEC slightly overlaps with the tile calorimeter ($|\eta| < 1.7$) as well as the FCal ($|\eta| > 3.1$) in order to reduce the drop in material density at the transition between them. The granularity is $\Delta\eta \times \Delta\phi = 0.1 \times 0.1$ for $|\eta| < 2.5$ and $\Delta\eta \times \Delta\phi = 0.2 \times 0.2$ for $|\eta| > 2.5$.

The FCal are located in the same cryostats as the end-cap calorimeters in the range of $3.1 < |\eta| < 4.9$ forming an uniformity of calorimetric coverage. As the FCal modules are located at high η, they are exposed to high particle fluxes. This has motivated a design with very small liquid-argon gaps, which are obtained by using an electrode structure of small-diameter rods, centered in tubes which are oriented parallel to the beam direction. The FCal consists of three modules in each endcap: one EM module (FCal1) and two hadronic modules (FCal2 and FCal3). To optimize the resolution and the heat removal, copper was chosen as the absorber for FCal1. Copper plates are stacked one behind another. An electrode consists of a coaxial copper rod and copper tube separated by a precision, radiation-hard plastic fiber wound around the rod. However, tungsten was chosen as the absorber for FCal2 and FCal3 for the reason of optimizing the absorption length, to provide containment and minimize the lateral spread of hadronic showers. This is achieved by maximizing the amount of tungsten in the modules. These modules consist of two copper end-plates, which are spanned by electrode structures, similar to the ones used in FCal1, except for the use of tungsten rods instead of copper rods.

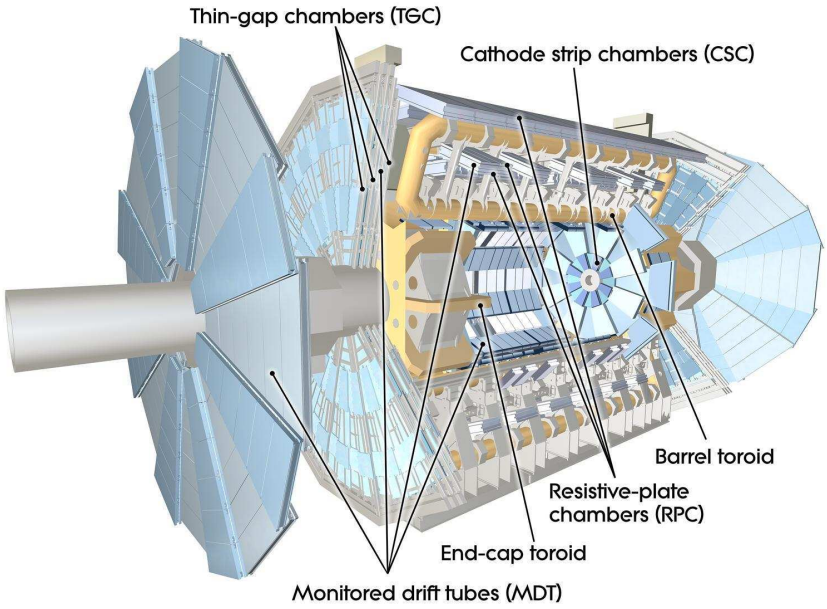

Figure 2.6: Cut-away view of the ATLAS Muon Spectrometer.

2.2.3 Muon spectrometer

The muon spectrometer, the outermost part of the ATLAS detector, is designed to identify and determine the transverse momentum p_T of charged particles escaping the calorimeter, in particular the muon for its strong penetration through materials. In addition, the system is also instrumented to trigger on these particles. Similar to the procedure that uses Lorentz force to measure the momentum in inner detector, it is embedded in a superconducting toroidal magnet system. The general layout of muon system is illustrated in figure 2.6.

The two endcap toroids are inserted at each end of the barrel toroid and line up with the central solenoid. Each of the three toroids consists of eight coils assembled radially and symmetrically around the beam axis. The toroids provide a strong but inhomogeneous magnetic field. The bending power is 1.5 to 5.5 Tm in the barrel range of $0 < |\eta| < 1.4$ and 1.0 to 7.5 Tm in the end-cap region $1.6 < |\eta| < 2.7$. Due to its large volume, the muon spectrometer is able to measure the momenta of highly energetic muons up to 1 TeV at which the bending power of ID is not sufficient to give reliable results.

The trigger and momentum measurements are achieved by 4 different subdetectors using different technologies. A precision track position measurement is performed by Monitored Drift Tube Chambers (MDT's) with the coverage of $|\eta| < 2.7$. In the forward region $2.0 < |\eta| < 2.7$ where the particle density is highest, Cathode Strip Chambers (CSC's) are used instead, as they offer a higher rate capability and time resolution. In addition, Resistive Plate Chambers (RPC's) and Thin Gap Chambers (TGC's) are installed in the barrel and endcap respectively. Their response is very fast and they are therefore used for triggering.

2.2.4 Trigger and data acquisition

The bunch crossing rate at the design LHC bunch spacing is about 40 MHz. It is impossible to record data to tape at this rate because of limits of computing and storage resources. The Atlas trigger is designed to reduce the rate of candidate collisions from 40 MHz to about 200 Hz (300Hz for 2011-2012 data) without losing interesting physics events. The trigger system has three distinct levels. Each trigger level refines the decisions from previous level and applies additional selection criteria. The data acquisition system (DAQ) receives and buffers event data from detector-specific readouts at L1 trigger, subsequently transmits requested data to higher level trigger. Then events passing the EF trigger are moved to permanent event storage. The chain of dataflow from the detector to high level trigger is illustrated by figure 2.7.

- The L1 trigger is typically based on information from muon trigger chambers or the calorimeter to select events with high-p_T muons, electrons, photons, jets or large total transverse energy. It defines regions of interest (RoI) in the detector where high momentum objects are located. Based on the information from the RoI, an event is accepted or rejected. The logic for the L1 trigger is mostly hardwired in the readout electronics, and provides decision times of approximately 2.5 microseconds. It reduces the event rate to 75 kHz.

- The L2 trigger is based on a full readout of the detector in the RoIs that have been identified at L1. This procedure allows to limit the amount of data which are transferred from the detector readout. A fast object reconstruction software

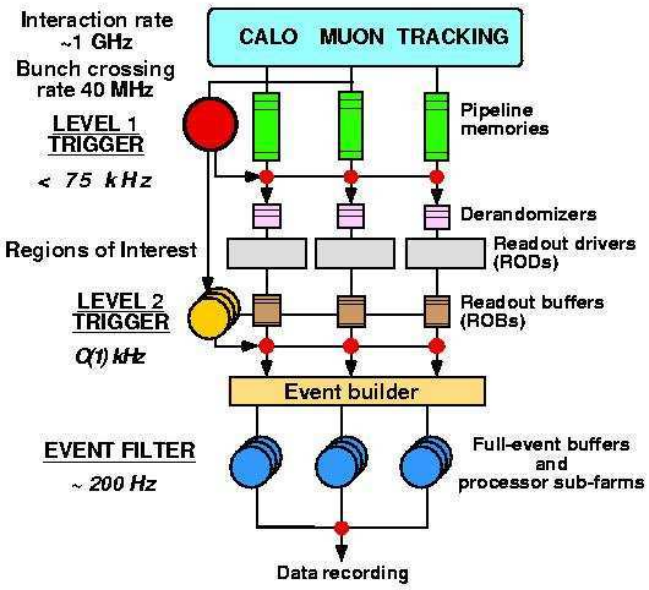

Figure 2.7: Trigger and data acquisition system in Atlas.

is used to better determine the object properties and reduce the fake rate. This takes approximately 40 ms and is used to reduce the event rate to 3.5 kHz.

- The Event Filter (last trigger level) uses full offline object reconstruction to build events and further reduces the event rate to 200 Hz with an event processing time of order of 4 seconds. Events passing the Event Filter with a typical size of 1.3 MB are recorded for subsequent offline analysis.

An exact set of triggers defines a trigger menu. Different trigger menus are used depending on the instantaneous luminosity of the LHC. At the highest luminosities, some low-threshold triggers need to be prescaled. This means that only a fraction of the events accepted are effectively passed to the next level for further processing. A prescale of 1 means that all events selected by the trigger are accepted, while larger prescales mean that only a fraction 1/prescale is accepted.

Most triggers in ATLAS aim to select high momentum particles such as muons, electrons, photons, jets or large missing E_T. The kinematic requirement on these object triggers change in time taking into account the instantaneous luminosity of LHC and the physics program for each data taking period. Events passing at least

one of the ATLAS triggers are stored in data streams corresponding to the type of trigger used to select the event. For example, events selected using muon triggers and are stored in the muon stream. As events can be triggered by different objects, some events are stored in more than one data stream.

2.2.5 Data production and Monte Carlo simulations for analysis

Raw data, which are the output of high level trigger, are classified into streams. At this stage, data are located in local storage and then processed by Atlas reconstruction software producing a format which is called ntuple and which is designed for efficient analysis.

We define a Good Run List (GRL) in terms of data quality for analysis. GRL is a list of run numbers and luminosity blocks [1] in which the events are considered as "good" according to the Atlas Data Quality status. The data were flagged with color, typically green, yellow or red during reconstruction. Green refers to good data while red implies bad data that should not be used. Yellow means degraded data which could be recovered. There are three elements that play important roles in data quality decision. They are Detector Control System (DCS) information, like power supply strips, noise bursts, etc., detector coverage and the removal of parts of detector during a run [44]. Additionally, the GRLs may differ from one physics analysis to another due to different subsystems employed.

In addition, a trigger menu is applied during the data reconstruction. Each event has been marked whether or not it passes a specific trigger type. This offers a further data preselection to select considered events among a tremendous numbers of uninterested events.

Monte Carlo (MC) samples are computer simulated events which are generated for comparison with real data. A good MC sample which agrees well with data is a powerful tool for analysis. It is used to test and validate the analysis method. In addition, MC simulations are used to estimate the amount of data needed to reach

[1] Luminosity block is Atlas interval time in which the luminosity is supposed to remain constant. One luminosity block contains roughly 1 minute of data taking, but this can vary due to run conditions and other operational issues.

the discovery or exclusion sensitivity. Normally, MC simulations model background and signal processes separately. In general, MC samples are produced through a full chain of steps: generation, detector simulation, digitization and reconstruction. The final step produces the event ntuples with the same format as data.

Chapter 3

Photon object

The Atlas detector is used to identify many different physical objects such as electrons, photons, jets and muons, etc. Identification of a given type of object typically combines information from several subdetectors. There are dedicated algorithms which are run for different object identification in Atlas software. This chapter will discuss the photon reconstruction and identification processes which are relevant to this thesis. Photons are reconstructed mainly based on EM calorimeter reconstruction which is described in the first section. The following sections discuss the photon identification techniques and the isolation variable. The identification aims to discriminate good photon candidates against background objects. The isolation energy variable provides an even stronger power of discrimination of photons from jets. Finally, a study of cluster position bias and resolution will be discussed in detail for the collision data collected in 2011.

3.1 EM Calorimeter reconstruction and calibration

Clustering is the starting point of reconstruction and calibration of EM calorimeter, as well as of the selection of electron and photon candidates. It forms rectangular clusters with a fixed or flexible size, depending on the algorithm and on the cluster position. The cluster size is chosen as to maximize the amount of energy within it. There are two alternate algorithms available in Atlas [45].

- **Sliding-Window algorithm** is based on summing cells within a fixed-size rectangular window. The position of the window is adjusted so that the contained transverse energy is a local maximum. This algorithm is later used for electron and photon (collectively called "egamma") identification. It proceeds in three steps: tower building, pre-cluster (seed) finding and cluster filling. In the first step, the calorimeter is divided into a grid of $N_\eta \times N_\phi$ elements of size $\Delta\eta \times \Delta\phi = 0.025 \times 0.025$. The tower energy for each element is calculated by summing the energy of all cells in all longitudinal layers. The information about each tower is stored in a CaloTower object. Then, a window of fixed size of 5×5 (in units of the tower size) is moved across each element of the tower grid defined above in steps of $\Delta\eta$ and $\Delta\phi$. A precluster is formed if the transverse energy inside the window is a local maximum and above a threshold of 3 GeV. The size of the window and the threshold have been optimized to obtain the best efficiency for finding preclusters, and to limit the rate of fake preclusters due to noise. The position of preclusters is calculated by the energy-weighted η and ϕ barycenters of all cells within a smaller window size of 3×3 around the central tower. If two preclusters have positions within a distance $\Delta\eta \times \Delta\phi = 2 \times 2$, only the one with larger energy is kept. The final step is EM cluster formation. The position of the pre-cluster is used as the seed for the final cluster. The EM cluster is filled with cells located in the rectangle of different size depending on whether the cluster position is in the barrel or endcap region, also on the hypothesized particle type (electron, converted or unconverted photon). The choice of the size for optimization has taken into account two competing effects. The cluster should be large enough so that it contains most of the energy deposited by the particle in the calorimeter, thus limiting the effect of lateral shower fluctuations on the energy resolution. However, including more cells also means including more noise.

- **Topological algorithm** creates, in contrast to the sliding-window algorithm, clusters of flexible size by grouping neighboring cells that have significant energies compared to the expected noise. This algorithm is dedicated to jet and missing transverse energy reconstruction and proceeds as follows. A signal over noise ratio is used as parameter of finding clusters. It starts with seeding cells

where this ratio is large over a threshold t_{seed}. A cluster is built iteratively by adding neighboring cells with signal to noise ratio above $t_{neighbor}$ and finished by including all direct neighbor cells on the outer perimeter with signal to noise above t_{cell}. In the standard ATLAS reconstruction, the electromagnetic "633" clusters are built, where each number in "633" corresponds to the ratio of signal over noise of t_{seed}, $t_{neighbor}$, and t_{cell} respectively. The cluster maker step is ideal for the isolation object situations. However it is not the typical case for most events. Especially in the endcap and forward calorimeters, clusters could grow to cover large areas of the detector because they contain adjacent objects. A cluster splitting algorithm is designed to deal with the overlapping shower effect and individual particles may still be separable if they are far apart enough to form local maxima in the calorimeter.

3.2 Photon identification

The photon identification aims to separate real photons from electrons or jet background. As discussed in chapter 2, shower-shape information from calorimeters are used to select electron and photon candidates. Additionally, EM objects can be recognized as electrons or photons by requiring that electrons have an associated track but no associated conversion and, in contrast, that photons have no matched track or a converted track reconstruction. The terminology "conversion" here is in the meaning of photon conversion. In the presence of material in front of calorimeter, photons have a possibility to turn into an electron/positron pair via pair production at any point in the inner tracker. Consequently, these photons, the so-called converted photons, have one or two associated tracks but can be distinguished from electrons by a conversion reconstruction algorithm [46].

For photons, all properties are derived from calorimeter information [47]: the energy as well as the position. Moreover, the very fine granularity in η of the first layer of EM calorimeter also helps with separating diphoton resulting from π^0's decay from isolated photons. A set of identification criteria based on shower shape variables in calorimeter is defined to optimize the photon identification or γ/jet separation (these cuts are also equivalent to the criteria related to EM calorimeter for tight electron

identification). In addition, track isolation from ID is used to improve this rejection.

- **Hadronic leakage** is defined as the ratio of transverse energy in the first layer of hadronic calorimeter to that of EM calorimeter. Real photons are primarily contained in EM calorimeter while jets containing hardons can penetrate deeper into the calorimeter and deposit significant energy in the hadronic calorimeter.

- **Variables using the second layer of the EM calorimeter.** Most of the photon energy is deposited in the second layer of the EM calorimeter. For this reason, two variables can be used:

  - Lateral shower shape variable R_η is given by the ratio of the energy reconstructed in 3×7 cells to the energy deposited in 7×7 because real photons deposits most of their energy in a window 3×7 (in units of cells). This ratio is typically larger than 0.9 for photons.
  - Lateral shower shape variable R_ϕ is the ratio of the energy reconstructed in 3×3 cells to the energy in 3×7. Due to the effect of the magnetic field increasing the width of the converted photon contributions in the ϕ direction, R_ϕ is less discriminating than R_η.
  - Shower width in η direction w_2 is defined by the width of the energy distribution in η in the second sampling of the EM calorimeter.

- **Variables using the first layer of the EM calorimeter.** As discussed above, using variables from hadronic calorimeter and second layer of EM calorimeter can reject jets containing π^0 with high energy and wide showers. The first layer, with its extremely fine granularity in η, is very powerful to detect substructure within a shower. It thereby gives high efficiency in discriminating γ against π^0. One might find two local maxima within jets resulting from π^0 decay into two photons. To search for and reject jets having a second maximum, the shower is studied in a window $\Delta\eta \times \Delta\phi = 0.125 \times 0.2$ around the hottest cell to look for a second maximum. If more than two maxima are found the second highest maximum is chosen. The following variables are used:

  - The difference between energy associated with the second energy maximum and energy reconstructed in the strip with the minimal value between the

first and second maximum $\Delta E_s = E_{max2} - E_{min}$.

- The corrected energy of second maximum as a function of transverse energy of cluster to minimize its sensitivity to fluctuations $R_{max2} = E_{max2}/(1 + 9 \times 10^{-3} E_T/GeV)$.
- The shower width w_{stot} determined in a window that covers 2.5 cells of the second layer of the EM calorimeter (typically 20 strips in the barrel).
- The fraction of energy deposited outside the shower core of three central strips $F_{side} = [E(\pm 3) - E(\pm 1)]/E(\pm 1)$. $E(\pm n)$ is the energy deposited in $\pm n$ strips around the strip with highest energy.
- The shower width for three strips around the maximum strip defined as $w_{s3} = \sqrt{\sum E_i \times (i - i_{max})^2 / \sum E_i}$, which is expressed in units of strip cells. The index i is the strip identification number, i_{max} is the identification number of the most energetic strip, and E_i is the energy deposited in strip i.

The distributions of these discriminating variables for photons and jets are shown in figure 3.1.

There are also two other methods for identification: the Log-likelihood-ratio-based and the Covariance-matrix-based methods. These methods are based on the above listed shower-shape distributions for the identification to define a log-likelihood-ratio parameter for the former method or a covariance matrix (H-matrix) in the later. The cut is applied on new defined parameters instead of the shower-shape variables themselves, find details in Ref. [48].

We defined the selection criteria on the shower shape variables to categorize photons as "loose" or "tight". The "loose" definition mainly uses the variables of hadronic leakage and of the second sampling of the EM calorimeter in the selection. The "tight" definition comprises all criteria as the "loose" and in addition uses the variables of the first sampling of the EM calorimeter. Details can be found in Ref. [49]. Tight selection means all criteria have been satisfied and provides the best capability to identify true photon candidates. If only a subset of criteria has been passed (typically the hadronic leakage and variables of the second layer of EM calorimeter), photons are identified as loose candidates which have a more ambiguity in separation from different objects.

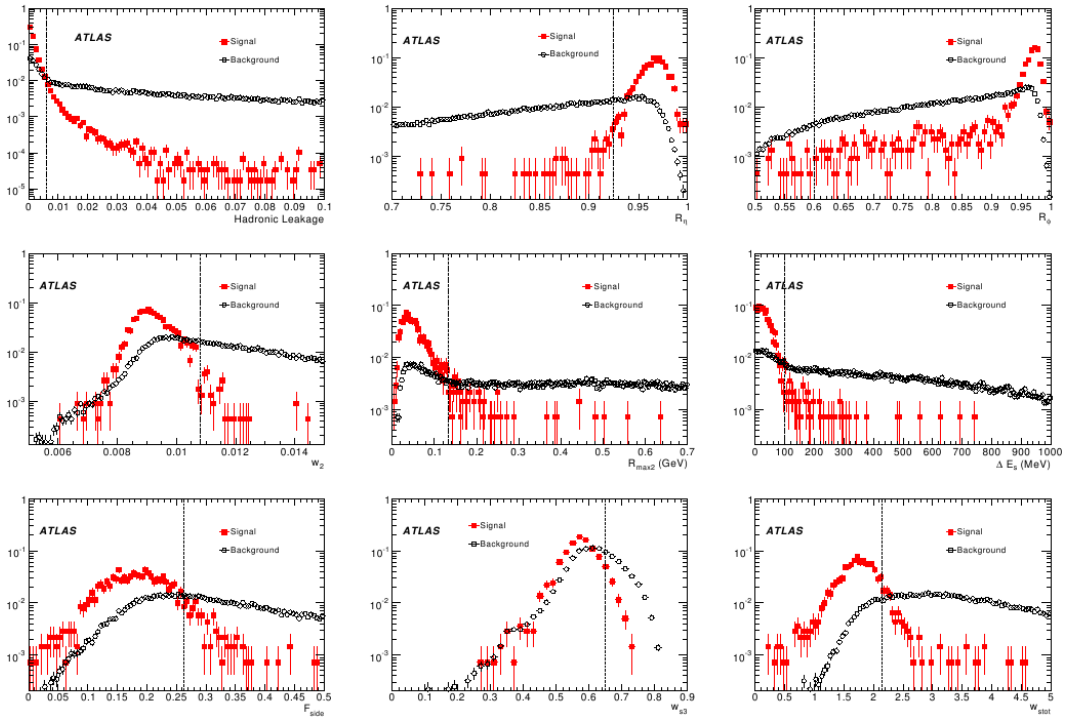

Figure 3.1: The normalized distributions of calorimetric discriminating variables in the region $0 < |\eta| < 0.7$ for $20 < E_T < 30$ GeV for true and fake photons [48].

3.3 Photon isolation

After identification, photons are distinguished from jets. The performance of γ/jet separation is higher if isolation is required around the EM shower as additional criteria. The isolation energy is defined as the sum of the calorimeter transverse energy within a cone of a radius $R_0 = \sqrt{\Delta\eta^2 + \Delta\phi^2}$ around the photon direction (the definition is the same as in the electron case).

Two kinds of isolation energy are defined [50]:

- The cell-based isolation: the sum of energy (without any noise suppression) of all cells within the cone around the cluster barycenter, excluding a 5×7 grid of cells in the center of the cone. Cells from the EM and hadronic calorimeters are included, except cells from the TileGap3.

- The topoCluster-based isolation: the sum of energy of cells belonging to topological clusters whose barycenters are located in the cone. Energies are calibrated at the electromagnetic scale and only positive energy topoclusters are used.

This is a powerful variable which is used to distinguish direct electrons and photons produced in the hard process from fake or non-direct electrons and photons coming from jets (in hadronic decays). For direct electrons and photons, there is typically no energy deposited in this cone, apart from low-energy objects coming from the underlying event, multiple interactions and pileup collisions (the so-called pileup noise). In case of fakes and no-direct candidates, this energy is potentially large due to an additional energy contribution coming from the accompanied objects in the jet. Therefore, the isolation energy of true photons (or electrons) is, as expected, smaller than that of fake jets. The typical isolation energy distributions of true and fake photons are illustrated in figure 3.2.

Most of the photon energy is contained in a cluster size of 5×7. In the case of very high energy objects, it is possible that the energy shower leaks outside this cluster and contributes in the isolation energy calculation. Besides, the isolation energy is also affected by readout electronic noises, especially pileup dependence [51, 52]. As a result, in the usage of isolation energy, it is necessary to apply corrections accounting for the influence of these effects.

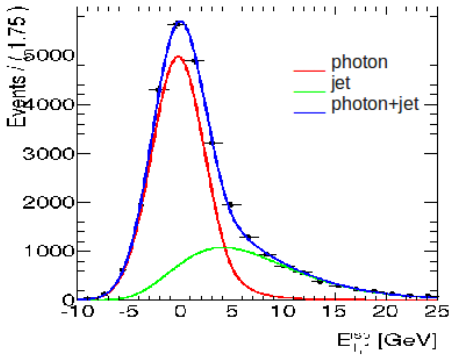

Figure 3.2: Isolation energy distributions of true (red) and fake (green) photon candidates observed in tight photon data sample.

In addition, the contamination of inclusive jets could be alternatively rejected by an additional track-isolation variable. It is defined as the sum of all p_T track ($p_T > 1$ GeV) within $\Delta R < 0.3$, where ΔR is the η-ϕ distance between the track vertex and cluster center. The imposition on p_T is to minimize the effect of pileup and underlying events.

3.4 EM cluster position study

As mentioned, EM calorimeter is an important subdetector in Atlas to probe photons and measure their energy as well as their position. The position is calculated by examining the energy weighted on cells of calorimeter cluster [53, 54]. The cluster position plays a main role in photon direction determination and vertex measurement. Therefore, the cluster position study is considered in my calibration study [55]. It starts with the cluster position bias study by using the well-measured track positions (extrapolated to the calorimeter) as a reference and examining the track-cluster position matching. This study is also a necessary ingredient of electron identification process. A following step which is to quantify the cluster resolutions is carried out as well.

3.4.1 Data and Monte Carlo simulation samples

The study is performed on electrons selected from candidate $W \rightarrow e\nu$ events which provide a sizable sample of pure electrons. We use data collected in 2011 campaign and the corresponding $W \rightarrow e\nu$ Monte Carlo (MC) sample for this study. The MC is simulated (by PYTHIA generator) consistently with detector configurations as in data in order to obtain the best estimate of data.

3.4.2 Event selection

After passing the trigger, events are selected in lumiblocks which are marked as good data quality. Events affected by LAr noise burst and data corruption are rejected. Events having vertex with at least three tracks are chosen. Events with bad reconstructed jets, which result in lower precision on missing transverse energy (MET) calculation [1], are also removed. Following the general selection, more stringent selections based on electrons are applied. Electron objects falling into dead regions of detector (OTX) are rejected. Only events that have exactly one high-p_T electron ($p_T > 20$ GeV) outside the crack region ($1.37 < |\eta| < 1.52$) are chosen. Electron is additionally required to satisfy tight identification criteria and to be isolated. Then events are eliminated if the measured MET is lower than 25 GeV. And finally events must have transverse mass $m_T > 40$ GeV to reach criteria of W candidates. Figure 3.3 shows the transverse mass of W candidates with background estimated fully from MC samples. The electron impurity is dominated by QCD dijet background when a jet is misidentified as an electron in reconstruction step. QCD estimation is performed based on dijet sample using Pythia generator. It gives approximately 89% on electron purity.

3.4.3 Track-Cluster matching

In order to evaluate the bias on cluster-based position reconstruction in LAr calorimeter, it is useful to compare to a quantity which provides an unbiased measurement.

[1] The MET in this analysis is the refined calibration version of the cell-based MET reconstruction including contributions from transverse energy deposits in the calorimeters, corrections for energy loss in the cryostat and measured muons. Details of the definition can be found in Ref. [56].

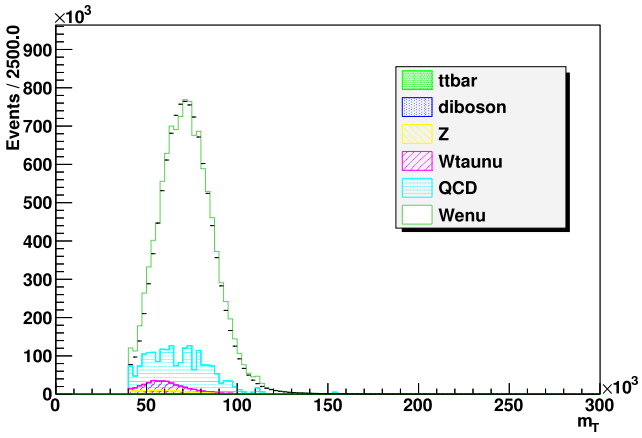

Figure 3.3: Transverse mass distribution of W candidates.

By assuming that inner detector with pixels and silicon trips give high precision on track position, we perform a study on difference in position between clusters where electron deposits energy in calorimeter and the corresponding reconstructed track of that electron in inner detector.

3.4.3.1 $\Delta\eta$

$\Delta\eta$ between cluster and track is calculated taking into account a parametrization in the depth of each layer [57], and also the displacement in z of the origin of the track comparing to the origin of the coordinate detector system. The luminous region of LHC is spread a few cm along the z direction. Track parameters are usually reported with respect to the vertex where track originates, while cluster positions are always expressed with respect to the detector origin. We therefore apply a correction in η_{cl}, to change it into a new one with respect to the coordinates of track vertex. Figure 3.4 shows a comparison of mean bias in η of two first samplings of calorimeter compared to the track measurements. It is known that η is corrected for the S-shape in Atlas reconstruction [53, 54]. The S-shape structure is due to the finite granularity of cluster cells of calorimeter, it gives rise to a systematic shift of the shower center toward the center of cells. In order to check the validity of this correction, figure 3.5 displays a zoom in one cell (both sampling 1 and 2) of figure 3.4 for data, and it does not show any residual S-shape explicitly. This means that the S-shape correction, which

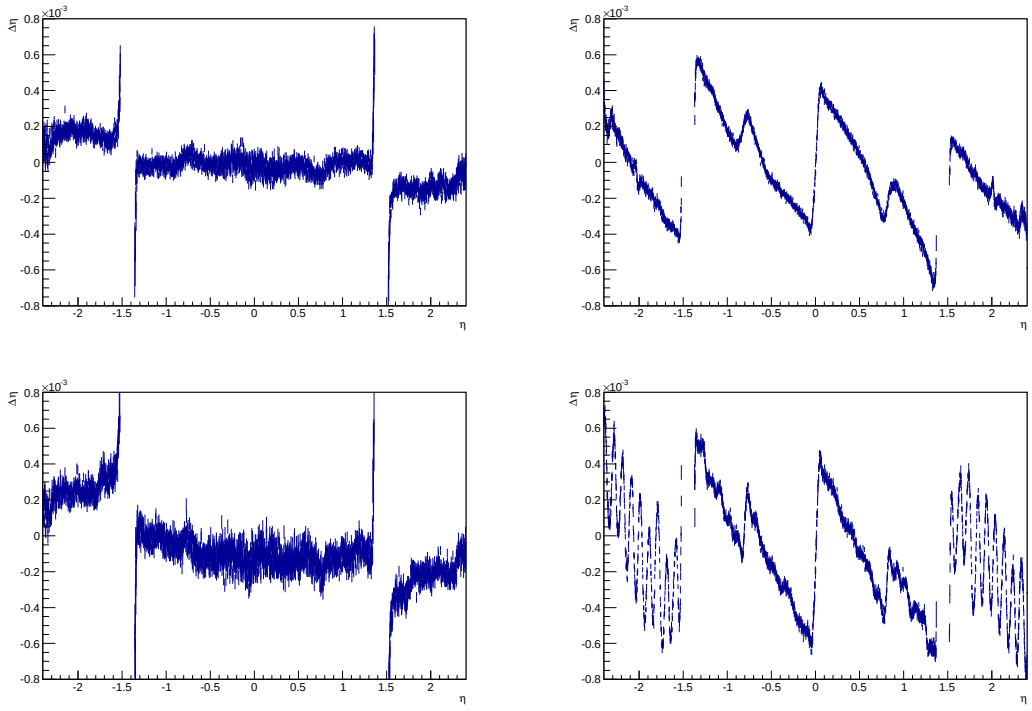

Figure 3.4: Mean in η comparing data/MC in: sampling 1 in MC on the top-left, sampling 1 in data on the top-right, sampling 2 in MC on the bottom-left and sampling 2 in data on the bottom-right.

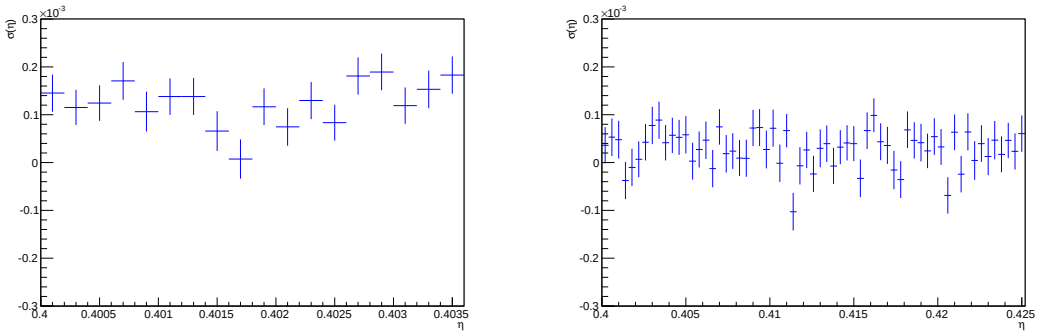

Figure 3.5: Mean of $\Delta\eta$ versus η with one cell size zoom of sampling 1 (left) and sampling 2 (right) for data.

is derived from simulation, works well for collider data.

In figure 3.4, data has definitely a wider range of variation than MC, and clear discontinuities in the region where the absorber thickness in the barrel changes (at $|\eta| = 0.8$) and the transition region between cryostats ($1.37 < |\eta| < 1.52$). A 4-cell periodicity is seen in the end-cap region of sampling 2 in data but not in MC. The origin of these oscillation is not understood. One detector feature with 4-cell periodicity is the connections to summing boards [58], which is probably relevant. This effect will be visible again in next study on $\Delta\phi$ versus ϕ plot. The bias is least at the module center of detector and larger gradually to the boundary, which can be interpreted in terms of an imperfection in detector geometry length of the barrel half-modules. The maximum bias read in figure 3.4 is about 0.6×10^{-3} in η, translating into the longitudinal coordinate which is about 0.96 mm. It is reasonable to explain that the module size of detector is constructed in precision within the order of mm.

Figure 3.6 shows a combination of resolutions in η-position of both cluster calorimeter and inner tracker. First layer with finer granularity consequently has better resolution than second layer.

3.4.3.2 $\Delta\phi$

Electron cluster ϕ position is different from electron track ϕ due to the effect of bending of charged particles in magnetic field. Accounting for the influence of this effect, $\Delta\phi$ is calculated with new track ϕ-position at the point where the track enters

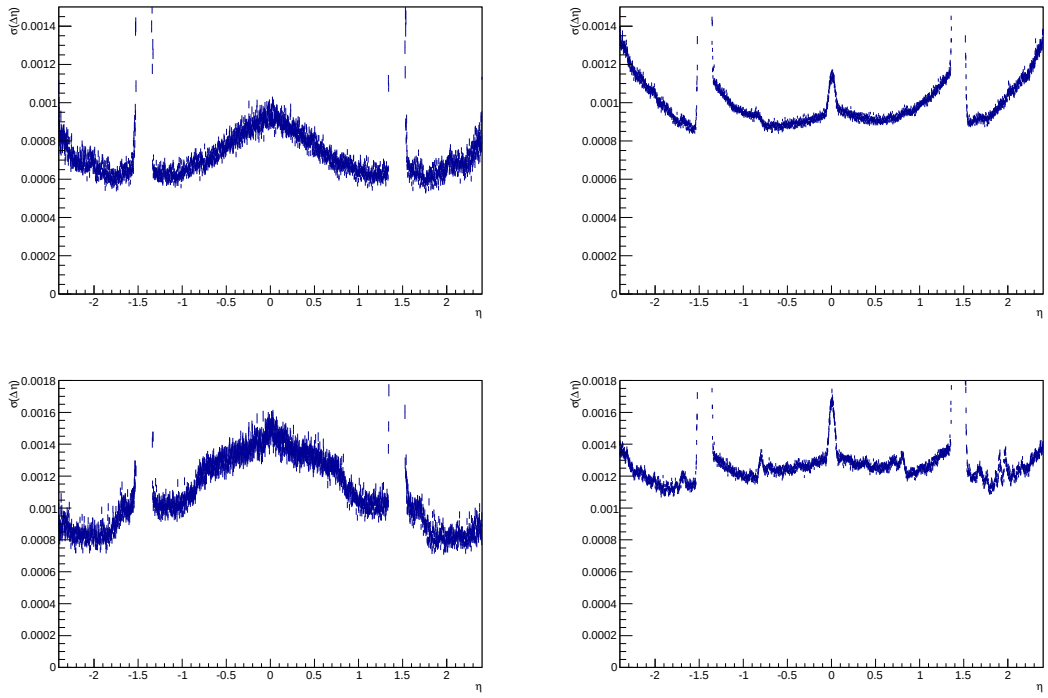

Figure 3.6: RMS in η in sampling 1 (top) and sampling 2 (bottom), comparing data (right) to MC (left)

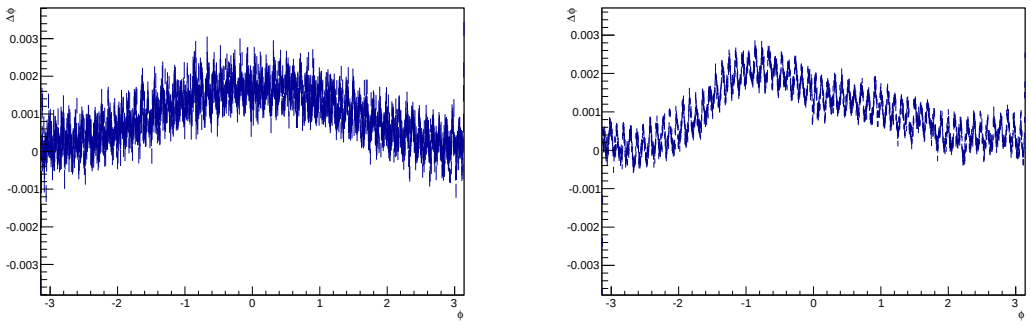

Figure 3.7: Mean on ϕ in sampling 2 for data (right) and MC (left).

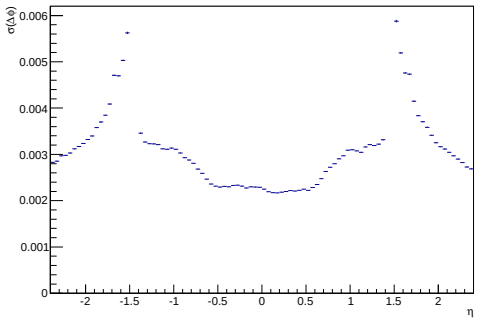

Figure 3.8: RMS on ϕ in sampling 2 for data in η direction.

the calorimeter. Moreover, accounting for the effect of bremsstrahlung possibility in inner detector, we use the electron E_T measured in EM calorimeter, instead of the electron p_T measured in ID, in the calculation to compensate the energy lost due to photon emission.

Only the $\Delta\phi$-mean bias on middle layer, which has fine segmentation in ϕ, is shown, see figure 3.7. Again 4-cell periodicity is exposed in this layer corresponding to the separation of summing boards [59, 60]. As opposed to η-direction, the detector is pretty uniform in ϕ, so it is not surprising that there are no big structures in this direction. However, $\Delta\phi$ resolution does depend on η corresponding to the change of shower depth, as shown in figure 3.8.

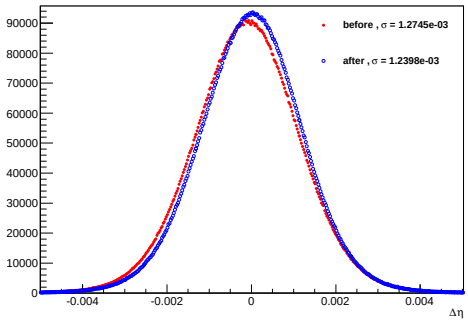

Figure 3.9: Comparison on RMS of $\Delta\eta$ before and after mean bias correction applied on data.

Correction of mean bias in η-direction in sampling 2

We have seen a wider variation on mean of $\Delta\eta$ in data comparing to MC and also an unexpected oscillation in end-cap in sampling 2. This bias is of the order of its resolution. A correction is applied to data to check if it leads to any improvement in resolution. η_{cl} is added an amount that corresponds to the mean value at that η bin obtained by figure 3.4. A small gain of resolution is observed after this correction, as shown in figure 3.9.

3.4.4 Cluster position resolution

The position resolution in EM calorimeter can be extracted from the distributions of comparison between cluster and track shown in the previous section, assuming the track position resolution of inner detector is known. We now demonstrate that the track resolution is comparable to that of cluster. It contributes significantly to the cluster-track distributions in figure 3.6. Figure 3.10 shows the MC simulated resolution in η-direction for the cluster and track separately. Indeed, the track η resolution is not negligible compared to the cluster resolution. As a consequence, track resolution needs to be known precisely in order to derive the cluster resolution from the $\Delta\eta$ distribution.

The track position resolution had been studied in detail with cosmic data in 2008 [61]. However the results have not been updated for current state of detector in 2011. We have performed the same procedure as the cosmic ray note [61] to get

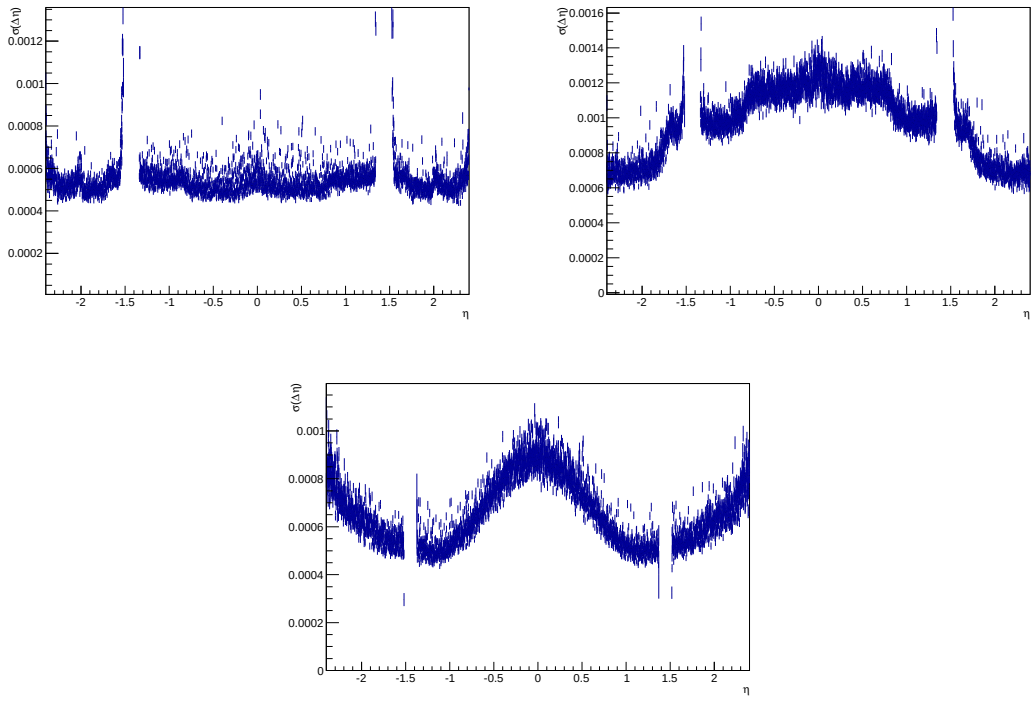

Figure 3.10: Resolution on η direction estimated by MC for cluster (sampling 1 on the top-left and sampling 2 on the top-right) and for track at bottom

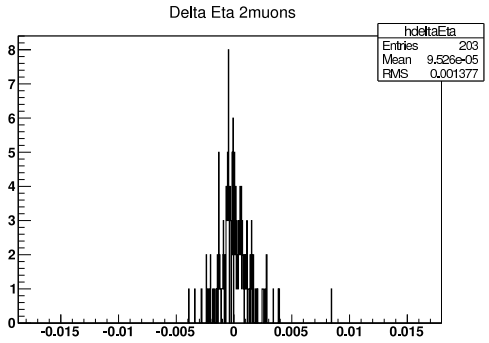

Figure 3.11: $\Delta\eta$ of two cosmic muons which are selected from the cosmic stream of full 2011 data.

the real track position resolution for 2011 data, using cosmic muons from `IDcosmics` stream recorded during inter-fills of colliding proton beams. The idea is that cosmic muon descending through the center of detector is reconstructed as two separate muons originating from detector center, then comparing track parameters of these gives their resolution. A tight selection of tracks is applied to guarantee that they travel through the components of inner detector. Figure 3.11 shows $\Delta\eta$ plot of two combined muons considered as originating from an unique one. It is expected to have mean value at zero and the RMS is a measure of track resolution on η. This plot has been made with all 2011 data taking periods, but only 203 entries satisfied the selection. With this limited statistics it is definitely not possible to parameterize the resolution as a function of η. We therefore turn to another control sample that allows us to compare the track direction resolution in data and MC.

We can exploit the standard and abundant $Z \rightarrow ee$ sample where both two electron tracks originate from a common primary vertex. In contrast to the sample of cosmic muons discussed above, there is no simple relation between the values of η (or ϕ) of the two tracks. But their longitudinal and transverse impact parameters, z_0 and d_0 respectively, with respect to the primary vertex should theoretically be equal to zero. Δz_0 between the two electrons can be used to estimate the track z_0 resolution. Comparing data versus MC gives a scale factor which is listed in table 3.1. We use it as an estimation of the scale factor for the track η resolution. To check the validity of this assumption, the correlation coefficient between the longitudinal impact parameter z_0 and the polar angle θ of track $\rho(z_0, \theta)$ has been studied and displayed in figure 3.12

$\|\eta\|$	scale factor	$\rho(cl, trk)$
0	1.0054±0.0083	0.2570
0.2	0.9996±0.0081	0.2750
0.4	1.0312±0.0087	0.2440
0.6	1.0860±0.0099	0.2250
0.8	1.1476±0.0117	0.2153
1.0	1.1992±0.0151	0.2367
1.2	1.2359±0.0247	0.2116
1.4	1.2266±0.0246	0.1709
1.6	1.2801±0.0192	0.2360
1.8	1.2052±0.0172	0.2595
2.0	1.0785±0.0162	0.2728
2.2	0.9913±0.0236	0.3556

Table 3.1: Scale factor data vs MC extracted by $\Delta z0$ distribution and correlation factor between cluster and track as a function of η.

proving that z_0 and θ are strongly correlated. It is consequently possible to use the scale factor from the Δz_0 study as a reliable estimate of the scale factor of the track η resolution. There are two populations in figure 3.12, the one with less correlation corresponds to tracks in central region while the other refers to tracks more forward to end-cap. This implies that systematic uncertainty on the $\Delta\eta$ scale factor in table 3.1 in small η region would be higher than for larger η (simply because the scale factor from z_0 resolution is less reliable estimate of the scale factor for η resolution).

The RMS of $\Delta\eta$ between cluster and track in figure 3.6 is a combination of resolutions of each separated component. In general, it follows the error propagation formula [62]

$$\sigma^2_{cl-trk} = \sigma^2_{cl} + \sigma^2_{trk} - 2\rho(cl, trk)\sigma_{cl}\sigma_{trk} \tag{3.1}$$

where $\rho(cl, trk)$ is correlation coefficient between cluster and track fluctuations. Ideally cluster and track would be independent variables and correlation term in equation 3.1 would vanish. We use MC to quantify the correlations. The correlation coefficient can be quantified by a 2-D histogram made by MC in figure 3.13. It slightly depends on η as shown in table 3.1. Finally cluster resolution is obtained by

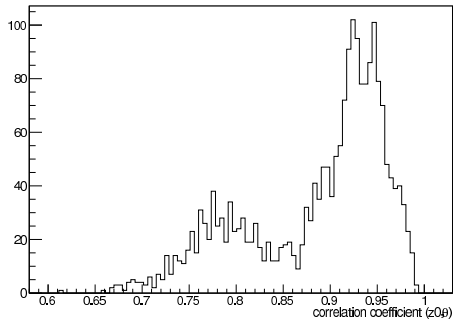

Figure 3.12: Correlation factor between $z0$ and θ parameters of track.

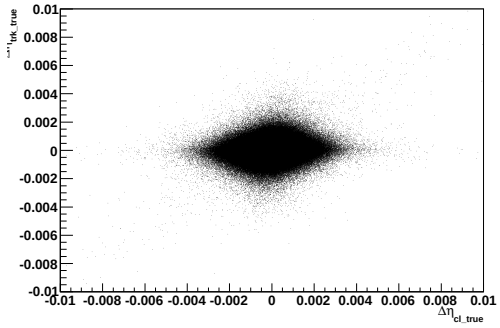

Figure 3.13: 2-D correlation histogram of cluster and track η resolution

solving the above equation for σ_{cl}. The result is displayed in figure 3.14.

Compared to the values determined by MC, the data distribution has more variation in sampling 1 while it is flat in MC. The resolutions (in both two samplings) are comparable in data and MC for central η and the quality of agreement degrades as η increases (the resolution is worse in data). For example, in the first sampling, the η resolutions are estimated roughly 0.0006 in MC and degrade gradually up to $\sim$0.001 in data. In the second sampling, these values refer to $\sim$0.001 in MC and degrade to $\sim$0.0012 in data [2]. The systematic uncertainty in this study is mainly due to the use of scale factor from Δz_0 to constrain the resolution in η. As discussed above, a larger correlation between z_0 and θ (or η) parameters of track means that use of the scale

[2]We just made quantitatively comparisons between data and MC in the barrel region $0.8 < |\eta| < 1.37$ where the position measurement is more precise and the systematic uncertainty in our calculation is small.

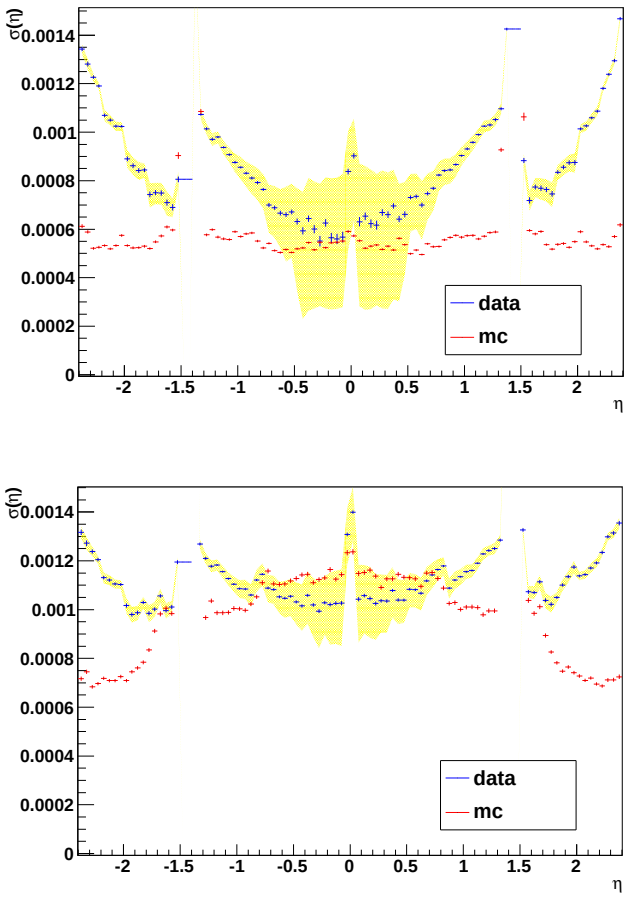

Figure 3.14: The estimation of cluster resolution of η position from data (in blue) for sampling 1 (top) and sampling 2 (bottom). The band represents the systematic uncertainty estimation. The MC simulation is superimposed (in red).

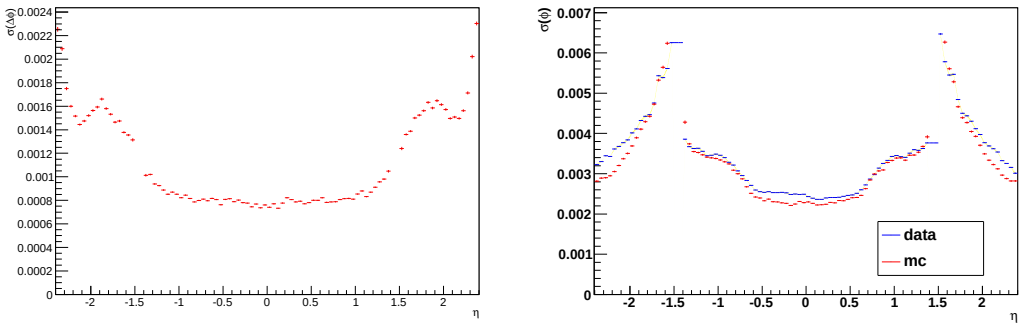

Figure 3.15: Resolution of ϕ position for track estimated by MC is on the left, and for cluster sampling 2 is on the right.

factor from Δz_0 for η is more reliable and the corresponding systematic uncertainty is smaller.

The same procedure is applied for ϕ direction calculation. The data/MC scale factor used for ϕ_{track} resolution estimation is extracted by Δd_0 instead, because these two parameters are strongly correlated. The cluster resolution in ϕ direction is shown in figure 3.15, only sampling 2 has been examined because ϕ granularity is best in this layer. It is obvious that cluster resolution in ϕ is the main component contributing to the common cluster-track resolution plot.

In conclusion, a measurement of bias and resolution on cluster position has been studied. An unexpected bias oscillation with 4-cell periodicity is seen for sampling 2 in endcap, but it does not impact significantly the resolution. The cluster position resolution has been quantified from data. It shows that data and MC are in agreement for central region and the degradation of agreement is higher for forward region.

Chapter 4

Diphoton analysis for LED

This chapter will describe the diphoton final state analysis with the aim of searching for LED. Data and MC samples used in this analysis are introduced in section 4.1. Next section will list the selection criteria used to isolate diphoton events. The signal and background studies are respectively discussed in detail in section 4.3 and 4.4. There will be a section 4.5 which specifies for the study of systematic uncertainties arising in signal and (or) background determination. Finally the results of the analysis will be presented in section 4.6.

4.1 Data and Monte Carlo simulation samples

The data used in this analysis correspond to the full 2011 dataset of `egamma` stream [1] with the center-of-mass collision energy $\sqrt{s} = 7$ TeV. The integrated luminosity of data reached 4.91 fb^{-1} by the end of 2011. The data are preselected with a Good Run List (GRL) which is recommended by the ATLAS egamma working group [63].

The ADD signal samples are generated using the Sherpa generator [64]. They are listed in table 4.1 with the corresponding cross sections. According to the equation 1.11, these cross sections should reflect as a polynomial function $\mathcal{O}(2)$ of $1/M_S^4$. The symbol M_{cut} denotes a parameter of the generator, it restricts the center-of-mass energy of the hard process to be below this specified scale. We generated samples

[1] `egamma` stream is an Atlas jargon which refers to the data stream collected by triggering on EM calorimeter.

Dataset number	n_{ED}	M_S (TeV)	M_{cut}(TeV)	KK Convention	σ (fb)
145068	2	2.5	2.5	Hewett-	154.98
145069	2	3.	3.	Hewett-	152.86
145070	2	3.5	3.5	Hewett-	158.60
145071	2	4.	4.	Hewett-	154.32
145072	2	4.5	4.5	Hewett-	154.31
145073	2	5.	5.	Hewett-	156.05
145076	2	2.5	2.5	GRW	174.05
145077	2	3.	3.	GRW	160.42
145078	2	3.5	3.5	GRW	159.74
145079	2	4.	4.	GRW	155.60
145080	2	4.5	4.5	GRW	159.47
145081	2	5.	5.	GRW	157.54

Table 4.1: The ADD signal samples used in this analysis. n_{ED} is the number of extra dimensions. The M_S and M_{cut} are the ultraviolet cutoff scale and the cut value in the MC production, respectively.

with the Hewett- and GRW formalism to have signal events with constructive (GRW) and destructive (Hewett) interference.

The background samples are produced with PYTHIA [65], and shown in table 4.2. Only events where the two photons have a $E_T > 15$ GeV are selected at generator level. In the table, the symbol $\gamma\gamma_{15}$ is used to denote this generator-level requirement. The $\gamma\gamma$ samples are reweighted to match the NLO prediction from DIPHOX [66] for the irreducible background. DIPHOX is a MC computer program of partonic event generator which is used to calculate cross section of photon pair production in hadronic collisions, based on a perturbative QCD calculation of full NLO accuracy. The tool handles NLO calculation of all the processes except the box diagram, including the fragmentation into a leading photon of one or two final-state partons.

Moreover, for the reason that MC does not perfectly simulate data and that there are uncertainties in the process of energy reconstruction in the detector, some corrections need to be applied to either MC or data samples during the analysis.

Name	cross section (fb)	Dataset Number
$\gamma\gamma_{15}$	114.5 $\times 10^3$	105964
$\gamma\gamma_{15}(m > 200GeV)$	1394	119584
$\gamma\gamma_{15}(m > 800GeV)$	8.72	145606
$\gamma\gamma_{15}(m > 1500GeV)$	0.33	145607

Table 4.2: MC samples used for background studies.

These correction will be discussed in the following.

Pileup correction

The large instantaneous luminosity at the LHC leads to many *pp* scatterings taking place simultaneously in a given bunch crossing. The term "pileup" comes in this context to express the pollution due to many soft scatterings on top of an interesting hard process in a recorded event. The additional *pp* interactions, which occur at the same or previous bunch crossings, produce particles overlapping with the ones from the main interaction triggering the event. This refers to as in-time and out-of-time pileup, respectively. The pileup condition simulated in our MC samples are only a best-guess of the pileup condition in data. It is necessary at the analysis level to reweight the MC simulation pileup conditions to what is found in data. With an unprecedented instantaneous luminosity of about 10^{34} $cm^{-2}s^{-1}$, there are of the order of 20 interactions for each bunch crossing. The number of reconstructed vertices, which is indicative of the true in-time pileup, is often used to reweight MC simulation to data. That is, in most cases, sufficient for pileup consideration. However, as of 2011 data taking, the LHC is running with bunch train separation of 50 ns. Now the out-of-time pileup (overlapping signals in the detector from other neighboring bunch crossings) is also very important and the number of vertices in a given event is not a good measure anymore. Instead, one needs to use the average number of pileup interactions $< \mu >$ [67]. A Pileup Reweight Tool has been created to calculate the event weight to apply for Monte Carlo events in order to reweight that Monte Carlo sample to a given data sample [67]. We have used this tool as a consideration of pileup correction in our analysis.

Identification correction

The standard ATLAS sliding window algorithm for finding photons in the calorimeter and the standard identification criteria which were described in chapter 3 are used in this analysis. As discussed above, the shower shape variables in the first and second samplings of EM calorimeter are used as discriminating variables for photon identification. However, MC samples do not perfectly simulate our detector, particularly the simulation of the electromagnetic shower lateral development. It results in a non-negligible discrepancy on shower shape distributions between data and MC simulation. A Fudge Factor taking into account this systematic problem is provided [68] and applied on MC s in order to shift the shower shape distributions of MC to that of data. The validity of the fudging method has been checked by data driven measurements of the identification efficiency [69]. This leads to a systematic uncertainty in the efficiency measurement, discussed in detail in section 4.5.

Energy correction

In addition, another effect due to the imperfection of calorimeter simulation also needs to be taken into account. It concerns the energy measurement, and a tool called EnergyRescaler has been introduced and is responsible for energy correction on EM objects applied seperately in data and MC. The tool provides the energy scale correction to data which is obtained from the study of resonances such as $Z \rightarrow ee$, $J/\psi \rightarrow ee$ by constraining the di-electron invariant mass distribution to the well-known Z or J/ψ lineshape. The correction simply rescales the energy of an electron or cluster in a certain η/ϕ bin by applying energy scales α using the formula $E_{corr} = E/(1+\alpha)$. On the other hand, the MC energy resolution is always observed better than the resolution in data. A smearing correction also provided by the tool is applied to MC photon energies to match the resolution seen in data.

Isolation correction

Photon isolation energy was discussed carefully in chapter 3. In this analysis we use the definition based on cell energies. It is, for a reminder, defined as the sum of calorimeter cell energies inside a cone of $\Delta R = 0.4$ around the cluster barycenter,

excluding a 5×7 grid of cells in the center of the cone. Two effects which modify this value are: the leakage of photon energy outside its center core resulting in the growth of isolation energy as a function of p_T, and the soft energy deposits in the cone due to pileup interactions. The latter becomes a more important effect with the increase of high luminosity achieved in LHC. We use an estimate of isolation energy which is corrected for these two effects [70] in both data and MC. In addition, we also correct the residual data/MC discrepancies in the p_T leakage modeling.

4.2 Event selection

This section lists the criteria which are used to select events for the diphoton analysis:

- Events are initially filtered with trigger requirement of 2g20_loose, which is designed to select events in which two photons with transverse momentum of at least 20 GeV are produced and pass the Loose identification at the trigger level.

- The GRL requirement is applied and then primary vertex selection is made. Specifically, events are selected if they are in the good luminosity blocks marked for physics analysis. Events are required to have at least one primary vertex (PV) which has at least three tracks.

- A preselection is defined as events having at least two photons with transverse energy of above 25 GeV and passing Loose identification at the reconstruction step. The two photons are imperatively located in the region of EM calorimeter which is instrumented for precision physics and outside of the transition region between the barrel and endcap calorimeter: $|\eta| < 1.37$ or $1.52 < |\eta| < 2.37$, where η is measured in the second layer of the EM calorimeter. The preselection also includes object quality and photon cleaning requirements according to the recommendations of Ref. [71].

- A tight identification on two highest-E_T photons is further required.

- Isolation energy of two highest-E_T photons is required to be below a threshold of 5 GeV.

- Additionally, events are removed if the LAr event flag is set, indicating the presence of a noise burst in the LAr calorimeter.
- Moreover, in order to make the diphoton analysis orthogonal to the dilepton analysis [72], we remove all events that are also selected as $G \to ee$ candidates in the dilepton analysis.

Table 4.3 presents the data cut flow for the various selection cuts. A total of 135,196 data events pass all selection requirements.

Selection Cut	Data Events
1. Trigger Requirement	6,459,127
2. GRL and Primary Vertex Requirements	6,121,534
3. Preselection	1,232,444
4. Tight Photon Identification	222,544
5. Photon Isolation	141,277
6. LAr Error Flag	140,889
7. *ee* Overlap Removal	135,196

Table 4.3: Number of data events surviving the various stages of the selection requirements.

4.3 Signal event study

With ADD signal samples, we firstly show in figure 4.1 the η and p_T distributions of leading and subleading photons as well as the $m_{\gamma\gamma}$ distribution at truth level for various GRW samples. It can be clearly seen that the η distribution of signal photons is very broad, while the Atlas detector acceptance for high precision measurement is limited to $|\eta| < 2.5$. This leads to a significant loss of acceptance in ADD signals as can be seen in table 4.4. This table shows the acceptance and efficiency after various steps of selection. The signal acceptance "truth A" is understood as a requirement of the

two signal photons pass the p_T and η cuts at the truth level. For the GRW formalism the signal acceptance is varying from 20% to 12%. This variation is a consequence of the variation of the η distributions of the leading and subleading photons, as seen in figure 4.1. The signal offline efficiency is defined as the percentage of events within the acceptance which are selected after all selection cuts. This efficiency, which includes identification and isolation efficiency of the two photons, is roughly constant at the level of 65-68%. The final column of table 4.4 shows the product of the acceptance and efficiency multiplied by the fraction of surviving events which are in the ADD search region (which we will discuss in detail later), namely with diphoton mass greater than 1217 GeV. This choice of mass cut comes from the optimization of the expected limit described in section 5.3. More information about the systematic uncertainties on the event selection efficiency appears in the following section. The selection efficiency decreases as a function of M_S that can be seen obviously in GRW samples but not in Hewett samples due to the fluctuation of small statistics.

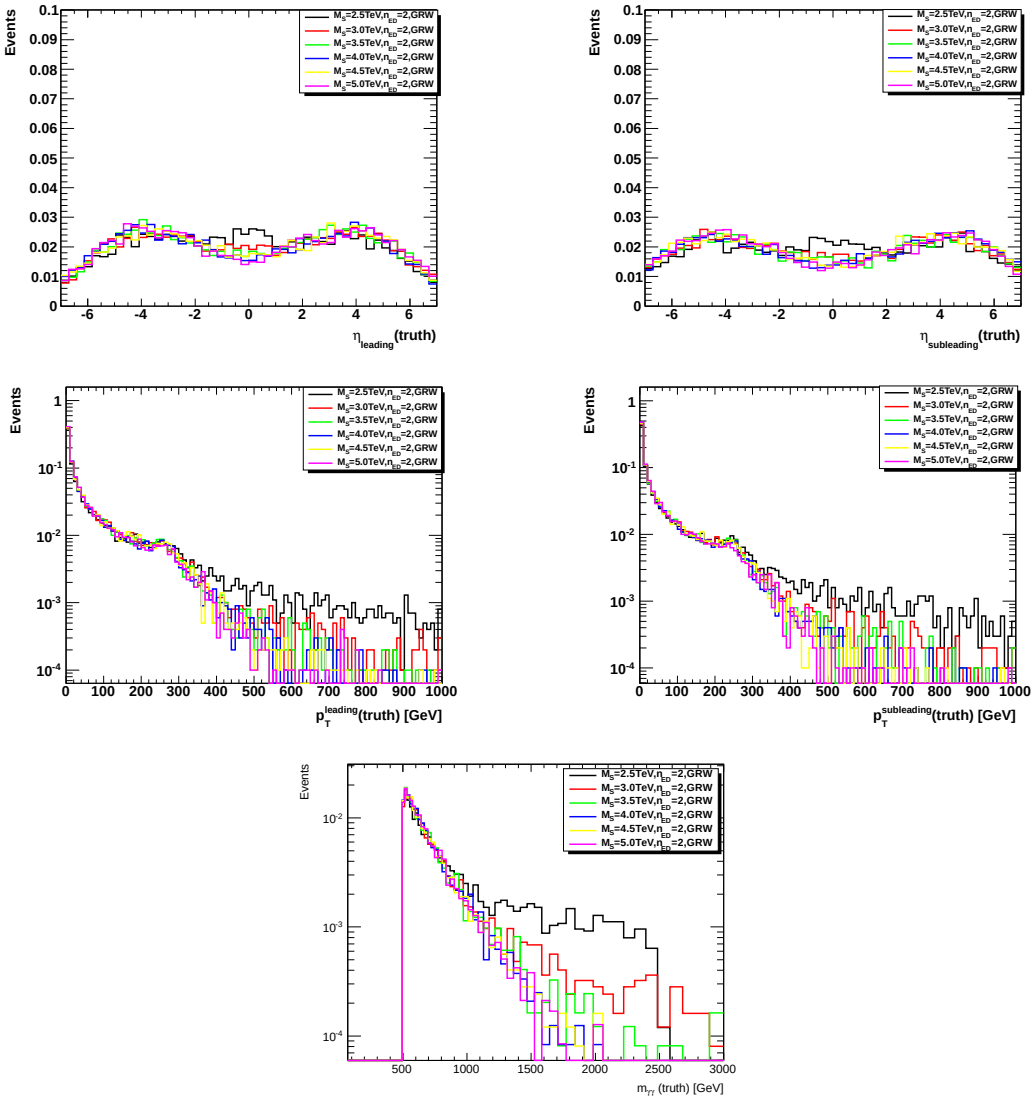

Figure 4.1: Truth-level η and p_T distributions for the leading and subleading photon, and $M_{\gamma\gamma}$ in the ADD model for the GRW MC signal samples. The mass shape is cut at 500 GeV due to the mass selection at generator level.

MCID	M_S(TeV)	KK	truth A	offline ϵ	$M_{\gamma\gamma} > 1.217\ TeV$	$A \times \epsilon \times M_{\gamma\gamma}$ cut
145068	2.5	Hewett	$(13.12 \pm 0.34)\%$	$(68.30 \pm 1.28)\%$	$(8.71 \pm 0.94)\%$	$(0.78 \pm 0.09)\%$
145069	3.	Hewett	$(13.39 \pm 0.34)\%$	$(65.99 \pm 1.29)\%$	$(2.61 \pm 0.53)\%$	$(0.23 \pm 0.05)\%$
145070	3.5	Hewett	$(12.72 \pm 0.33)\%$	$(63.89 \pm 1.35)\%$	$(1.33 \pm 0.40)\%$	$(0.11 \pm 0.03)\%$
145071	4.	Hewett	$(12.89 \pm 0.34)\%$	$(68.34 \pm 1.30)\%$	$(1.69 \pm 0.43)\%$	$(0.15 \pm 0.04)\%$
145072	4.5	Hewett	$(13.22 \pm 0.34)\%$	$(65.59 \pm 1.31)\%$	$(0.89 \pm 0.31)\%$	$(0.08 \pm 0.03)\%$
145073	5.	Hewett	$(12.63 \pm 0.33)\%$	$(68.18 \pm 1.31)\%$	$(2.01 \pm 0.47)\%$	$(0.17 \pm 0.04)\%$
145076	2.5	GRW	$(20.69 \pm 0.41)\%$	$(68.39 \pm 1.02)\%$	$(22.64 \pm 1.11)\%$	$(3.20 \pm 0.18)\%$
145077	3.	GRW	$(16.05 \pm 0.37)\%$	$(66.65 \pm 1.18)\%$	$(10.33 \pm 0.93)\%$	$(1.10 \pm 0.10)\%$
145078	3.5	GRW	$(14.57 \pm 0.35)\%$	$(66.06 \pm 1.24)\%$	$(5.61 \pm 0.74)\%$	$(0.54 \pm 0.07)\%$
145079	4.	GRW	$(14.17 \pm 0.35)\%$	$(68.88 \pm 1.23)\%$	$(2.29 \pm 0.48)\%$	$(0.22 \pm 0.05)\%$
145080	4.5	GRW	$(13.95 \pm 0.35)\%$	$(66.01 \pm 1.27)\%$	$(2.40 \pm 0.50)\%$	$(0.22 \pm 0.05)\%$
145081	5.	GRW	$(12.98 \pm 0.34)\%$	$(65.00 \pm 1.32)\%$	$(2.33 \pm 0.52)\%$	$(0.20 \pm 0.04)\%$

Table 4.4: Acceptance and efficiency of different cut levels for the ADD signal MC samples listed in table 4.1. For more details, see the text.

4.4 Background study

The background in the diphoton analysis is divided into two categories. The irreducible background is due to SM processes emitting a pair of real isolated photons in final state. These events necessarily pass our diphoton event selection, but they are due to SM processes and not a graviton. It contributes significantly to the total background, including in the signal region, the high end of the diphoton invariant mass spectrum. The second contribution is called the reducible background. It is due to QCD processes (dijets, photon+jets), in which another physical object, typically a jet, is misidentified as photon during reconstruction. It contains events in which one or both of the photon candidates results from fake objects. This type of background thus appears from the imperfection of experimental setup conditions. The word "reducible" implies that tighter photon identification requirements tend to reduce the contamination from this background. We are indeed using rather tight selection requirements to reduce this kind of background. However, this does not mean that we can definitely ignore it. In proton-proton collider experiments, due to an overwhelmingly large cross section of QCD processes, and also to the impact of pileup activity appearing in high luminosity collisions, the possibility of fake photon recognition can not be neglected although we do have a very good injection of fake photons. As a consequence, both two kinds of backgrounds are essentially studied in detail in the following section.

4.4.1 Irreducible background

The irreducible background includes all processes with two prompt photons in the final state. Prompt photons are considered as photons produced either directly in the hard scattering or in fragmentation processes. As discussed in section 1.6, it is classified into three categories: first is both two direct photons, second is one direct photon plus one resulting from fragmentation of a quark or gluon, and third is both two photons from fragmentation. We use DIPHOX to account for NLO correction in calculation, all processes which were shown in section 1.6 are included in DIPHOX [38].

The contribution of irreducible background which is generated by PYTHIA mainly comes from direct diphoton production of LO Born process and gluon fusion. Since

these are the tree-level LO contributions, a comparison of the PYTHIA and DIPHOX predictions for the differential (in $m_{\gamma\gamma}$) cross section has been made in order to obtain a "k-factor" correction which is defined as ratio between LO and NLO cross sections. The result yields a mass-dependent effective NLO correction, shown in figure 4.2, which is used to reweight the PYTHIA MC events as a function of diphoton mass to match the DIPHOX NLO prediction. We also studied the impact on the differential cross section of several choices of parton density functions (PDFs) (MSTW2008NLO, CTEQ6.6, MRST2007LOMOD) and isolation cuts (5 - 15 GeV). Results are summarized in figure 4.3. On the left the distributions are normalized to the same value in the region below 400 GeV. This is done to mimic the effect of the normalization to data in the low mass control region as discussed in section 4.4.2. The right distributions show the relative systematic uncertainties on the shape of the irreducible background from various sources of uncertainty. These relative uncertainties are obtained by comparing the various predictions against the default configuration (MSTW2008NLO, Isolation cut at 7 GeV [2]) after normalization to data in the low-mass control region. Each uncertainty component is parametrized separately and added in quadrature to determine the final systematic uncertainty in the irreducible background.

4.4.2 Reducible background

The reducible background, also known as QCD background, contributes to diphoton production mainly by the misidentification of jets as photons. We divide it into three components: events with a leading photon and a jet misreconstructed as subleading photon, events with a leading fake photon and a subleading real photon, and lastly events in which both photon candidates result from misidentified jets. The shape of the diphoton invariant mass spectrum of the reducible background components is determined by several data driven control samples which are taken from data and enriched in one given background contribution.

- The first control sample, namely Tight-AntiTight, contains events where the leading photon candidate passes the Tight photon identification requirement. However, the second photon candidate is required to fail the Tight photon

[2]The 7 GeV is employed at the DIPHOX generator level, which corresponds to the default 5 GeV at the reconstruction level.

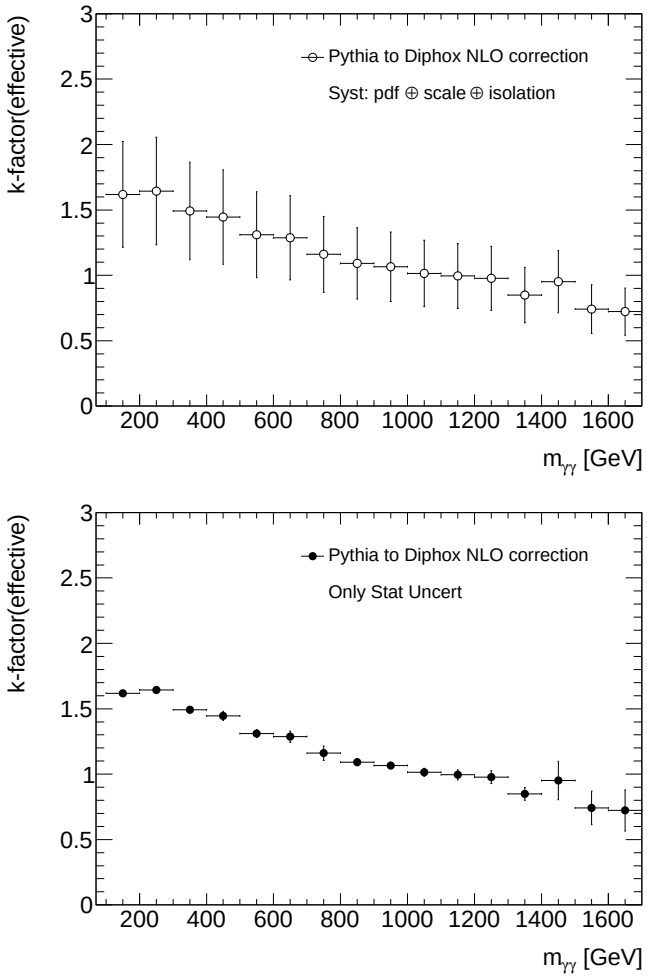

Figure 4.2: "k-factor" correction applied to PYTHIA diphoton events in order to re-weight them, at MC truth level, to the DIPHOX prediction for the differential cross section as a function of diphoton mass. (Top) the error bars show the systematic uncertainty (both normalization and shape), due to scale, isolation and PDF choices. (Bottom) the error bars show the statistical uncertainty arising from limited statistics in the Monte Carlo samples.

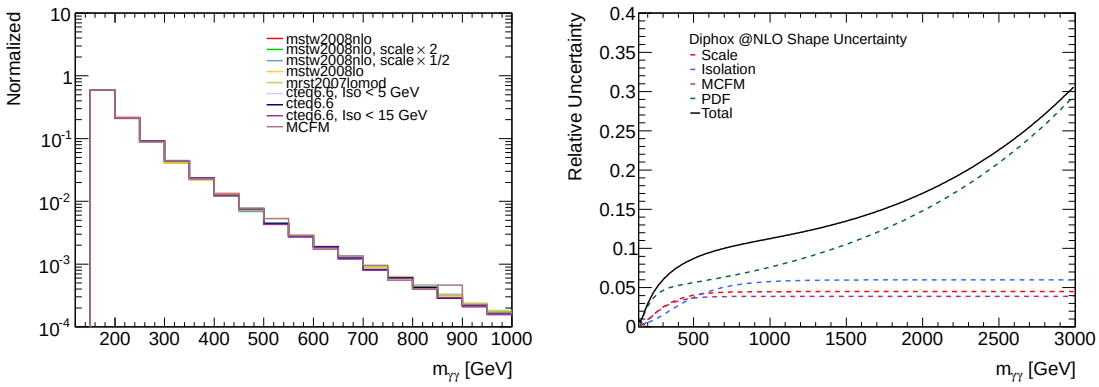

Figure 4.3: (left) Differential cross section from DIPHOX as a function of the diphoton mass for several choices of PDFs and isolation cuts. (right) Relative systematic uncertainties from various predictions as a function of the diphoton mass after normalization to data in the low-mass control region.

identification, and to pass the Loose requirement. The latter restriction is applied since the trigger selection has already required two Loose photons. This sample is enriched in $\gamma + jets$ events, where the photon passes Tight and a jet passes Loose.

- The second control sample, namely AntiTight-Tight, contains events where leading photon candidate is required to fail the Tight requirement whereas the second photon candidate passes the Tight requirement. This sample is consequently dominated by $jets + \gamma$ events.

- A third control sample, namely AntiTight-AntiTight, is defined in a similar way, but two photon candidates are selected to pass Loose and fail Tight criteria. As a result, this sample is expected to largely due to jet - jet events.

In all control samples, the two photon candidates are required to pass the same isolation cut as for the signal selection, because removing the isolation requirement was seen to bias the diphoton mass spectrum.

Figure 4.4 shows the diphoton invariant mass distributions obtained from these control samples superimposed with the result of a fit to a power law function ($x^{k_1+k_2\log(x)}$). Table 4.5 shows the results of the fit.

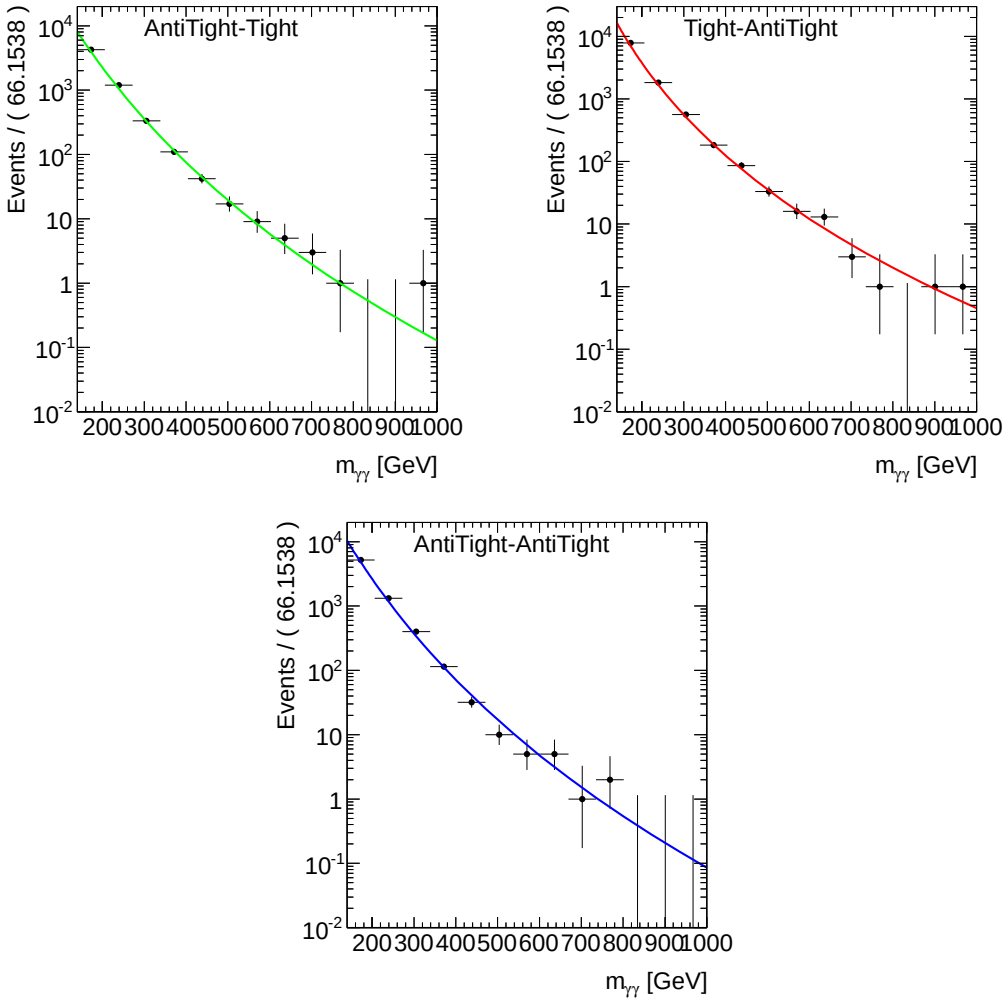

Figure 4.4: Diphoton invariant mass distributions for the three background control samples superimposed with fits to a power law function (see in the text).

Sample	Functional form	Fit parameter	Fit value	χ^2/ndf of fit
AntiTight-Tight	Power law	k1	9.5 ± 0.05	0.80
		k2	-1.28 ± 0.005	
Tight-AntiTight	Power law	k1	3.6 ± 0.04	0.43
		k2	-0.75 ± 0.004	
AntiTight-AntiTight	Power law	k1	9.7 ± 0.05	1.54
		k2	-0.95 ± 0.004	

Table 4.5: Fit results for the three control samples which we use to describe the reducible background.

4.4.3 Determination of the background composition

This section concerns in the determination of the purity. The purity is defined as the ratio of events with two real photon candidates over the total number of events in data samples in a given mass region. We determine the purity in the mass range 140-400 GeV where the presence of any graviton signal has been ruled out by previous searches. A measurement of the purity thus provides an estimate of the relative contributions of reducible and irreducible backgrounds to this low-mass control region. The lower mass threshold at 140 GeV is chosen to avoid complications due to small contamination near 90 GeV from $Z \to ee$ events with electrons faking photons.

In a previous study [73], several complementary methods for determining this purity are discussed:

- One method simply uses the DIPHOX prediction of the cross section to normalize the irreducible background contribution to data.
- The second method is to fit the diphoton mass spectrum of data and background in a low mass control region. The background spectrum is the sum of irreducible and reducible contributions with a floating purity fraction which is considered as a parameter to be fit to the data.
- The last one is known as the isolation template fit method which is also used in this analysis. It determines the background components by an extended maximum likelihood fit to the two-dimensional (2D) isolation distribution of

the two photon candidates. The details of this method will be described in the next paragraphs. This method has been developed for the purpose of the Standard Model diphoton cross section measurement [74] and it is also used in the Higgs to two photons analysis [75].

The purity results obtained from three separate methods had been found to be in good agreement with each other [73]. The method with DIPHOX prediction gives the largest uncertainty mainly due to the theoretical uncertainties. The fit to the mass spectrum also results in a relatively large uncertainty on the purity for the reason of similarity of the shapes of the irreducible and reducible background components. It implies that the total background prediction is quite insensitive to the exact value of the purity. The isolation template fit provides the best precision on the purity. This is the reason why this method is retained in current analysis.

The final goal is to normalize the total background to match the number of data events in the low-mass control region. The isolation template fit method aims to determine the contribution of four different background components, one for the irreducible background and three categories for the reducible background. It performs an extended maximum likelihood fit to the 2D isolation distribution of the Tight diphoton events, using the probability density functions (pdf) for true and fake photons derived from data control samples. The total 2D pdf of the Tight diphoton sample is written as follows:

$$\begin{aligned} P(E_{T,1}^{iso}, E_{T,2}^{iso}) \quad = \quad & N_{\gamma\gamma} P(E_{T,1}^{iso}) P(E_{T,2}^{iso}) + N_{\gamma j} P(E_{T,1}^{iso}) J(E_{T,2}^{iso}) \\ & + N_{j\gamma} J(E_{T,1}^{iso}) P(E_{T,2}^{iso}) + N_{jj} J(E_{T,1}^{iso}, E_{T,2}^{iso}) \end{aligned} \tag{4.1}$$

where $E_{T,i}^{iso}$ is the calorimeter isolation variable for the leading (i=1) or subleading (i=2) photon candidate. $P(E_{T,i}^{iso})$ and $J(E_{T,i}^{iso})$ are the isolation pdfs for true photons and fake photons, while $J(E_{T,1}^{iso}, E_{T,2}^{iso})$ is the global pdf for dijet background. The reason for which the pdf of $jet - jet$ events is not factorized as the product of the leading and sub-leading candidate pdfs is that the correlation of two fake candidates isolation variables has been shown to be non-negligible (around 20%) in [74]. The coefficients $N_{\gamma\gamma}, N_{\gamma j}, N_{j\gamma}, N_{jj}$ of the four 2D probability density functions (also called templates) are called as the yields of the different components in the total diphoton event samples. The 2D fit is performed to the sample of diphoton candidates passing

Tight identification criteria but without any isolation requirement. It directly returns the central values and statistical uncertainties of these four yields.

The determination of the pdfs starts with a control sample where two selected photons are required to pass a Loose identification criteria. The fake photon templates $J(E_{T,i}^{iso})$ are extracted from this sample with an additional requirement that photon candidate i fails the Tight criteria. The pdfs are smoothed by fitting Novosibirsk functions to the isolation distributions, and the results of the fit are shown in Figure 4.5.

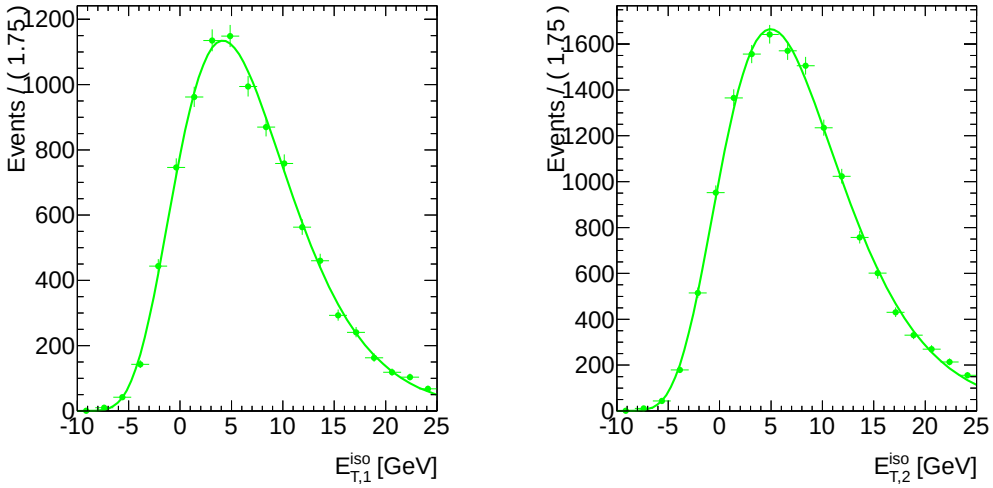

Figure 4.5: Fake pdfs $J(E_{T,i}^{iso})$ fitted on the anti-Tight sample for the leading (left) and sub-leading (right) photon candidate.

The true photon templates $P(E_{T,i}^{iso})$ are consecutively obtained by subtracting the normalized isolation distribution for fake photons from the distribution of photons from the Tight-Tight sample. The normalization of fake template is performed in a way such that it describes the distribution for $E_{T,i}^{iso}$ values greater than 10 GeV where the fakes are known to dominate. The $P(E_{T,i}^{iso})$, which is described by a Crystal Ball function, is then determined and shown in figure 4.6.

Finally, a 2D pdf of $jet - jet$ events $J(E_{T,1}^{iso}, E_{T,2}^{iso})$ is extracted by building a `RooKeysPdf` [3] based on the 2D isolation histogram of the control sample where both

[3] `RooKeysPdf`, which is a standard implementation of a kernel estimation technique [76], is used

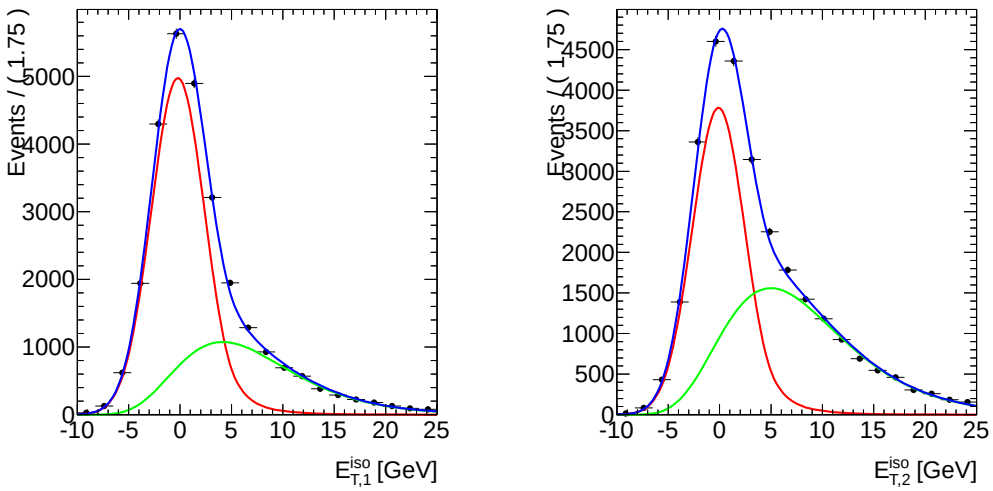

Figure 4.6: Extraction of the true photon pdfs (red) for the leading (left) and subleading (right) photon candidate. The green curves show the fixed fake pdfs that have been determined previously.

candidates fail the Tight criteria. The result is shown in figure 4.7.

Once the individual pdfs have been determined, a sum to the 2D pdf described in equation 4.1 is performed. This 2D template is later used to fit the 2D isolation distribution of the selected Tight-Tight sample. The results are displayed in figure 4.8. The different background components can be determined by integrating the corresponding pdf up to the 5 GeV isolation cut. This allows us to calculate the fractions of individual background contributions, or arbitrarily the purity, in the final selection of the analysis, as shown in table 4.6.

Systematic uncertainty in background estimation

The systematic uncertainty of this method is mainly due to the impact of correlation between identification and isolation of photons. Particularly, the contamination of true photons in jet templates is varied depending on the chosen of Loose identification criteria, since Loose photon sample refers to jet definition. The more stringent of Loose sample we define, the less reference to jets we get. A Loose criterion can be

in `RooFit` toolkit [77] to build a pdf estimation from an arbitrary input dataset as a superposition of Gaussian kernels.

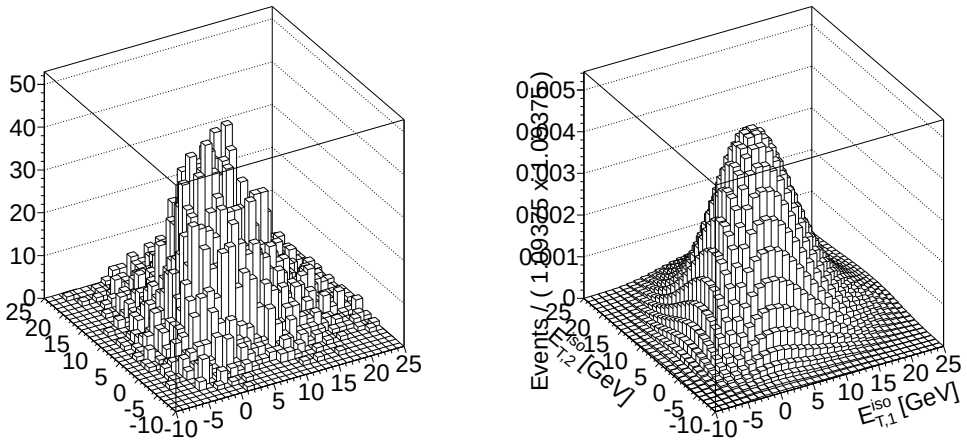

Figure 4.7: Histogram of dijet events (events where both photons fail Tight) is shown on the left, while a smoothed `RooKeyPdf` derived from the histogram is shown on the right.

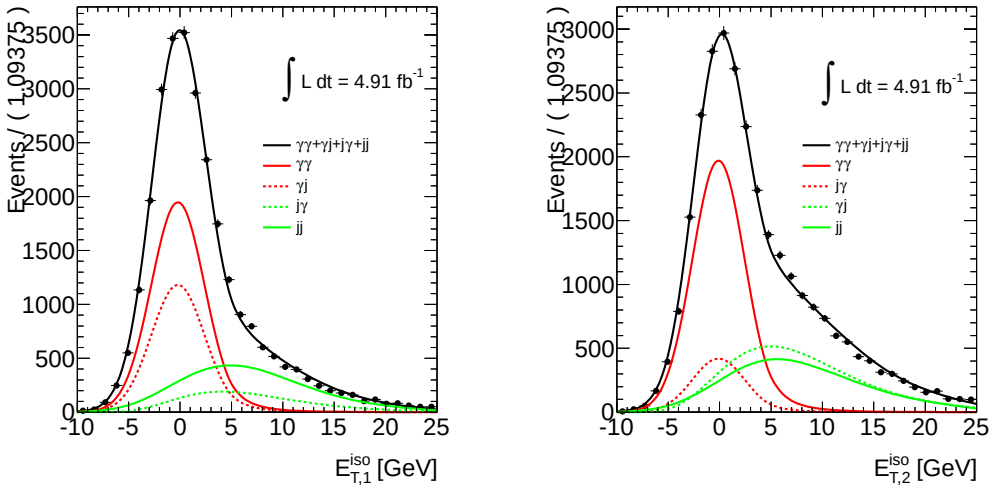

Figure 4.8: Projections of the 2D fit of the Tight-Tight sample on the first (left) and second (right) photon isolation variable.

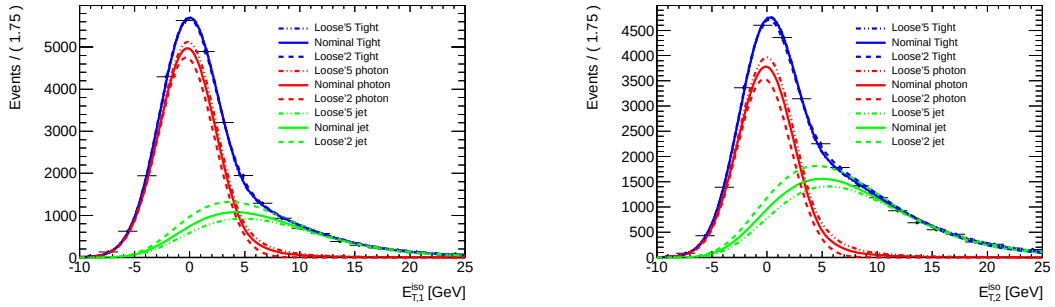

Figure 4.9: Impact of the Loose' variation on the true photon pdfs (red) and true jet pdfs (green) for the leading (left) and sub-leading (right) photon candidate.

understood by relaxing several cuts with respect to the Tight criterion, for the purpose of reducing as much as possible correlations with the isolation variable. We define some different Loose' samples with a variation on relaxed cut list in order to assess the systematic uncertainty on purity estimation with this 2D template fit method. By varying the Loose' sample definition, it induces large variation of the jet templates and consequently of the photon templates, as illustrated in Figure 4.9. For each Loose' configuration, we performed the extraction of the yields as illustrated in Figure 4.10. Table 4.6 shows the fit results of this method. The event yields for signal and for each of the background components are listed for four different Loose' samples. It is noticed that these numbers are derived in the low invariant mass control region, the photon event purity (as defined in table 4.6) can be considered as the fraction of irreducible background contribution over the total background in this control region.

4.4.4 Extrapolation of background prediction to the signal region

We have determined both the shape and the normalization of two kinds of background components in the low mass control region. The following step is to extrapolate the background prediction to the signal region of higher diphoton mass values.

For the irreducible background, we have generated PYTHIA samples with good statistics over the entire range of interest, up to about 3 TeV. Moreover, with DIPHOX

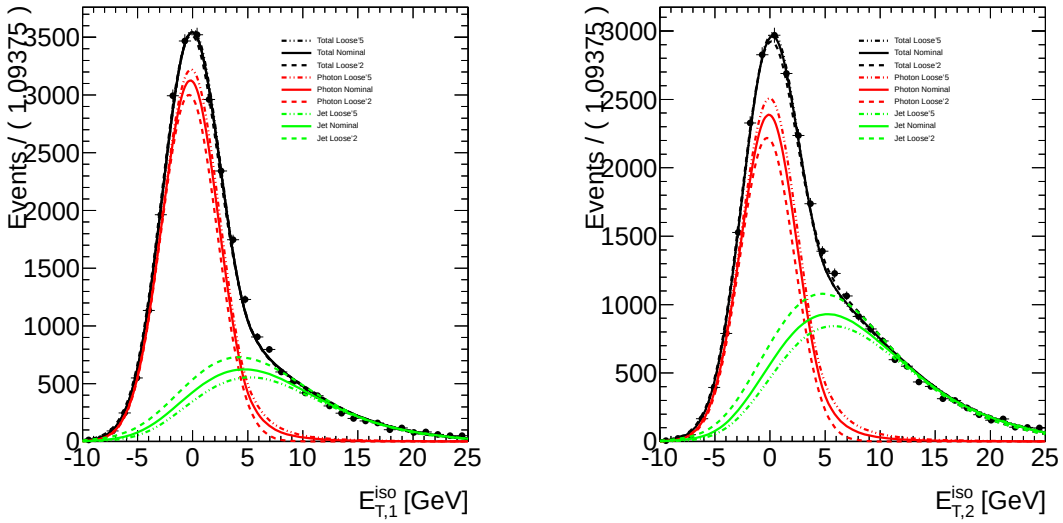

Figure 4.10: Impact of the Loose' variation on the 2D fit of the Tight-Tight sample on the first (left) and second (right) photon isolation variable.

corrections, we have obtained the shape at NLO approximation which is simply extrapolated to high mass region. It is noticed that DIPHOX has a correction up to 1.3 TeV, above this region no correction is applied so far. All details, as well as the mass dependent systematic uncertainty on the shapes were discussed in section 4.4.1.

For the reducible background, since it has been derived from data and depends on the different choices of Loose' control samples. We have to study possible variations on the extrapolated mass shapes with different Loose' control samples in order to assess the systematic uncertainties of the reducible background shape. The change of several Loose' definitions is as used in 4.4.2. This check aims to estimate the impact of the correlation between the identification and the diphoton invariant mass.

To estimate the total background prediction, the irreducible and reducible background components are added together with appropriate weights accounting for the central value of the 2D template fit results. A systematic uncertainty from the yield determination therefore needs to be considered in addition to the shape uncertainty. This uncertainty is achieved by comparing the total background predictions of different yield estimations from different Loose' definition. Figure 4.11 shows the results as a function of invariant mass. It indicates from the right plot of figure 4.11 that the

Loose' sample	$N_{\gamma\gamma}$	$N_{\gamma j}$	$N_{j\gamma}$	N_{jj}	Purity = $\frac{N_{\gamma\gamma}}{N_{tot}}$ (%)
Loose' 2 (2 cuts relaxed)	9646±136	3086±58	1222±50	1707±32	61.6±0.5
Loose' 3 (3 cuts relaxed)	10120±139	2986±56	1207±49	1379±28	64.5±0.5
Loose' 4 (nominal) (4 cuts relaxed)	10812±138	2640±51	1057±44	1167±24	69.0±0.5
Loose' 5 (5 cuts relaxed)	11647±137	2265±45	886±37	890±20	74.2±0.4

Table 4.6: Results, including systematic uncertainties, of the 2D template fit method. The nominal Loose' sample corresponds to 4 Tight cuts relaxed. The maximum deviations observed among the different samples, as compared to the nominal cuts, are taken as the systematic uncertainty.

uncertainty due to the yield estimation grows up to 10 % at high mass.

Finally the total systematic uncertainty of backgrounds is calculated as the sum in quadrature of three different sources: the uncertainty on the shape of irreducible and reducible background distributions separately, plus the uncertainty due to the yield estimations of background components resulted from the template fit method. All is presented in figure 4.12.

4.5 Systematic uncertainties on signal

We describe in this section several sources which result in systematic uncertainties on signal efficiency determination. They include the effects of pileup, photon identification or isolation. Some minor effects from the luminosity measurement or the bunch crossing identification, etc. are also taken into account.

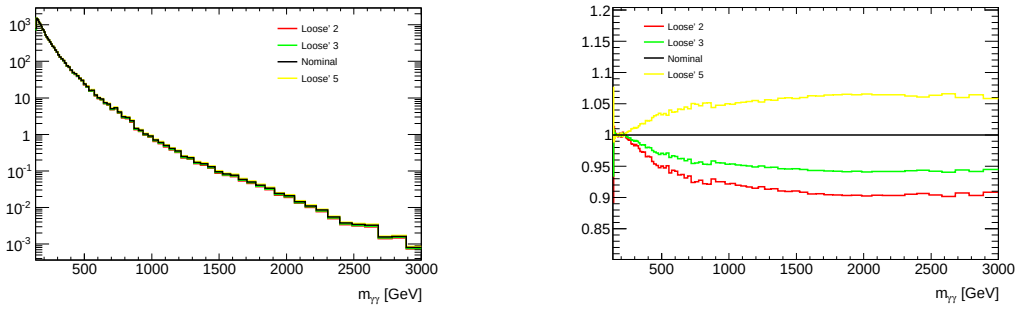

Figure 4.11: Comparison of the total background estimation with yield estimation using different Loose' samples w.r.t. to the nominal yield estimation.

4.5.1 Pileup uncertainty

Due to the high luminosity of Atlas data collected in 2011, it is necessary to study the impact of pileup effect on the signal efficiency. We have, during the data collection, different pileup conditions depending on the data taking periods. This refers to a wide distribution of the average number of interaction per bunch crossing $< \mu >$, as shown in figure 4.13 on the left. By considering the variation of efficiency as a function of $< \mu >$, we can estimate the systematic uncertainty due to pileup. A linear fit is applied to the efficiency plot as a function of $< \mu >$ to provide the best estimate of variation. The systematic uncertainty is determined as a variation of efficiency within one sigma variation of $< \mu >$. We conclude that the pileup impact on signal efficiency for our study with these pileup conditions can be negligible since the variation is less than 1 % which is displayed in figure 4.13 on the right.

4.5.2 Identification uncertainty

In order to assess the systematic uncertainty due to photon identification, a comparison on photon efficiency is performed between results from MC simulation and those from data driven measurement. Several independent data driven approaches have been studied to reach the efficiency estimations in different regions of photon pseudorapidity and transverse momentum for both converted and unconverted candidates [78, 79, 80]. These give consistent results and have a final combination in Ref. [81]. In this analysis, we decided to use the results from the data driven ma-

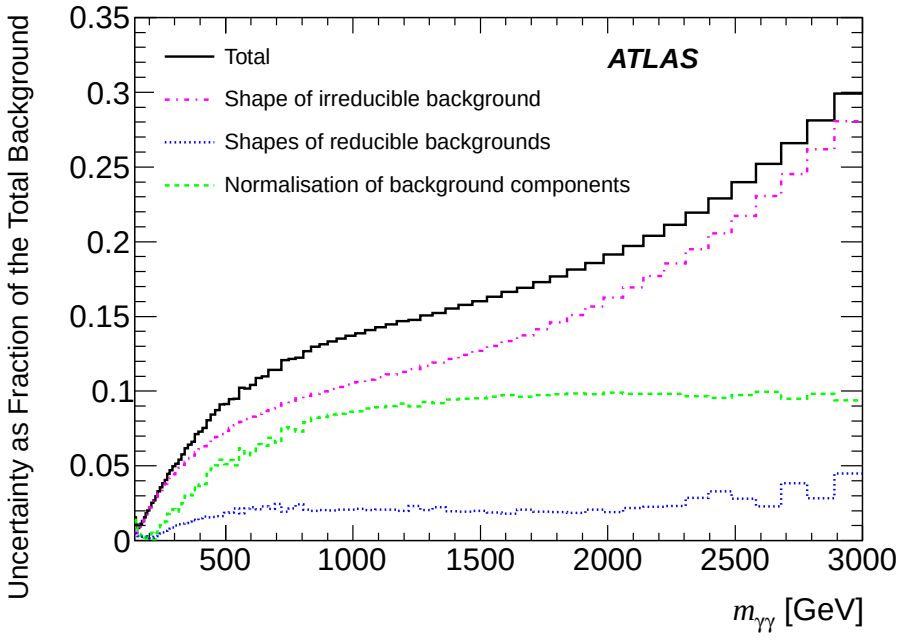

Figure 4.12: The final total systematic variations in the shape of the background prediction as a function of diphoton mass. This includes uncertainties on the reducible and irreducible background shapes and the relative yields estimation.

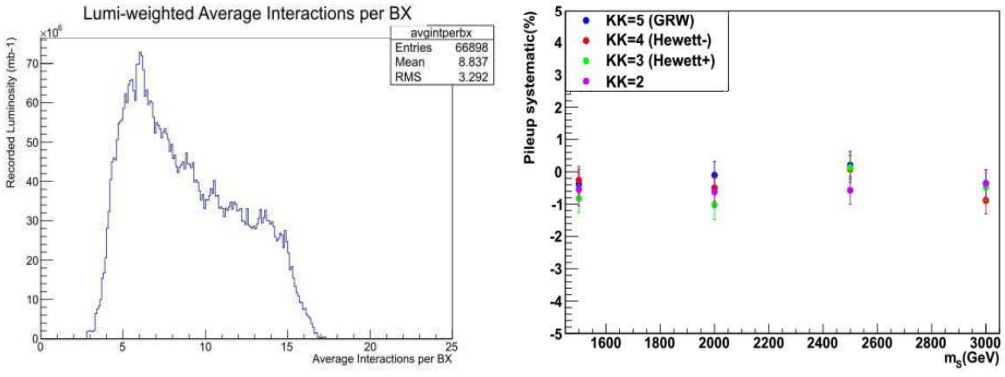

Figure 4.13: On the left, the distribution of the average number of interaction per bunch crossing for 2011 data collection. On the right, it shows the systematic uncertainty on signal efficiency determination due to pileup effect.

trix method to compare to the simulation results after applying the shower shape correction (Fudge Factor correction) [80].

However, the photon E_T spectrum for comparison in Ref. [80] is just covered to 400 GeV while our ADD signal photon E_T spreads up to approximately 1 TeV. We then quoted the uncertainty for $p_T > 400$ GeV equal to the last bin result of the matrix method measurement. This is slightly a conservative approach since the discrepancy between data and MC decreases as a function of p_T. These results simply describe the identification systematic uncertainty for one photon. We need a further combination of uncertainties to count for diphoton event production in our analysis.

We firstly determine the uncertainty of each photon separately depending on conversion mode (converted or unconverted), p_T and η of photon. By considering leading and subleading photons in the events are fully correlated, the uncertainty on events is the sum of each together. To simplify, we can demonstrate the formula to calculate the event uncertainty as the following:

$$\begin{aligned}\Delta\epsilon_{ID} \quad = \quad & [N_{CC} \times (\Delta\epsilon_{ID}^{leadconv} + \Delta\epsilon_{ID}^{subleadconv}) + \\ & N_{UC} \times (\Delta\epsilon_{ID}^{leadunconv} + \Delta\epsilon_{ID}^{subleadconv}) + \\ & N_{CU} \times (\Delta\epsilon_{ID}^{leadconv} + \Delta\epsilon_{ID}^{subleadunconv}) + \\ & N_{UU} \times (\Delta\epsilon_{ID}^{leadunconv} + \Delta\epsilon_{ID}^{subleadunconv})]/(N_{CC} + N_{UC} + N_{CU} + N_{UU})\end{aligned} \tag{4.2}$$

where the total numbers of diphoton events are classified into 4 categories: N_{CC}, N_{UC}, N_{CU}, N_{UU} which are numbers of event with leading converted and subleading converted photons, leading unconverted and subleading converted photons, leading converted and subleading unconverted photons, leading unconverted and subleading unconverted photons respectively. The $\Delta\epsilon_{ID}^{leadconv}$, $\Delta\epsilon_{ID}^{leadunconv}$, $\Delta\epsilon_{ID}^{subleadconv}$, $\Delta\epsilon_{ID}^{subleadunconv}$ are the *average* systematic identification uncertainties for each kind of photon which have already considered the dependence on the p_T and η of photons. Equation 4.2 gives an average uncertainty on the event efficiency due to photon identification for a given signal sample. The relative systematic uncertainties shows in figure 4.14, give a fairly flat results, around 4.5 % for different ADD samples.

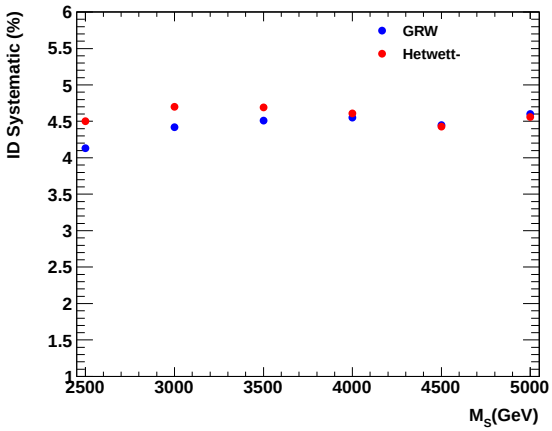

Figure 4.14: Photon identification relative systematic uncertainty on the signal efficiency.

4.5.3 Isolation uncertainty

Since the analysis requires isolated photons in the selection, we need to investigate the impact of isolation requirement on the signal efficiency. We have performed some studies on isolation efficiency with MC samples, a comparison on MC signal and background samples [82]. However, in order to determine the systematic uncertainty due to isolation, the discrepancy on photon isolation energy distributions between MC and data samples should be evaluated and discussed in detail.

The photon isolation distributions have been studied in both data and MC in the aspect of dependence on the number of primary vertex (nPV) and the p_T of photon. In order to get the distribution of true photons from data, the procedure is similar to what we had described in the 2D template fit method. For data, we start with a sample of Loose reconstructed photons (Loose sample) from which it can induce two subsets, the ones passing the Tight criteria (Tight sample) separate from the ones failing the Tight (antiTight sample). In the Tight sample, it composes of both true and fake photons. Therefore the true photon distribution can be determined by subtracting the contribution of fake photons from the total distribution of Tight sample. The fake shape can be estimated from the antiTight sample which is dominated by the fake photons, then it is normalized to agree with the Tight sample distribution in

the region of isolation value above 10 GeV since the main population in this region is known by fakes. The normalized antiTight distribution is then subtracted from the Tight sample, and the remaining distribution is fitted to a Crystal Ball (CB) function. For MC samples of pure photons, the fit is done directly on the Tight samples without a need of background subtraction. The results of this procedure are illustrated in figure 4.15 for events with $6 < \text{nPV} < 8$, and figure 4.16 showing the result for photons with p_T between 75 and 100 GeV.

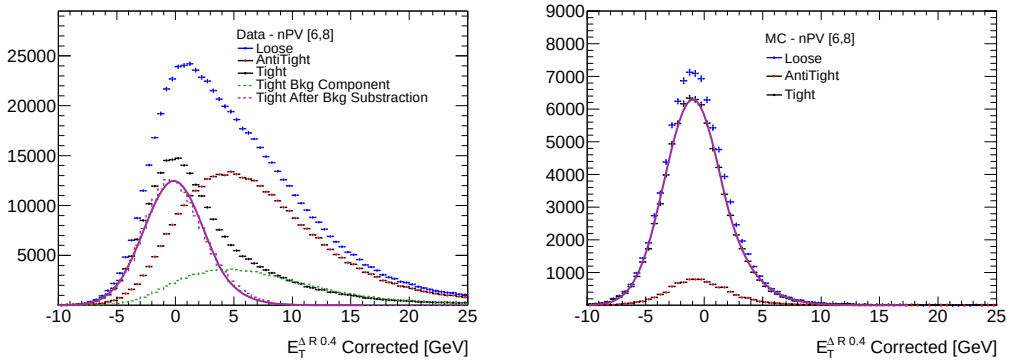

Figure 4.15: Isolation distribution for events with $6 < \text{nPV} < 8$ in (left) data (right) MC. Loose, Tight and anti-Tight samples are shown in blue, black and red markers respectively. For data, the dashed green ticks shows the normalized anti-Tight sample and the magenta dashed line shows the Tight sample after the background subtraction procedure. The magenta line shows the result of the CB fit to the latter.

The fitted CB's mean and width results of data are compare to these of MC as a function of nPV and p_T photon and are summarized in figure 4.17 and 4.18 respectively. For case of nPV dependence, we see that the mean value is rather constant in MC, while in data it is shifted to larger values as nPV increases. The width grows with nPV in both MC and data. For case of p_T dependence, it again shows no dependence of mean value on p_T of photon in MC as consequence of the correct implementation of leakage corrections. In data, there is still a shift of the mean value to higher value when p_T increases. The width is constant and similar between data and MC for this case.

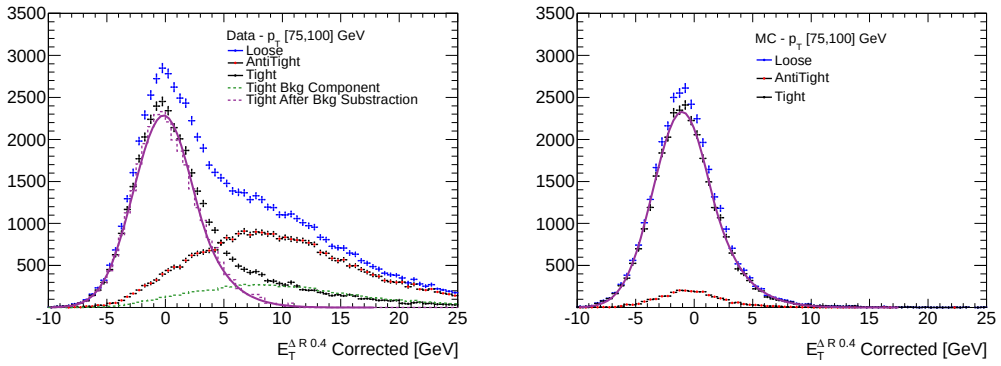

Figure 4.16: Isolation distribution for events with 75 $<p_T <$ 100 GeV in (left) data (right) MC. Loose, Tight and anti-Tight samples are shown in blue, black and red markers respectively. For data, the dashed green ticks shows the normalized anti-Tight sample and the magenta dashed line shows the Tight sample after the background subtraction procedure. The magenta line shows the result of the CB fit to the latter.

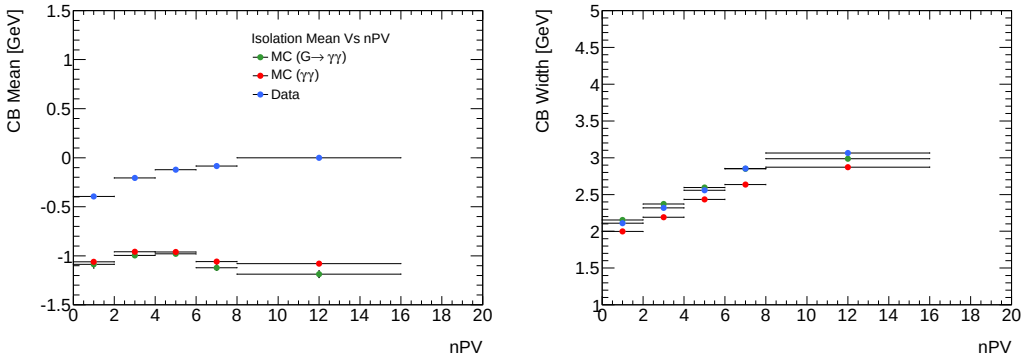

Figure 4.17: Isolation mean (left) and width (right) values coming from the CB fit for data (blue) and MC (red/green) as a function of nPV. The error bars on the x coordinate represent the interval being covered.

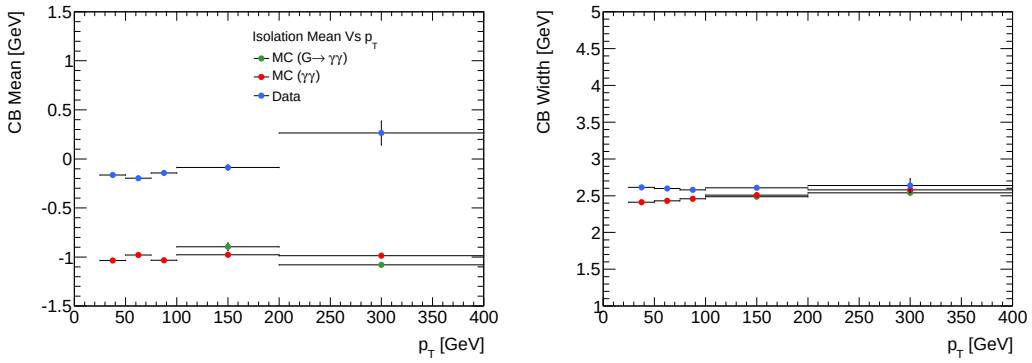

Figure 4.18: Isolation mean (left) and width (right) values coming from the CB fit for data (blue) and MC (red/green) as a function of pt. The error bars on the x coordinate represent the interval being covered.

For both two studies, the data/MC discrepancy on the mean of CB fit is about 1 GeV (data in higher values). To account for the systematic uncertainty coming from such deviations, we apply to MC samples a move from the default isolation cut value of 5 GeV to the cut of 4 GeV. Then we take the difference in efficiencies obtained by the nominal cut and the shifted one as an estimate of systematic uncertainty due to isolation. The results are shown in figure 4.19.

In summary, the combined uncertainty due to the photon identification and isolation can be obtained by adding in quadrature the two separate contribution. The result is shown in figure 4.20. We quote the value of 8% for this combination.

Besides, there are other various systematic uncertainties accounted for the signal efficiency, they are presented in table 4.7. These include the 3.9% uncertainty on the integrated luminosity [83], and a 1% uncertainty to account for the limited signal MC statistics. The bunch crossing identification uncertainty which is of 0.3% is taken from Ref. [72], where a study was made of the ability to pick the correct BCID when signal pulse saturation occurs in the trigger digitization.

4.5.4 PDF uncertainty impact on signal cross section

Each PDF has its uncertainty which comes from experimental measurement errors used to construct the PDF and from theoretical approximations. The specific choice

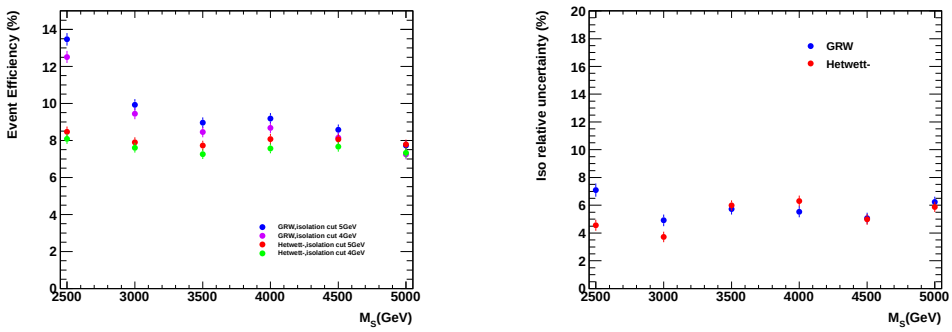

Figure 4.19: Event efficiency as a function of M_S for default isolation cut (5 GeV) and the shifted cut (4 GeV). The relative uncertainty is shown on the right.

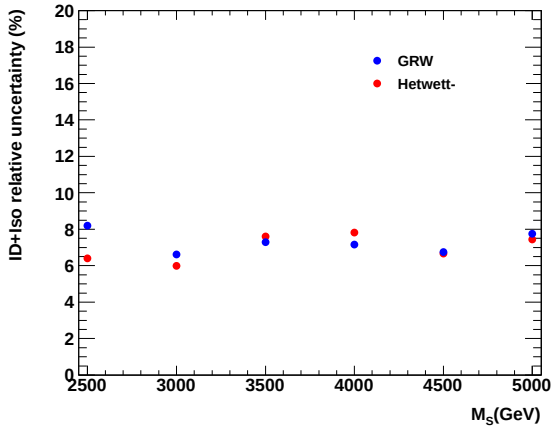

Figure 4.20: Photon isolation+identification relative systematic uncertainty on the event efficiency.

Source of Uncertainty	Signal Uncertainty (%)
Integrated Luminosity	3.9
MC Statistics	1.0
Bunch Crossing Identification	0.3
Photon Trigger	2.0
Photon ID+isolation	8.0
Total Signal Uncertainty	9.2

Table 4.7: Summary of systematic uncertainties for the signal. The total signal uncertainty is obtained by summing in quadrature all the contributions.

of PDF has an impact on the predicted signal: it affects directly the signal cross section and it modifies the shape of distributions and therefore impacts the selection efficiency. This is a kind of systematic uncertainty from theoretical prediction. We used CTEQ6.6 in this analysis.

Derived from Hessian matrix method [84] which helps to calculate the PDF uncertainty, it provides N eigenvectors as the basis of the PDF parameter space (N free parameters). Each eigenvector probes a direction in PDF parameter space. There are 2N+1 members of the PDFs where there is a central member and 2N members correspond to up and down variations of each N eigenvector direction. The central member gives a best estimate for an observable of interest, specifically the cross section. The other 2N members give positive and negative deviations around the central observable. This can result in an asymmetric uncertainty on cross section as:

$$\Delta\sigma^{+} = \sqrt{\sum_{i=1}^{n}(max(\sigma_i^{+} - \sigma_0, \sigma_i^{-} - \sigma_0, 0))^2} \tag{4.3}$$

$$\Delta\sigma^{-} = \sqrt{\sum_{i=1}^{n}(max(\sigma_0 - \sigma_i^{+}, \sigma_0 - \sigma_i^{-}, 0))^2} \tag{4.4}$$

where n is the number of PDF eigenvectors, σ_i^{+} is the cross section for the higher value of the i^{th} PDF eigenvector, σ_i^{-} is the cross section for the lower value of the i^{th} PDF eigenvector, and σ_0 is the cross section for the central member of the PDFs.

Convention	M_S	CTEQ6.6		
	(GeV)	$\sigma_0(pb)$	Uncertainty (%)	
GRW	2500	0.16696	+9.13	-4.83
GRW	3000	0.15319	+9.08	-4.81
GRW	3500	0.14945	+8.23	-6.53
GRW	4000	0.14799	+8.20	-6.09
GRW	4500	0.14651	+10.4	-4.77
GRW	5000	0.14645	+9.82	-4.94
Hewett	2500	0.14659	+8.08	-6.33
Hewett	3000	0.14434	+10.5	-4.14
Hewett	3500	0.14553	+7.83	-6.81
Hewett	4000	0.14466	+11.2	-3.52
Hewett	4500	0.14576	+8.21	-6.13
Hewett	5000	0.14572	+6.38	-8.08

Table 4.8: Cross section computed with CTEQ6.6 PDF and fractional uncertainty due to PDF variation.

The cross section and its fractional uncertainties are shown in table 4.8. These uncertainties are exposed in figure 5.2 in the number of signal event calculation. In the context of CTEQ6.6, they are expressed at 90% C.L.

4.6 Result and plot

Figure 4.21 shows the final diphoton invariant mass distribution over the full range with the background prediction superimposed. Evidently it has no observation of excess above the background for total amount of Atlas data recorded in 2011. The bottom panel of figure 4.21 shows a bin-by-bin statistical significance of the difference between data and background, where the definition of statistical significance can be found in Ref. [85]. Shortly introduction, it is the probability of finding a deviation of expected background at least as big as the one observed in data. Small value means insignificant discrepancy and inversely, larger value implies significant discrepancy

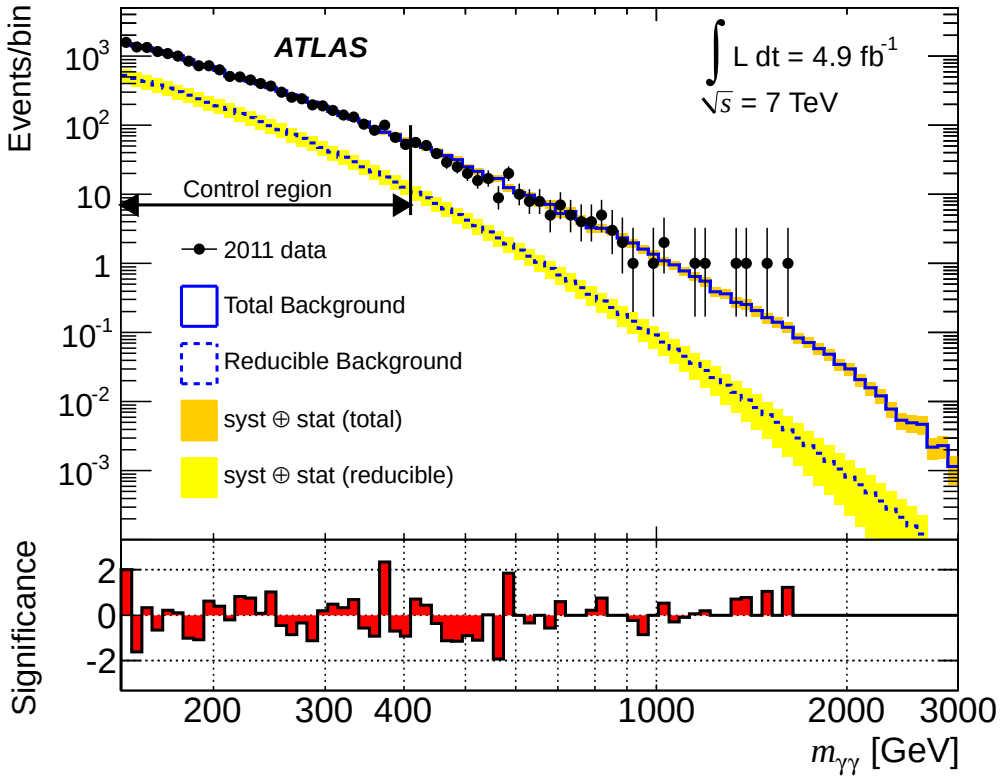

Figure 4.21: (Upper) Observed invariant mass distribution of diphoton events. Superimposed is the SM background prediction, including irreducible and reducible components. (Lower) The bin-by-bin significance of the difference between data and background is shown in the lower panel.

between data and background. Following the convention of Ref. [85] , the significance is set to zero for bins with insignificant deviations with respect to a small expected background. This concerns mainly the bins at large $m_{\gamma\gamma}$ where a fraction of an event is expected (on average) and where zero events are observed.

Besides, we also present the numbers of events in each mass bin contributed by irreducible and reducible background separately, as well as the total number of background against the actual observed number of events in data for that bin, see table 4.9. The binning was chosen to have a constant logarithmic width to compensate the quick decrease of data spectrum. The expected total number of background again insists

Mass Window	Background Expectation			Observed
$[GeV]$	Irreducible	Reducible	Total	Events
$[142, 409[$	10195 ± 1092	4586 ± 1092	14781	14781
$[409, 512[$	192 ± 26	42.6 ± 10.4	234.73 ± 19.7	221
$[512, 596[$	57.2 ± 8.1	10.7 ± 2.7	67.8 ± 6.6	62
$[596, 719[$	35.0 ± 5.1	5.4 ± 1.5	40.4 ± 4.4	38
$[719, 805[$	11.9 ± 1.8	1.4 ± 0.4	13.3 ± 1.6	13
$[805, 901[$	7.8 ± 1.2	0.7 ± 0.2	8.5 ± 1.1	10
$[901, 1008[$	4.6 ± 0.7	0.4 ± 0.1	5.0 ± 0.7	2
$[1008, 1129[$	2.7 ± 0.4	0.2 ± 0.1	2.8 ± 0.4	2
$[1129, 1217[$	1.1 ± 0.2	0.06 ± 0.03	1.2 ± 0.2	2
$[1217, 1312[$	0.72 ± 0.12	0.04 ± 0.02	0.76 ± 0.11	0
$[1312, 1414[$	0.50 ± 0.08	0.02 ± 0.01	0.53 ± 0.08	2
$[1414, 1525[$	0.36 ± 0.06	0.01 ± 0.01	0.37 ± 0.06	1
$[1525, 2889[$	0.64 ± 0.12	0.02 ± 0.01	0.66 ± 0.12	1

Table 4.9: Number of events expected from the reducible and irreducible background components as well as the total background and observed number of events in each mass bin. The uncertainty on the reducible and irreducible components take into account the uncertainty on the shape and the yields estimate. Since the yields uncertainties are strongly anticorrelated between the two components, their contribution to the total uncertainty is reduced.

the good agreement with the observed data in each mass bin.

Chapter 5

Limit setting

The common statistical analysis tasks in searching for new physics are, firstly, to look for a potential excess of candidate events by testing and quantifying the consistency of the data with the background expectation. In the absence of a significant excess, the next step is to set confidence limits on parameters of interest that describe a potential signal. The confidence intervals can be quantified by following the frequentist or the Bayesian approaches [86].

In our analysis, from the invariant mass distribution comparing data to MC, we have seen no significant excess of data above background estimation. We proceed to set an upper limit on parameters of the ADD model. Beyond the limit, data exclude the model at 95% confidence level (C.L.). The procedure is implemented in a software tool, namely the Bayesian Analysis Toolkit, which has been developed to apply Bayes' theorem in limit setting. A brief introduction of this toolkit is presented in the first section of this chapter. Next, we discuss in detail the Bayesian approach in section 5.2. A procedure from Bayesian probability to an upper limit inference will be described. In the comparison of data and MC, we can simply count and compare the number of events in a defined mass region. This approach is known as a counting experiment analysis. Or, we can consider the entire shape distributions of data and MC in that interested region. In section 5.3, we will present the results of Bayesian limit using both two approaches.

5.1 Bayesian Analysis Toolkit

The main goals of a typical data analysis are to compare model predictions with data, to draw conclusions on the validity of the model, and to extract the possible values of parameters within the context of a given model. The Bayesian Analysis Toolkit (BAT) is a software package aimed at these purposes. BAT is based on Bayes' theorem and uses Markov Chain Monte Carlo to help to solve statistical problems encountered in Bayesian inference. It gives access to the full posterior probability distribution and enables straightforward parameter estimation, limit setting and uncertainty propagation [87, 88].

Bayes' theorem for a single model has the form

$$P(\vec{\lambda}|\vec{D}) = \frac{P(\vec{D}|\vec{\lambda})P_0(\vec{\lambda})}{\int P(\vec{D}|\vec{\lambda})P_0(\vec{\lambda})\,\mathrm{d}\lambda} \tag{5.1}$$

i.e., the probability of parameter set $\vec{\lambda}$ given data $\vec{D}$ (the *posterior* probability) is proportional to the probability of data given parameters (also known as the *likelihood*) times the initial probability for the parameters (the *prior* probability). It can be interpreted from the formula that: the knowledge about the parameters of the model (or the model itself) before the experiment, the prior, is updated using the probability of the new data for different values of the parameters, resulting in posterior knowledge.

In some cases, the posterior possibly depends on various parameters including ones of interest and non-interest (also called nuisance parameters). Systematic uncertainties in a measurement are often described using nuisance parameters [89]. These quantities are necessarily included in the analysis since they have an impact on our signal or background estimation, though they are of no intrinsic interest. The so-called marginalization is a powerful method to deal with nuisance parameters. It proceeds by integrating over these non-interest parameters, denoted as $\vec{\theta}$, in order to get a marginal posterior as a function of only parameters of interest $\vec{\lambda}$:

$$P(\vec{\lambda}|\vec{D}) = \int_{-\infty}^{+\infty} P(\vec{\lambda}, \vec{\theta}|\vec{D})d\vec{\theta} \tag{5.2}$$

BAT is implemented in C++ and relies on ROOT [90] to provide a reliable and fast code for numerical operations as well as a flexible framework to formulate any model of interest and its parameters. It features the possibility to estimate parameters

and to compare models. A procedure to estimate the goodness-of-fit is also included and based on ensemble tests. The Markov Chain Monte Carlo is used as a key tool in BAT which allows for the mapping of the posterior probability in multidimensional parameter space and the extraction of quantities of interest.

For each data analysis, the user only needs to implement the model by defining the parameters, $\vec{\lambda}$ and $\vec{\theta}$ (if required), the likelihood, $P(\vec{D}|\vec{\lambda})$, and the priors, $P_0(\vec{\lambda})$, and data inputs. BAT will do the rest: common tasks such as normalization, mode finding, goodness-of-fit test, marginalization and presentation of the outputs are nicely handled by BAT functions.

5.2 Bayesian approach in limit setting

In the Bayesian framework, the outcome of a typical experiment is modeled in terms of parameters of interest and nuisance parameters which describe systematic effects or uninteresting degrees of freedom. The posterior probability is expressed as a function of both parameters of interest and nuisance parameters. One needs a marginalization step which is to integrate over all nuisance parameters in order to obtain the marginal posterior probability distribution as a function of only parameters of interest. Following this way, one can evaluate the confidence interval of parameters of interest in a manner that is independent of the nuisance parameters.

In addition, prior probabilities need to be specified for all parameters and should represent our knowledge of parameter distribution without taking into account information from data. In the Bayesian approach, the choice of the prior probability for the parameter does have some impact on the evaluation of confidence intervals. An uniform distribution is commonly preferred to noninformative prior [91] which has a minimal impact on the posterior. Some statisticians favor noninformative priors because they appear to be more objective [92]. However, it is unrealistic to expect that noninformative priors represent total ignorance about the parameter of interest.

In our case, we choose to apply the Bayesian approach to the counting experiment analysis. The number of observed data events follows a Poisson distribution. Its mean is estimated as the sum of expected signal and background. Therefore, the likelihood

to observe n_{obs} events is:

$$\mathcal{L}(n_{obs}|N_{sig}, N_{bkg}) = \frac{\mu^{n_{obs}} e^{\mu}}{n_{obs}!} \quad \text{, where} \quad \mu = N_{sig} + N_{bkg}. \tag{5.3}$$

Uncertainties in any of the free parameters of the likelihood are treated as nuisance parameters by multiplying the likelihood by the probability density function (pdf) which characterizes that uncertainty. If N_{sys} such nuisance parameters $\theta_1, ..., \theta_{N_{sys}}$ are identified, the likelihood becomes

$$\mathcal{L}(n_{obs}|N_1, ..., N_j, \theta_1, ..., \theta_i) = \frac{\mu^{n_{obs}} e^{\mu}}{n_{obs}!} \prod_{i=1}^{N_{sys}} G(\theta_i) \text{ , where } \mu = \sum_j \sum_i N_j(1 + \theta_i \epsilon_{ji}) \tag{5.4}$$

where ϵ_{ji} is the relative change in normalization of process j ($j = 1$ stands for signal and $j = 2$ is for background) for each source of systematic uncertainty i. $G(\theta_i)$ is the pdf for parameter θ_i and is chosen to be Gaussian [89].

We now generalize this procedure to include the shape of data distribution by introducing multiple bins. The number of observed events in bin k is represented by the Poisson distribution with mean μ_k. The binned likelihood function is modified:

$$\mathcal{L}(data|N_1, ..., N_j, \theta_1, ..., \theta_i) = \prod_{k=1}^{N_{bin}} \frac{\mu_k^{n_k} e^{\mu_k}}{n_k!} \prod_{i=1}^{N_{sys}} G(\theta_i) \text{ , where } \mu_k = \sum_j \sum_i N_j T_{jk}(1 + \theta_i \epsilon_{jik}) \tag{5.5}$$

where signal and background correspond to template numbers $j = 1$ and $j = 2$ respectively, G is a Gaussian prior for nuisance parameters θ_i that control bin-by-bin systematic variations ϵ_{jik} of the unit-area template shapes T_{jk}.

The dependence of the likelihood is reduced to one parameter of interest, typically the cross section of interest signal, by a marginalization technique:

$$\mathcal{L}'(data|\sigma B) = \int \mathcal{L}(\sigma B, \theta_1, ..., \theta_N) d\theta_1 ... d\theta_N. \tag{5.6}$$

The reduced likelihood function is converted into a posterior probability density using Bayes' theorem, assuming a uniform positive prior in (σB), i.e. $\pi(\sigma B) = 1$. The maximum of the posterior probability density $P(\sigma B|data)$ corresponds to the most likely signal content given data. The 95% Bayesian upper limit $(\sigma B)_{95}$ is obtained by integrating the posterior probability density:

$$0.95 = \frac{\int_0^{(\sigma B)_{95}} \mathcal{L}'(\sigma B)\pi(\sigma B) d(\sigma B)}{\int_0^{+\infty} \mathcal{L}'(\sigma B)\pi(\sigma B) d(\sigma B)}. \tag{5.7}$$

The cross section limits are converted into mass limit using the theoretical (σB) dependence on the graviton mass [82].

We now discuss the advantage of the shape analysis. In the counting experiment approach, choosing an appropriate region to count events ("signal region") is a non-trivial task. A small signal region typically yields high signal purity, but events outside the region are lost, which leads to a larger statistical error in the parameter estimation. We can improve this error by enlarging the counting region: more signal events are added, but also more background events. The signal purity consequently decreases. It is necessary to define an optimized region of balancing these two effects in order to get the best possible estimated parameters. However, the method of binning the data sample can solve these problems. Applying bin-by-bin processing, we do not lose the shape information of the distribution. It means that the signal purity is still kept high in the most interesting bins. We just include more bins, or add more "acceptance", into the calculation even if the signal purity of the additional bins is lower. This achieves better results than just one counting region.

5.3 Setting limits on the parameter of the ADD model

In the previous chapter we obtained the observed diphoton invariant mass distribution shown with the predicted SM background and expected signals for several ADD models superimposed. This is summarized in figure 5.1. Seeing that no significant data exceed from the background, we proceed to set limits on the various ADD model implementations. Firstly, we set limits using the counting experiment approach. We further set limits taking into account the shape of distribution and quantify the improvements due to this approach.

5.3.1 Limits using a counting experiment approach

The procedure is to define a mass region $m_{\gamma\gamma} > m_{\gamma\gamma}^{cut}$ to count the number of observed events. The expected number of background and signal events are then used with BAT to perform limit setting in this 1-bin region. We optimize the choice of the mass

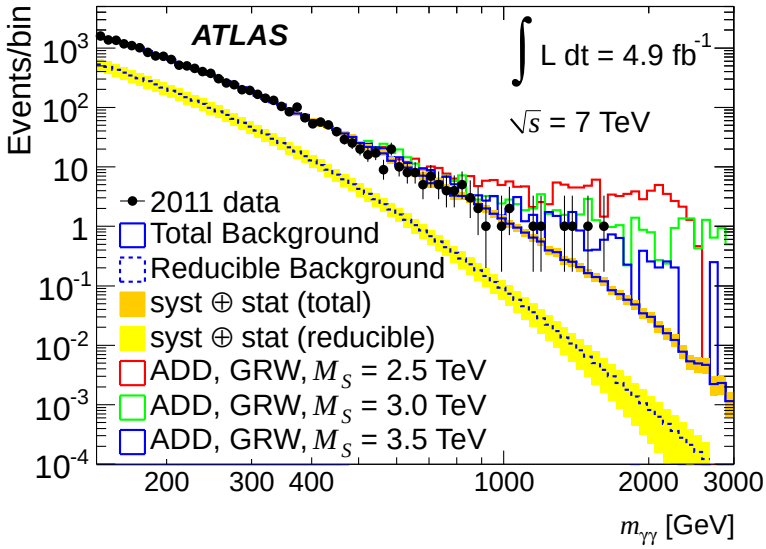

Figure 5.1: Observed invariant mass distribution of diphoton events, with the predicted SM background and expected signals for several ADD models superimposed.

cut and find that $m_{\gamma\gamma}^{cut} = 1217$ GeV is the optimal choice which yields the smallest expected limit on the cross section of new physics. The optimization procedure will be described in the following.

The likelihood in the presence of nuisance parameters which represent the uncertainties on signal and background is given by:

$$\mathcal{L}(n_{obs}|s,b) = \frac{\mu^{n_{obs}} e^{-\mu}}{n_{obs}!} \times G(\epsilon_b, 1, \frac{\sigma_b}{b}) \times G(\epsilon_s, 1, \frac{\sigma_s}{s}) \quad \text{, where} \quad \mu = s \times \epsilon_s + b \times \epsilon_b. \quad (5.8)$$

In the equation above, s is the number of expected signal events, b is the estimated total background contribution, σ_b is the uncertainty on b, σ_s is the uncertainty on s, ϵ_b and ϵ_s are the nuisance parameters representing the gaussian fluctuations of background estimation and signal yield determination respectively. We choose gaussian prior for these nuisance parameters with mean of 1 and widths of the corresponding relative uncertainties. Applying Bayes' theorem and marginalization of the posterior, we obtain the Bayesian upper limit of the signal events at 95% C.L.

In the region defined by $m_{\gamma\gamma} > 1217$ GeV, $n_{obs} = 4$ events are observed in the data, compared to a total background expectation of 2.32 events (with a 16% relative uncertainty). The expected and observed limits at 95% C.L. on the number

Stat. method	Expected limit -2σ	-1σ	Central value	$+1\sigma$	$+2\sigma$	Observed limit
Bayes	3.08	3.08	5.18	5.96	8.53	7.21

Table 5.1: Expected and observed limits at 95% C.L. on the number of signal events using Bayes statistical method.

of signal events are presented in table 5.1. The observed limit is understood as the result from using experimental data while the expected limit is obtained from pseudo-experiments. The "data" of pseudo-experiments are obtained by a simulation that mimics the *real* experiment. The simulated data in our case include backgrounds only, i.e. the pseudo-experiment data are simulated by a fluctuation of backgrounds within their determined uncertainty. A thousand pseudo-experiments are generated in order to produce a distribution of the upper limits on the parameter. The expected limit is, by definition, the median of this distribution.

We can translate the observed limit on the number of signal events into constraints on the parameter η_G of the ADD model using the following procedure: compute the number of expected signal events as a function of η_G and find the intersections with the expected and observed limit line from table 5.1. We notice that we cannot disentangle the contribution of new physics (NP) (or signal) from the SM (considered as irreducible background) in the ADD simulation samples. In order to define the number of selected signal events, we subtract the contribution of SM from the number of events that pass the selection criteria in the ADD MC samples. The result is shown in figure 5.2. A given value of η_G is excluded if it falls in the region where the number of signal events is greater than the upper limit. The acceptable η_G interval in the Hewett model is given in table 5.2. It also shows the results obtained when accounting for NLO effects by applying a constant k-factor value of 1.7 to the signal. This k-factor has been provided by the authors of Ref. [93, 94], who have updated their calculation if the NLO cross sections for 14 TeV to the case of 7 TeV proton-proton collisions.

Finally, we translate into the limits on M_S based on the relation $\eta_G = \mathcal{F}/M_S^4$ where $\mathcal{F}$ definition depends on the formalism (equation 1.8). The results is summarized in

k-factor	Allowed interval for η_G
1.0	[-0.0191, 0.0115]
1.7	[-0.0159, 0.0085]

Table 5.2: Allowed interval for η_G in the Hewett model.

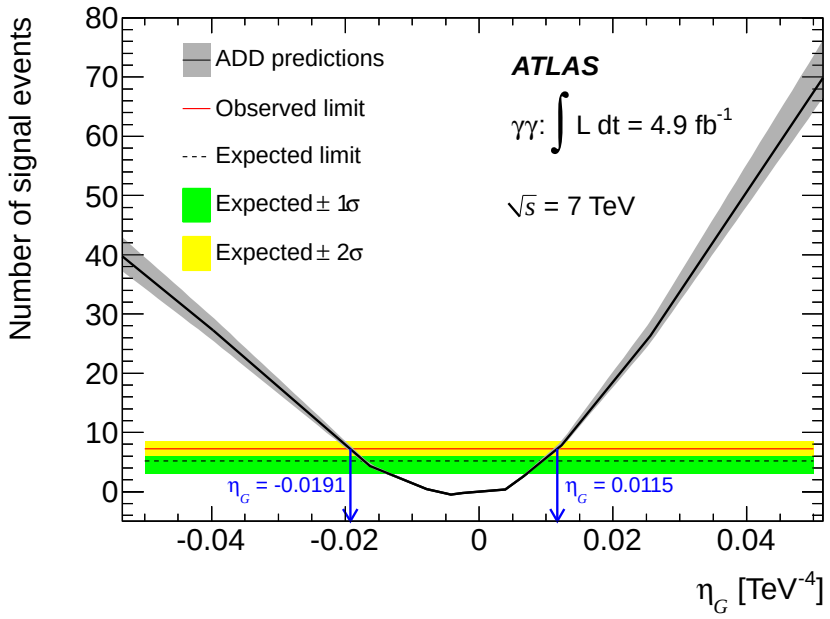

Figure 5.2: Number of signal events as a function of η_G. The red horizontal line corresponds to the observed limit, the dashed line corresponds to the expected limit and the green (resp. yellow) band to the $\pm 1\sigma$ ($\pm 2\sigma$) uncertainty on the expected limit. The dark curve corresponds to MC predictions from various samples. The band around it illustrates the theoretical uncertainty due to the PDF expressed at 90% C.L.. When the prediction is greater than the limit line, the corresponding value for η_G is excluded.

k-factor	ADD	GRW	Hewett		HLZ				
Value	Parameter		Pos.	Neg.	$n=3$	$n=4$	$n=5$	$n=6$	$n=7$
1.0	η_G	0.0115	0.0115	-0.0191			0.0115		
	M_s	3.05	2.73	2.40	3.63	3.05	2.76	2.57	2.43
1.7	η_G	0.0085	0.0085	-0.0159			0.0085		
	M_s	3.29	2.94	2.52	3.92	3.29	2.98	2.77	2.62

Table 5.3: 95% CL limits on the ADD model parameters η_G and M_S for the various ADD models.

table 5.3.

Optimization of the invariant mass cut

As discussed above, a trade-off between signal purity and signal acceptance has to be made in the counting experiment approach. The aim of the optimization procedure is to define the invariant mass region where the expected limit on the ADD parameter η_G is the best possible. This results in the smallest expected limit on the cross-section of NP, σ_{95}. The invariant mass distribution of the ADD signal varies with the value of M_S. This implies that the optimization depends on the value of M_S. We arbitrarily chose the ADD prediction for GRW convention, $n_{ED} = 2$, $M_S = 2500$ GeV.

As discussed above, the contribution of NP in the ADD simulation samples can not be disentangled from the SM. Therefore, the contribution of NP is defined as the difference between the ADD samples and the pure SM sample. First step is to determine the product $(\epsilon \times \mathcal{A})_{NP}$:

$$(\epsilon \times \mathcal{A})_{NP} = \frac{N^{RTI}_{NP}}{N^{G}_{NP}} = \frac{N^{RTI}_{tot} - N^{RTI}_{SM}}{N^{G}_{tot} - N^{G}_{SM}} = \frac{(\sigma \cdot \epsilon \cdot \mathcal{A})_{tot} - (\sigma \cdot \epsilon \cdot \mathcal{A})_{SM}}{\sigma_{tot} - \sigma_{SM}} \tag{5.9}$$

where $N^{RTI}_{NP,\,SM,\,tot}$ is the number of reconstructed, tightly identified and isolated events and $N^{G}_{NP,\,SM,\,tot}$ is the number of generated events for respectively NP, SM contributions and the total (tot) sample. σ_{tot} is the total diphoton production including both the SM processes and contributions from the Gravitons, σ_{SM} is the cross section of the SM processes only, $\mathcal{A}$ is fraction of events in kinematical and geometrical acceptance of our measurement, ϵ is the event reconstruction and selection efficiency.

$m_{\gamma\gamma}^{cut}$ (GeV)	N_{95}	b_{irr}	$(\mathcal{A} \times \epsilon)_{tot}$	O
901	9.27	10.66	0.049	0.2960
1009	7.28	6.03	0.041	0.2502
1129	5.90	3.36	0.034	0.2291
1217	5.19	2.22	0.033	0.1990
1312	4.66	1.50	0.029	0.1995
1415	4.26	1.00	0.024	0.2179
1525	3.91	0.64	0.020	0.2370
1644	3.64	0.39	0.017	0.2566
1707	3.53	0.31	0.015	0.2816

Table 5.4: Optimizing the mass threshold for the signal region definition using expected limits.

Then giving the limit on the number of signal events at 95% CL (namely N_{95}), we can convert into a limit on ADD cross section, σ_{95} :

$$\sigma_{95} = \frac{N_{95}}{(\epsilon \times \mathcal{A})_{NP} \cdot \mathcal{L}} = \frac{N_{95} \cdot (\sigma_{tot} - \sigma_{SM})}{\mathcal{L} \cdot (\sigma \cdot \epsilon \cdot \mathcal{A})_{tot} - \mathcal{L} \cdot (\sigma \cdot \epsilon \cdot \mathcal{A})_{SM}} \tag{5.10}$$

We defined $m_{\gamma\gamma}^{cut}$ as the lower bound for the search region, therefore the contribution of the irreducible background (b_{irr}) in this region is computed as :

$$b_{irr} = \int_{m_{\gamma\gamma}^{cut}}^{+\infty} f_{irr}(m_{\gamma\gamma}) d(m_{\gamma\gamma}) = \mathcal{L} \cdot (\sigma \cdot \epsilon \cdot \mathcal{A})_{SM} \tag{5.11}$$

Finally, the figure-of-merit O, calculated as in equation 5.12, is minimized to determine the optimal region.

$$O = \frac{\sigma_{95}}{\sigma_{tot} - \sigma_{SM}} = \frac{N_{95}}{\mathcal{L} \cdot (\sigma \cdot \mathcal{A} \cdot \epsilon)_{tot} - b_{irr}} \tag{5.12}$$

For different mass thresholds, the expected limit on the extra contribution N_{95}, irreducible background, b_{irr}, and the figure-of-merit O are tabulated in table 5.4. The value $m_{\gamma\gamma}^{cut} = 1217$ GeV has been chosen as O has the smallest value.

5.3.2 Limits using the shape information

In this section, we utilize an advanced approach in limit setting. Instead of simply counting events of data and MC above a given value of invariant mass to input to the likelihood function, we further exploit the shapes of the distributions. This is achieved by applying bin-by-bin Poisson statistic in the likelihood as mentioned in equation 5.5. The inputs needed in this approach are numbers of events in bins from data and MC mass distribution.

In this approach we aim to set a limit directly on the model parameter η_G instead of the number of expected signal. For this purpose, it is necessary to have several mass distributions of signal samples corresponding to different η_G from the model. To have the best determination of which signal plus background fit to data distribution, it requires as many ADD samples as possible. We generate a hundred ADD samples with various η_G or M_S scales. Due to a limit of computing resources, it is not possible to ask for all these samples to be processed through the detector simulation. As a result, the invariant mass distribution for these samples can be easily obtained at the true level but not at the reconstructed level. The reconstructed mass shapes can, however, be obtained by applying a reweighting procedure based on the current official samples (listed in table 4.1) where the mass shapes are known at both true and reconstructed levels.

In principle, the reconstructed mass histogram can be deduced from the known reconstructed mass shape of official samples h_{reco}^{offi} and the ratio of the true mass shapes between the generated and official samples (which is denoted as the weight w)

$$h_{reco}^{gen} = h_{reco}^{offi} \times w \quad \text{, where} \quad w = \frac{h_{true}^{gen}}{h_{true}^{offi}} \tag{5.13}$$

Applying bin-by-bin for the reconstructed histogram, the equation 5.13 becomes:

$$h_{reco}^{gen}(i) = \sum_j h_{reco}^{offi}(i,j) \times w_j \quad \text{, where} \quad w_j = \frac{h_{true}^{gen}(j)}{h_{true}^{offi}(j)} \tag{5.14}$$

where i denotes the bin index of reconstructed histogram and j represents the bin index of true histogram. The sum over j for a given bin i indicates that it is possible for a wide range of various true mass values, which arranges in different bins at the true level, to fall into a same mass bin at the reconstruction level. Moreover, this

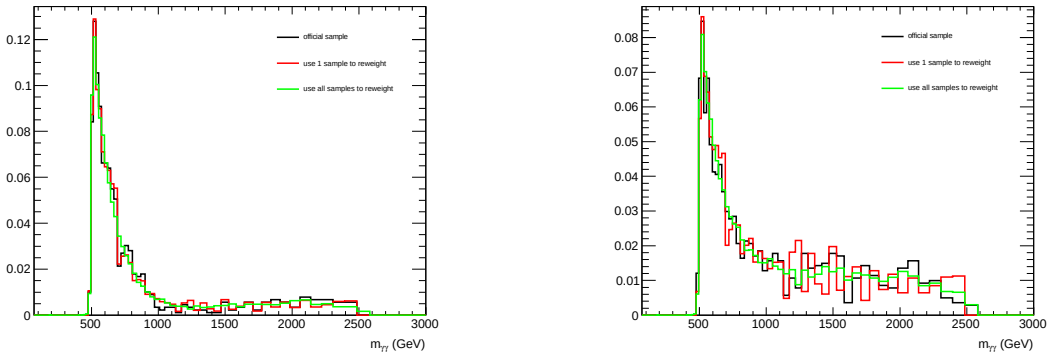

Figure 5.3: Comparison of reconstructed mass distributions obtained by the reweighting procedure to that obtained by full reconstruction procedure (noted by official sample) for M_S=2500 GeV samples with GRW (right) and Hewett- (left) convention. All shapes are normalized to unit surface.

is simply a translation from true level to reconstructed level and does not depend on model parameter. We can therefore add up all available official ADD samples to have more statistical mass distributions and consequently reduce the uncertainty in the weight w_j determination. This produces final smooth distributions with high statistics. Figure 5.3 shows a comparison of reconstructed mass shape obtained by this reweighting procedure to that obtained by full reconstructed procedure for a specific sample. The result is acceptable.

With this procedure, we explicitly lose the information of reconstruction process, or the offline efficiency of photon reconstruction in particular. It can be nevertheless inferred from the official samples by assuming that this efficiency is rather uniform for different η_G samples (it has seen from table 4.4). We finally normalize the mass distribution to the integrated luminosity of data. The normalized number of expected events as a function of invariant mass in several M_S samples is shown in figure 5.4. It is noticed that the number of events shown in figure 5.4 which includes the significant signal added by the expected Standard Model background. We need to subtract the event numbers from the background to be usable for limit setting.

The signal mass distributions were obtained. The next step is replacing the parameter of interest in the likelihood function, the number of signal events, by η_G to enable direct limit setting on η_G. We need a parametrization of the number of

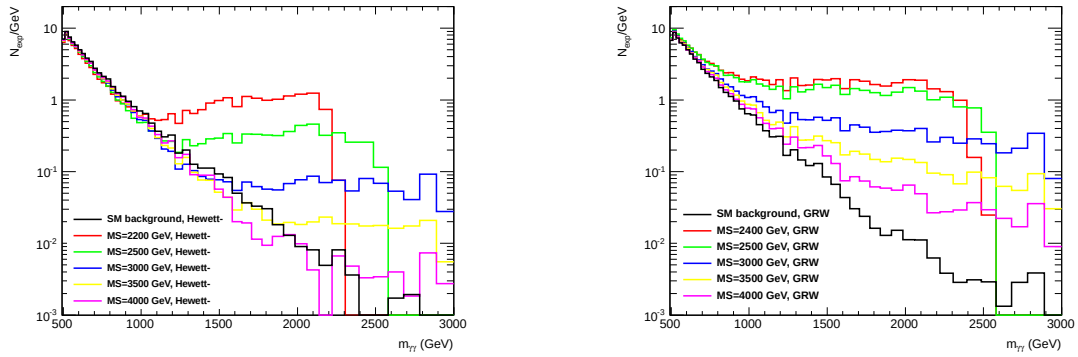

Figure 5.4: Normalized number of expected events as a function of invariant mass with several M_S for GRW and Hewett- convention are shown on the right and left respectively.

expected signal events as a function of η_G. From the discussion of the model in chapter 1, the cross section can be parameterized as a polynomial $\mathcal{O}(2)$ of η_G while the cross section is proportional to the number of expected events. Therefore we can obviously formulate

$$n_{exp} = n_0 + n_1\eta_G + n_2\eta_G^2 \tag{5.15}$$

where n_0, n_1, n_2 are evaluated from the fitted curve of n_{exp} distribution versus η_G.

As a validation of reweighting procedure, a parametrization of signal events depending on η_G is shown in figure 5.5, superimposed on the official Monte Carlo prediction (number of signal events is counted above the mass cut of 1217 GeV). The new parametrization is seen in good agreement with that from official samples. Also the observed and expected number of signal event limits are displayed. Consequently, a new interval limit of η_G can be extracted and shown in table 5.5 with the quotation "1-bin".

The expected number of events in each mass bin is counted and parameterized as a function of η_G, as illustrated in figure 5.6. A polynomial $\mathcal{O}(2)$ is fitted to the curve. The parameterized function is included in the likelihood function which is now modified as in equation 5.5. The number of expected events μ in the likelihood is now presented as a function of η_G, instead of the number of expected signals. As a result, the model parameter η_G is now treated as the parameter of interest and directly proceeded a limit setting. For a comparison, table 5.5 presents the

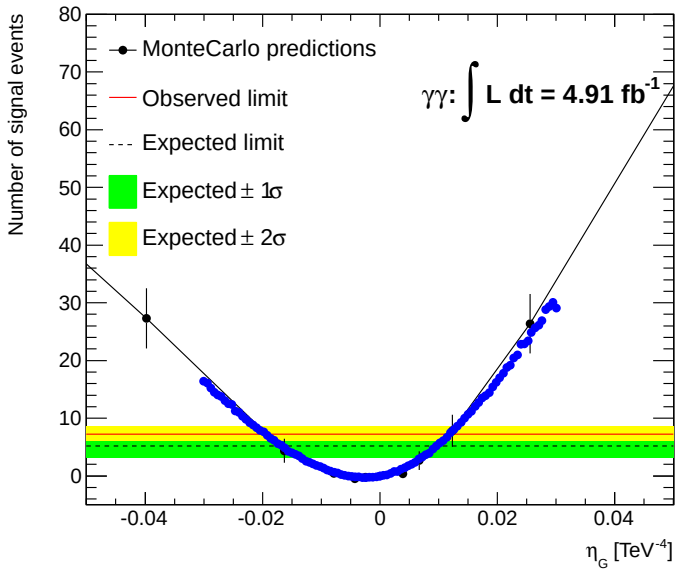

Figure 5.5: A parametrization of predicted signal events as a function of η_G obtained from reweighting procedure (the blue point curve) superimposes on the official Monte Carlo prediction (the black one). Also the observed and expected number of signal event limits are displayed.

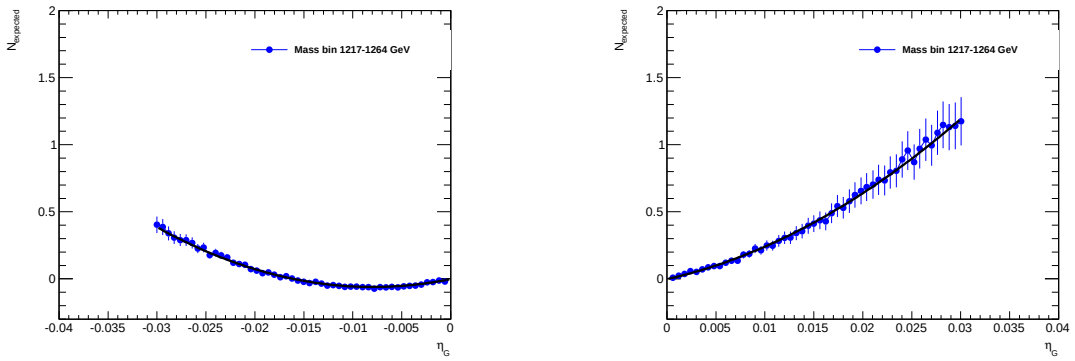

Figure 5.6: Number of expected events (in a given mass bin) as a function of η_G for Hewett- and GRW convention are shown on the left and right respectively.

	Allowed interval for η_G
1-bin	[-0.0180810, 0.0109742]
shape	[-0.0124174, 0.0097303]

Table 5.5: Interval of observed limit of η_G for the 1-bin counting and the shape approach by using the parametrization obtained from reweighting procedure. The mass bin cut is same for previous study, 1217.41 GeV.

results obtained by both 1-bin counting and using the shape. The results which are translated into M_S limits with different formalism are shown as well in table 5.6 (no k-factor is applied in this section). We achieve a slight increase by a factor of 1.04 for constructive interference and of 1.11 for destructive interference, comparing to the counting experiment results.

In addition, several mass cut region extending from about 1700 to 600 GeV are performed to set limits. The observed limit as well as the expected limit with its uncertainty is shown in figures 5.7 and 5.8. An improvement on expected limit is visible when moving to lower mass region in consistence with the concept of enlarging the region of counting events. Especially, this improvement is clearly seen in high mass region where the contamination of background is still small. The -1σ and -2σ variations of the expected limit exhibit a tendency to be, in particular, close to the expected limit at large mass cut. This behavior is expected as signals with large

k-factor	ADD	GRW	Hewett		HLZ				
Value	Parameter		Pos.	Neg.	$n=3$	$n=4$	$n=5$	$n=6$	$n=7$
1.0	η_G	0.0097	0.0097	-0.0124	0.0097				
	M_s	3.18	2.84	2.67	3.79	3.18	2.88	2.68	2.53

Table 5.6: Observed limits on M_S (TeV) result from the mass shape fitting method by using the parametrization obtained from reweighting procedure. The mass bin cut is same for previous study, 1217.41 GeV.

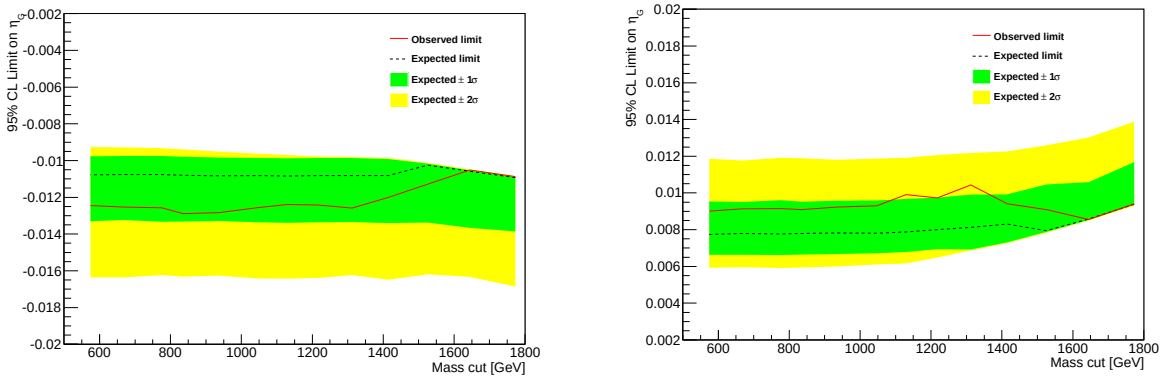

Figure 5.7: The observed and expected limits on η_G interval is presented as a function of invariant mass cut. Left: Hewett- and Right: GRW convention.

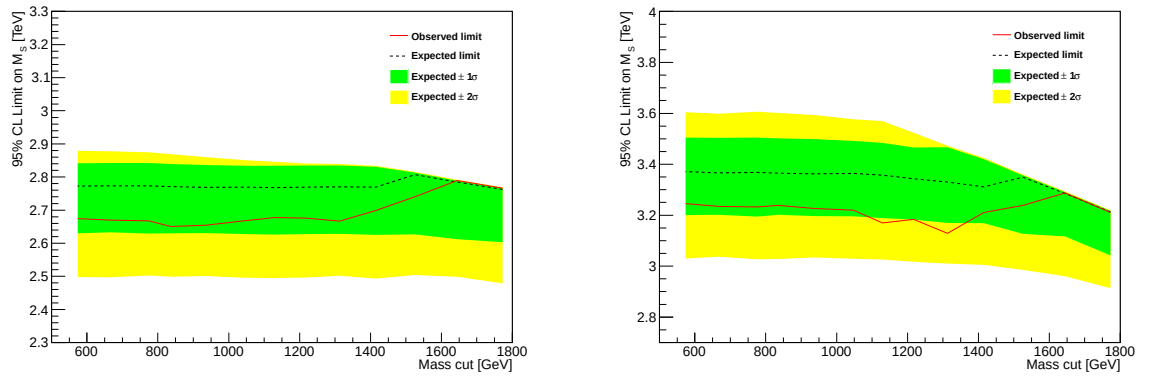

Figure 5.8: The observed and expected limits on M_S is presented as a function of invariant mass cut. Left: Hewett- and Right: GRW convention.

invariant mass would manifest themselves in regions of $m_{\gamma\gamma}$ where the SM background is small and the poissonian fluctuations around the mean expected background are highly asymmetric.

Chapter 6

Conclusion

In summary, this thesis have presented the analysis to search for the Large Extra Dimensions using 4.91 fb^{-1} of data collected in 2011 in the Atlas experiment at the LHC collider at CERN. We have looked for the manifestation of extra dimensions via the effect of virtual graviton exchange on the di-photon final state. The diphoton invariant mass spectrum has been measured and found no excess of data over the background expectation. The two approaches of limit setting have been exploited: the counting experiment and the shape analysis. It has set, in the counting experiment, limits on the ultraviolet cutoff scale M_S between 2.62 and 3.92 TeV at 95% C.L., depending on the number of extra dimensions and the theoretical formalism used. The shape analysis has achieved 4% of improvement on the limits. Finally, we notice that these analysis results have been approved by Atlas Collaboration and have been accepted for publication in the New Journal of Physics [37].

Bibliography

[1] K Nakamura and et. al. Review of particle physics. *Journal of Physics G: Nuclear and Particle Physics*, 37(7A):075021, 2010.

[2] E. Fermi. An attempt of a theory of beta radiation. *Z.Phys.*, 88:161–177, 1934.

[3] David Griffiths. *Introduction to Elementary Particles*. Wiley-VCH, 2nd edition, 2008.

[4] S.L. Glashow. Partial Symmetries of Weak Interactions. *Nucl.Phys.*, 22:579–588, 1961.

[5] Steven Weinberg. A Model of Leptons. *Phys.Rev.Lett.*, 19:1264–1266, 1967.

[6] Abdus Salam. Weak and Electromagnetic Interactions. *Conf.Proc.*, C680519:367–377, 1968.

[7] Steven Weinberg. Conceptual foundations of the unified theory of weak and electromagnetic interactions. *Rev. Mod. Phys.*, 52:515–523, Jul 1980.

[8] Hideki Yukawa. On the interaction of elementary particles. i *. *Progress of Theoretical Physics Supplement*, 1:1–10, 1955.

[9] Steven Weinberg. Nonabelian Gauge Theories of the Strong Interactions. *Phys.Rev.Lett.*, 31:494–497, 1973.

[10] D.J. Gross and Frank Wilczek. Ultraviolet Behavior of Nonabelian Gauge Theories. *Phys.Rev.Lett.*, 30:1343–1346, 1973.

[11] H. David Politzer. Reliable Perturbative Results for Strong Interactions. *Phys.Rev.Lett.*, 30:1346–1349, 1973.

[12] H. David Politzer. Asymptotic Freedom: An Approach to Strong Interactions. *Phys.Rept.*, 14:129–180, 1974.

[13] Nicola Cabibbo. Unitary Symmetry and Leptonic Decays. *Phys.Rev.Lett.*, 10:531–533, 1963.

[14] Makoto Kobayashi and Toshihide Maskawa. CP Violation in the Renormalizable Theory of Weak Interaction. *Prog.Theor.Phys.*, 49:652–657, 1973.

[15] F. Englert and R. Brout. Broken Symmetry and the Mass of Gauge Vector Mesons. *Phys.Rev.Lett.*, 13:321–323, 1964.

[16] Peter W. Higgs. Broken Symmetries and the Masses of Gauge Bosons. *Phys.Rev.Lett.*, 13:508–509, 1964.

[17] ATLAS Collaboration. Observation of a new particle in the search for the Standard Model Higgs boson with the ATLAS detector at the LHC. *Phys.Lett.*, B716:1–29, 2012.

[18] CMS Collaboration. Observation of a new boson at a mass of 125 GeV with the CMS experiment at the LHC. *Phys.Lett.*, B716:30–61, 2012.

[19] Nima Arkani-Hamed, Savas Dimopoulos, and G.R. Dvali. The Hierarchy problem and new dimensions at a millimeter. *Phys.Lett.*, B429:263–272, 1998.

[20] Ignatios Antoniadis, Nima Arkani-Hamed, Savas Dimopoulos, and G.R. Dvali. New dimensions at a millimeter to a Fermi and superstrings at a TeV. *Phys.Lett.*, B436:257–263, 1998.

[21] Nima Arkani-Hamed, Savas Dimopoulos, and G.R. Dvali. Phenomenology, astrophysics and cosmology of theories with submillimeter dimensions and TeV scale quantum gravity. *Phys.Rev.*, D59:086004, 1999.

[22] T. Appelquist, A. Chodos, and P. G. O. Freund. *Modern Kaluza-Klein Theories*. Addison-Wesly, 1987.

[23] Theodor Kaluza. 96:69–72, 1921.

[24] Oskar Klein. Quantentheorie und fünfdimensionale relativitätstheorie. 37:895–906, 1926.

[25] K. Becker, M. Becker, and J.H. Schwarz. *String Theory and M-Theory. A Modern Introduction*. Cambridge U.P., 2006.

[26] Long J.C. and Price J.C. Current short-range tests of the gravitational inverse square law. *Comptes Rendus Physique*, 4(3):337–346, 2003.

[27] Greg L. Landsberg. Collider searches for extra dimensions. *eConf*, C040802:MOT006, 2004.

[28] Gian Francesco Giudice and Alessandro Strumia. Constraints on extra dimensional theories from virtual graviton exchange. *Nucl.Phys.*, B663:377–393, 2003.

[29] Gian F. Giudice, Riccardo Rattazzi, and James D. Wells. Quantum gravity and extra dimensions at high-energy colliders. *Nucl.Phys.*, B544:3–38, 1999.

[30] The Atlas collaboration. Search for dark matter candidates and large extra dimensions in events with a jet and missing transverse momentum with the ATLAS detector. *arXiv:1210.4491, CERN-PH-EP-2012-210*, 2012.

[31] Ambreesh K. Gupta, Naba K. Mondal, and Sreerup Raychaudhuri. Constraining large extra dimensions using dilepton data from the Tevatron collider. *arXiv:hep-ph/9904234*, 1999.

[32] JoAnne L. Hewett. Indirect collider signals for extra dimensions. *Phys. Rev. Lett.*, 82:4765–4768, Jun 1999.

[33] Tao Han, Joseph D. Lykken, and Ren-Jie Zhang. Kaluza-klein states from large extra dimensions. *Phys. Rev. D*, 59:105006, Mar 1999.

[34] Douglas M. Gingrich. Experimental limits on the fundamental Planck scale in large extra dimensions. *arXiv:1210.5923*, 2012.

[35] D0 Collaboration. Search for large extra spatial dimensions in the dielectron and diphoton channels in $p\bar{p}$ collisions at $\sqrt{s} = 1.96$ TeV. *Phys. Rev. Lett.*, 102:051601, Feb 2009.

[36] CMS Collaboration. Search for signatures of extra dimensions in the diphoton mass spectrum at the Large Hadron Collider. *arXiv:1112.0688, CERN-PH-EP-2011-173, CMS-EXO-11-038*, 2011.

[37] ATLAS Collaboration. Search for extra dimensions in diphoton events using proton-proton collisions recorded at $\sqrt{s} = 7$ TeV with the atlas detector at the lhc. *arXiv:1210.8389. CERN-PH-EP-2012-289*, Nov 2012.

[38] T. Binoth, J.P. Guillet, E. Pilon, and M. Werlen. A Full next-to-leading order study of direct photon pair production in hadronic collisions. *Eur.Phys.J.*, C16:311–330, 2000.

[39] Lyndon Evans and Philip Bryant. Lhc machine. *Journal of Instrumentation*, 3(08):S08001, 2008.

[40] *LEP design report*. CERN, Geneva, 1983. CERN-LEP-TH-83-29.

[41] G Rumolo, G Iadarola, O Dominguez, G Arduini, H Bartosik, S Claudet, J Esteban-Müller, F Roncarolo, E Shaposhnikova, and L Tavian. Lhc experience with different bunch spacings in 2011 (25, 50 and 75 ns). In *Proceedings of Chamonix 2012 workshop on LHC Performance*, page 10 p, Chamonix, France, 2012.

[42] `https://twiki.cern.ch/twiki/bin/view/AtlasPublic/LuminosityPublicResults`.

[43] The Atlas Collaboration. The atlas experiment at the cern large hadron collider. *Journal of Instrumentation*, 3(08):S08003, 2008.

[44] The Atlas Collaboration. Data quality status flags and good run lists for physics analysis in atlas. Technical Report ATL-COM-GEN-2009-015, CERN, Geneva, Mar 2009.

[45] W Lampl, S Laplace, D Lelas, P Loch, H Ma, S Menke, S Rajagopalan, D Rousseau, S Snyder, and G Unal. Calorimeter clustering algorithms: Description and performance. Technical Report ATL-LARG-PUB-2008-002. ATL-COM-LARG-2008-003, CERN, Geneva, Apr 2008.

[46] ATLAS Collaboration. Reconstruction of photon convertions in the "expected performance of the atlas experiment: detector, trigger and physics". CERN-OPEN-2008-020:112–140, 2009.

[47] M Wielers. Photon identification with the atlas detector. Technical Report ATL-PHYS-99-016, CERN, Geneva, Mar 1999.

[48] ATLAS Collaboration. Reconstruction and identification of photon in the "expected performance of the atlas experiment: detector, trigger and physics". CERN-OPEN-2008-020:94–111, 2009.

[49] Expected photon performance in the atlas experiment. Technical Report ATL-PHYS-PUB-2011-007, CERN, Geneva, Apr 2011.

[50] `https://twiki.cern.ch/twiki/bin/viewauth/AtlasProtected/EgammaIsolation`.

[51] M Wielers. Isolation of photons. Technical Report ATL-PHYS-2002-004, CERN, Geneva, Nov 2001.

[52] S Laplace and JB de Vivie. Calorimeter isolation and pile-up. Technical Report ATL-COM-PHYS-2012-467, CERN, Geneva, May 2012.

[53] Calibration and performance of the electromagnetic calorimeter. Technical Report ATL-PHYS-PUB-2009-003. ATL-COM-PHYS-2009-169, CERN, Geneva, Apr 2009. PUB Note from CSC book.

[54] R Sacco. Position resolution of an atlas electromagnetic calorimeter module. Technical Report ATL-LARG-2003-008, CERN, Geneva, Jul 2003.

[55] BT Le and J Stark. Study of electron cluster position measurements in the atlas electromagnetic calorimeter. Technical Report ATL-COM-CAL-2012-001, CERN, Geneva, Mar 2012.

[56] Measurement of missing tranverse energy. Technical Report ATL-PHYS-PUB-2009-016. CERN-OPEN-2008-020, CERN, Geneva, Mar 2009. Draft PUB Note for 'Measurement of Missing Transverse Energy in ATLAS' Chapter (J13).

[57] Calodepthtool. on `http://alxr.usatlas.bnl.gov/lxr/source/atlas/Calorimeter/CaloDetDescr/src/CaloDepthTool.cxx`.

[58] B. Aubert et al. Performance of the atlas electromagnetic calorimeter end-cap module 0. *Nucl.Instrum.Meth.*, A500:178–201, 2003.

[59] ATLAS Electromagnetic Liquid Argon Endcap Calorimeter Group. Construction, assembly and tests of the atlas electromagnetic end-cap calorimeters. *Journal of Instrumentation*, 3(06):P06002, 2008.

[60] ATLAS Electromagnetic Liquid Argon Barrel Calorimeter Group. Construction, assembly and tests of the atlas electromagnetic barrel calorimeter. *Nucl. Instrum. Methods Phys. Res.*, A 558(2):388 – 418, 2006.

[61] A Andreazza and et. al. Atlas inner detector track resolution measured for 2008 cosmic rays data. Technical Report ATL-COM-INDET-2009-084, CERN, Geneva, Nov 2009.

[62] S. Brandt. *Data Analysis. Statistical and Computational Methods for Scientists and Enginers*. Springer, New York, third edition edition, 1999.

[63] `https://twiki.cern.ch/twiki/bin/viewauth/AtlasProtected/EgammaGoodRunLists`.

[64] T Gleisberg and et. al. Event generation with sherpa 1.1. *J. High Energy Phys.*, 2009(02):007, 2009. arXiv:0811.4622.

[65] T Sjöstrand, S Mrenna, and P Skands. Pythia 6.4 physics and manual. *Journal of High Energy Physics*, 2006(05), 2006.

[66] `http://lapth.in2p3.fr/PHOX_FAMILY/diphox.html`.

[67] Recommendations for data analysis: Pileup reweighting tool. on `https://twiki.cern.ch/twiki/bin/viewauth/AtlasProtected/PileupReweighting`.

[68] `https://twiki.cern.ch/twiki/bin/viewauth/AtlasProtected/PhotonFudgeFactors`.

[69] The Atlas Collaboration. Reconstruction and identification efficiency of inclusive isolated photons. Technical Report ATL-PHYS-INT-2011-014, CERN, Geneva, Mar 2011.

[70] M Hance, D Olivito, and H Williams. Performance studies for e/gamma calorimeter isolation. Technical Report ATL-COM-PHYS-2011-1186, CERN, Geneva, Sep 2011.

[71] Recommendations for data analysis: Cleaning and object quality usage. on `https://twiki.cern.ch/twiki/bin/viewauth/AtlasProtected/LArCleaningAndObjectQuality`.

[72] The Atlas Collaboration. Search for high-mass dilepton resonances in 5/fb of pp collisions at sqrt(s) = 7 tev. Technical Report ATL-COM-PHYS-2012-177, CERN, Geneva, Feb 2012.

[73] The Atlas Collaboration. Search for evidence of extra dimensions in the diphoton final state in *sqrts* = 7 tev pp collisions. Technical Report ATL-COM-PHYS-2011-1078, CERN, Geneva, Aug 2011.

[74] The Atlas Collaboration. Measurement of isolated di-photon cross section in pp collision at $\sqrt{s} = 7$ tev with the atlas detector. Technical Report ATL-COM-PHYS-2011-301, CERN, Geneva, Mar 2011. This is the supporting note for the 2010 SM diphoton cross section paper, approved by ATLAS and submitted for publication.

[75] The Atlas Collaboration. Study of the di-photon backgrounds to the $h \to \gamma\gamma$ search with the atlas detector at *sqrts*= 7 tev. Technical Report ATL-COM-PHYS-2011-009, CERN, Geneva, Jan 2011.

[76] Kyle S. Cranmer. Kernel estimation in high-energy physics. *Comput.Phys.Commun.*, 136:198–207, 2001.

[77] `http://root.cern.ch/drupal/content/roofit`.

[78] K Liu, Y Liu, G Marchiori, and E Soldatov. Measurement of the identification efficiency of isolated prompt photons using radiative $z \to \ell\ell\gamma$ decays in 4.9 fb^{-1}

of atlas data. Technical Report ATL-COM-PHYS-2012-382, CERN, Geneva, Apr 2012.

[79] M Jimenez and K Tackmann. Photon identification efficiency extrapolated from electrons in $z \rightarrow e^+e^-$ decays. Technical Report ATL-COM-PHYS-2012-241, CERN, Geneva, Mar 2012.

[80] K Liu, Y Liu, and G Marchiori. Measurement of the identification efficiency of isolated prompt photons using the matrix method and 4.9 fb^{-1} of atlas data. Technical Report ATL-COM-PHYS-2012-242, CERN, Geneva, Mar 2012.

[81] The Atlas Collaboration. Measurements of the photon identification efficiency with the atlas detector using 4.9 fb^{-1} of *pp* collision data collected in 2011. Technical Report ATL-COM-PHYS-2012-408, CERN, Geneva, Apr 2012.

[82] F Alonso, X Anduaga, T Berry, Q Buat, T Dova, W Fedorko, H Hadavand, M Hao, D Hayden, Y Liu, B T Le, F Monticelli, J Parsons, J Stark, P Waller, and E Wulf. Search for extra dimensions using diphoton events in 7 tev proton-proton collisions with the atlas detector. Technical Report ATL-COM-PHYS-2012-352, CERN, Geneva, Mar 2012.

[83] Luminosity determination in pp collisions at sqrt(s) = 7 tev using the atlas detector in 2011. Technical Report ATLAS-CONF-2011-116, CERN, Geneva, Aug 2011.

[84] J. Pumplin, D. Stump, R. Brock, D. Casey, J. Huston, et al. Uncertainties of predictions from parton distribution functions. 2. The Hessian method. *Phys.Rev.*, D65:014013, 2001.

[85] G. Choudalakis and D. Casadei. Plotting the differences between data and expectation. 2011. arXiv:1111.2062v2.

[86] Diego Casadei. Statistical methods used in atlas for exclusion and discovery. PHYSTAT(arXiv:1108.2288v1), 2011.

[87] Frederik Beaujean, Allen Caldwell, Daniel Kollár, and Kevin Kröninger. The bayesian analysis toolkit. *Journal of Physics: Conference Series*, 331(7):072040, 2011.

[88] The bayesian analysis toolkit. on `http://www.mppmu.mpg.de/bat`.

[89] Pekka Sinervo. Definition and Treatment of Systematic Uncertainties in High Energy Physics and Astrophysics. *eConf*, C030908:TUAT004, 2003.

[90] `http://root.cern.ch/drupal`.

[91] `http://www.stats.org.uk/priors/noninformative/`.

[92] James Berger. The case for objective bayesian analysis. *Bayesian Analysis*, 3:385–402, 2006.

[93] L Kumar and et al. *Nucl. Phys.*, B818:28, 2009.

[94] L Kumar and et al. *Phys. Lett.*, B672:45, 2009.